conductivity has not been taken into account a renormalization of critical indices near m_c. Nevertheless, a recent numerical simulation for Dirac fermions with an uncorrelated random mass confirms a linear power law for the conductivity [335].

The suppression of the gap by random fluctuations can also play an important role in systems where a gap is induced either by an external magnetic field [336,337] or by interaction effects, such as Coulomb interaction [338] and electron–phonon interaction. Disorder, always present in realistic graphene samples, can lead to the randomness of the gap parameter. As a consequence, there is a competition between gap formation by interaction and gap suppression due to disorder. To observe a gap in the transport properties of such a system, the average gap must exceed a critical value. On the other hand, if the average gap is too small or the fluctuations are too large, the metallic behavior can survive.

6. Confinement of electrons in graphene

Quantum dots (QDs), or the 'artificial atoms' [8,9] are one of the most intensely studied systems in condensed matter physics where the fundamental effects related to various quantum phenomena in confined geometries can be studied but with the unique advantage that the nature of the confinement and the electron density can be tuned externally. However, much of the interest in this system derives from its enormous potentials for applications, ranging from novel lasers to quantum information processing. While the majority of the QD systems investigated are based on the semiconductor heterostructures, in recent years, QDs created in carbon nanotubes have been reported in the literature where the 'atomic' properties [339] were clearly elucidated and its importance in technological applications was also demonstrated [340]. Nonrelativistic electrons, the properties of which are described by the Schrödinger equation, can be easily confined by electrostatic confinement potentials, to create well-defined QD and quantum well structures in usual semiconductor systems. The behavior of relativistic electrons in graphene is however completely different. Due to the massless chiral nature of their energy dispersion, electrons in graphene can penetrate through potential barriers of any height. An electron approaching a potential barrier emerges inside the barrier as a hole, which can then freely propagate under the barrier and finally can penetrate through the barrier without any losses. Such electron tunnelling through a barrier of any height and width is known as Klein tunnelling [341–343]. A direct experimental observation of Klein tunnelling was reported in [344,345] where transport through a *n–p*-type potential barrier was measured. For an electron normally incident on the potential barrier, perfect transmission was observed, thus indicating a direct manifestation of Klein tunnelling.

Klein tunnelling therefore makes it hard to localize electrons in graphene by a confinement potential and the standard semiconductor QDs and quantum wells realized through the confinement potential cannot be achieved in graphene. The existence of Klein tunnelling for relativistic electrons in graphene and the transition from the Schrödinger bound state to the Dirac unbounded states in a confinement potential was demonstrated in [346]. Different approaches were explored to overcome the problem of electron confinement in graphene.

A straightforward approach, realized experimentally in [47,347–349], is based on 'mechanical' cutting of graphene into the desired nanosize shape. Such an island of graphene becomes a QD with characteristic discrete energy levels. The properties of these QDs are determined by the discrete nature of the energy levels and the charging effects due to inter-electron interactions within the QD.

Another approach to create QDs in graphene is to realize the QD through the confinement potential within the graphene layer. Due to Klein tunnelling, the standard confinement potential cannot localize the electron within a finite spatial region. In this case we need to consider not the QD that localizes an electron, i.e. the electron stays within the QD for infinitely long time, but a QD which can trap an electron for long enough time. Such trapping can be realized in a smooth confinement potential and only for states with large transverse momentum [350,351].

Spatial localization of an electron within a QD in graphene layer can be achieved if a finite gap is introduced in the energy dispersion for relativistic electrons. The energy gap can be produced, e.g. by the SOI, through coupling with the substrate, or in a biased graphene bilayer (Section 3). The QDs in graphene can be also introduced through a magnetic confinement potential [352–354]. In this case the nonuniform magnetic field results in electron localization within a finite spatial region, thereby creating a QD.

6.1. *QDs in graphene islands*

QDs in islands of graphene have been realized experimentally in [47,347–349]. To extract the discrete energy spectra of the QD islands, tunnelling transport through the system was measured [47,347–349]. Clear Coulomb blockade peaks in tunnelling conductance versus the bias voltage dependence have been observed (Figure 61). The positions of the peaks are determined by the charging and confinement energies within the graphene islands. The unique relativistic dispersion of electrons in graphene results in much larger confinement energy for electrons in graphene islands compared to the confinement energy of non-relativistic electrons. For graphene islands the confinement energy can be estimated as $\sim v_F h/2D$, where D is the size of the island, while for the non-relativistic massive electrons the confinement energy is $\sim h^2/8m^* D^2$, where m^* is an effective electron mass. For example, for a 40 nm QD the confinement energy is found to be $\sim$10 meV [347] for graphene while the energy is around 1 meV for a non-relativistic QD system. The interplay between the confinement energy and the charging energy determines the structure of the conductance peaks in the tunnelling transport experiments.

It was shown experimentally [347] that for large ($>$100 nm) QDs in graphene, i.e. in graphene islands, the Coulomb peaks are periodic and the positions of the peaks are mainly determined by the charging energy. From the Coulomb diamond measurements, a charging energy of 4.3 meV was extracted for 200 nm graphene islands [349]. For small QDs the energy scale is determined by the confinement energy. In this case the peaks of tunnelling conductance are nonperiodic [347] with the typical energy scale of $v_F h/2D$. Another manifestation of the confinement nature of the energy scale for small QDs is the special statistics of the energy levels, i.e. the distribution of the nearest neighbor energy-level spacing. The statistics of the energy levels are determined by the time-reversal symmetry of the Hamiltonian of the system and the

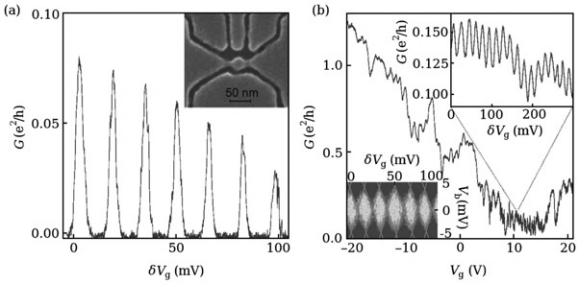

Figure 61. (a) Conductance of a graphene device with the central island of 250 nm in diameter as a function of the gate voltage, V_g, in the vicinity of +15 V, $T = 0.3$ K. The inset shows the smallest 30 nm diameter QD. (b) Conductance of the same device as in (a) over a wide range of V_g, and the temperature is 4 K. Upper inset: Zooming into the low-G region reveals hundreds of Coulomb blockade oscillations. The lower inset shows Coulomb diamond: differential conductance as a function of gate voltage (around +10 V) and bias voltage (Reprinted figure with permission from L.A. Ponomerenko *et al.*, Science, 32, p. 356, 2008 [347]. Copyright © (2008) The American Association for the Advancement of Science.).

type of boundary conditions. For non-relativistic systems, the statistics of the energy levels is described by the Poissonian distribution ($P(\delta E) = \exp(-\delta E)$) for classically regular shape of the QD. Here δE is the interlevel spacing. For an irregular classically chaotic shape, the distribution takes the Wigner–Dyson form, corresponding to the orthogonal ensemble ($P_O = (\pi/2)\delta E \exp(-(\pi/4)\delta E^2)$) for a system with time-reversal symmetry, and to the unitary ensemble ($P_U = (32/\pi^2)\delta E^2 \exp(-(4/\pi)\delta E^2)$) for a system without the time-reversal symmetry. In non-relativistic systems the time reversal symmetry is usually broken by an external magnetic field.

In graphene, even for the classically regular shape of a QD, the electron dynamics are chaotic and the statistics of energy levels are described by the Gaussian unitary ensemble [355], which corresponds to a system with broken time-reversal symmetry. The mechanism of time-reversal symmetry proposed in [355] is the infinite mass boundary condition. The experimentally measured level statistics [347] illustrates a transition from the Poisson distribution for dots of large size (>100 nm) to the distribution corresponding to chaotic Dirac billiards, for dots of small size (<100 nm) (Figure 62). Experimental results are best fitted by the Gaussian unitary distribution [347].

The results of the numerical analysis of disordered graphene QDs [356,357] show that the statistical properties of QDs strongly depend on the boundary conditions. For example, QDs with abrupt termination at the boundary show a transition from the Gaussian orthogonal ensemble at zero magnetic field to the Gaussian unitary ensemble at finite magnetic fields [356]. Therefore, these systems have time-reversal symmetry. The abrupt termination of the QD introduces inter-valley mixing at the boundary.

Another example of a boundary, considered in [357], is a smooth boundary, i.e. a smooth mass confinement. The smooth boundary condition is introduced through a smooth mass term. This type of boundary condition suppresses inter-valley scattering. It was determined that the statistics of the energy levels for QDs with a smooth boundary corresponds to the Gaussian orthogonal ensemble

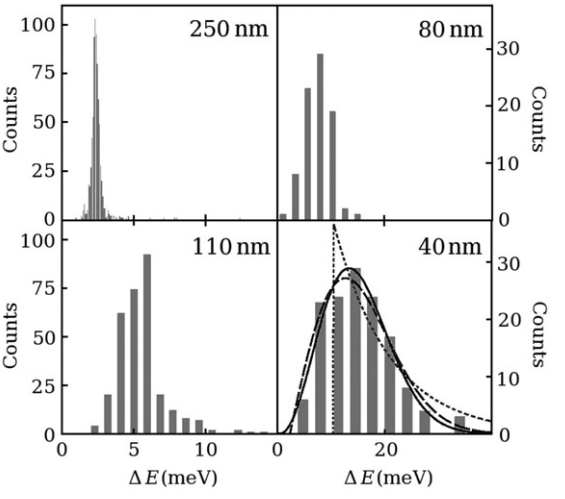

Figure 62. Level statistics in Dirac billiards. The histograms of the nearest neighbor level spacing are shown for QDs of different sizes. The level statistics becomes increasingly non-Poissonian for smaller QDs. This is illustrated for the smallest device, where the solid, dotted and dashed curves are the best fits for the Gaussian unitary, Poisson and Gaussian orthogonal ensembles, respectively. The distributions are shifted from the origin due to Coulomb blockade (Reprinted figure with permission from L.A. Ponomerenko *et al.*, Science, 32, p. 356, 2008 [347]. Copyright © (2008) The American Association for the Advancement of Science.).

for large QDs and the Poisson ensemble for small dots [356]. For small QDs the localized edge states determine the Poissonian statistics, while the contribution of the edge states is suppressed when the size of the dot is increased.

The energy spectra and the charging effects in graphene islands have been studied theoretically in great detail. It was shown that the structure of the electronic states and the energy scales of graphene QDs are determined by the edge type of the QDs, i.e. the boundary conditions, and electron occupation of the QD. There are two main types of edges in graphene QDs: armchair and zigzag, which are shown schematically in Figure 14. The distinctive feature of the armchair edge is that the vector normal to the edge is orthogonal to the bond. These two types of edges determine the basic configurations of QDs with the same type of edges along the whole boundary (Figure 63): trigonal zigzag [358–360], trigonal armchair [358,359], hexagonal zigzag [359–361], and hexagonal armchair [359,361]. A configuration with two types of edges, e.g. rectangular configuration (see Figure 64), has been also studied in the literature [362,363]. In this case there are zigzag edges along the x-axis and armchair edges along the y-axis. The dangling bonds at the edges of the graphene islands are passivated by hydrogen atoms (not shown in Figures 63 and 64).

The energy spectra of graphene QDs have been studied theoretically by two main methods: within the tight-binding model and within the Dirac relativistic equation. The tight-binding Hamiltonian has the form

$$\mathcal{H}_{\text{tight-binding}} = \sum_i \varepsilon_i c_i^\dagger c_i + \sum_{\langle i,j \rangle} t_{ij} c_i^\dagger c_j \tag{90}$$

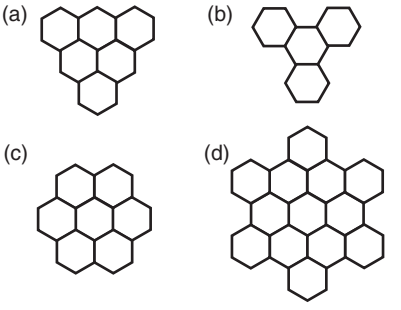

Figure 63. Typical configurations of graphene QDs with same type of the edges: (a) trigonal zigzag; (b) trigonal armchair; (c) hexagonal zigzag and (d) hexagonal armchair.

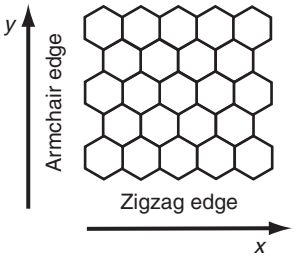

Figure 64. Rectangular QD terminated by both armchair and zigzag edges.

and the relativistic-like low-energy limit was described in Section 1.2. The properties of QDs strongly depend on the type of boundary, e.g. zigzag or armchair edges.

For the continuous Dirac-like equation, the type of the boundary determines the boundary conditions for the electron wave functions. The general energy-independent boundary condition is determined by a 4×4 matrix, M, through the following relation [364,365]:

$$\Psi = M\Psi. \tag{91}$$

For the boundary condition that preserves time reversal symmetry the matrix M is determined by three parameters [365]

$$M = (\vec{v} \cdot \vec{\tau}) \otimes (\vec{n} \cdot \vec{\sigma}), \tag{92}$$

where τ_i and σ_i are Pauli matrices in the valley space and the sublattice space, respectively. The matrix M is parametrized by the directions of two three-dimensional vectors, $\vec{v}$ and $\vec{n}$. Here the vector $\vec{n}$ is orthogonal to the unit vector normal to the boundary.

The above form of the matrix M introduces two types of boundary conditions. If we denote wave functions in the K valley by ψ_+ and those in the K′ valley by ψ_-, they are [365]: (i) zigzag-type boundary condition: $\psi_+^{\mathrm{A}} = \psi_-^{\mathrm{A}} = 0$ (any ψ_+^{B} and ψ_-^{B}) or $\psi_+^{\mathrm{B}} = \psi_-^{\mathrm{B}} = 0$ (any ψ_+^{A} and ψ_-^{A}); (ii) armchair-type boundary condition: $|\psi_+^{\mathrm{A}}| = |\psi_-^{\mathrm{A}}|$

and $|\psi_+^{\mathrm{B}}| = |\psi_-^{\mathrm{B}}|$. The type of the boundary condition is determined by the orientation of the vector, $\vec{T}$, of the period at the edge. This vector is approximately parallel to the edge. If the vector $\vec{T}$ is parallel to the bonds then the boundary condition is of the armchair type. For all other orientations of the vector $\vec{T}$, the boundary conditions are of the zigzag type [365]. Therefore, the zigzag-type boundary conditions are more generic. The zigzag boundary condition does not couple different valleys, while the armchair boundary condition introduces coupling between the two valleys.

There is an other type of boundary condition, which is used in some cases within the continuous Dirac-type model. This is the infinite mass boundary condition. This boundary condition can be realized, for example, through the staggered potential at the zigzag edge. The staggered potential means that the electrostatic potential at two lattice sites (A and B) is different, i.e. $V_A = +\mu$ and $V_{\mathrm{B}} = -\mu$. Similar to the zigzag boundary condition, the infinite mass boundary condition does not mix the valley and at the zigzag boundary takes the form [365]: $\psi_+^{\mathrm{A}} = \mathrm{i}\psi_+^{\mathrm{B}}$ and $\psi_-^{\mathrm{A}} = -\mathrm{i}\psi_-^{\mathrm{B}}$.

For triangular and trapezoidal geometries of graphene QDs the single-particle energy spectra of the QDs can be found analytically [366,367] within the tight-binding model. For example, for triangular QDs with armchair boundary conditions, the single-particle states are characterized by two integer numbers, n and m, and have the following form [367]:

$$\epsilon_{n,m,\pm} = \pm t\left\{3 + 2\cos\left[\frac{4\pi n}{3(N+2)}\right] + 2\cos\left[\frac{4\pi m}{3(N+2)}\right] + 2\cos\left[\frac{4\pi(n+m)}{3(N+2)}\right]\right\}^{\frac{1}{2}},$$

where N is number of carbon atoms per one side of the triangular QD.

The approach based on the tight-binding model is the more fundamental and is valid for QD of any size, while the Dirac equation, being a continuous approximation of the tight-binding model, is valid only for QDs of large size. In [363] a detailed comparison of the electronic eigenstates of a rectangular QD obtained within the framework of the Dirac equation and the tight-binding model was presented. It was found that the graphene QDs with size of 7×8 is the smallest one for which the Dirac equation is applicable.

Zigzag edges in graphene have unique properties. For example, they can introduce degenerate zero-energy states localized at the edges. The actual existence of zero-energy states depends on the configuration of the QD. As an example, the zero-energy states have been found only for rectangular QDs [362,363] and trigonal zigzag QDs [358–360]. However, no such zero-energy states exist for hexagonal zigzag graphene QDs [359,360]. A sufficient condition for the existence of degenerate zero-energy states in a graphene sample is the sublattice imbalance, i.e. an uncompensated lattice [360]. That is, if N_A is the number of atoms of sublattice A and N_{B} is the number of atoms of sublattice B in a graphene QD, then the parameter $N_Z = N_{\mathrm{A}} - N_{\mathrm{B}}$ determines the existence of zero-energy states. This parameter is zero for hexagonal zigzag QDs and nonzero for trigonal zigzag QDs [360]. The condition $N_Z > 0$ is the sufficient condition for the existence of zero-energy edge states but it is not the necessary condition. For example, for rectangular QDs there are zero-energy edge states, but the sample is compensated, i.e. $N_Z = 0$.

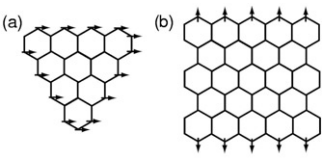

Figure 65. Local magnetization for trigonal zigzag QD (a) and rectangular QD (b). The directions of magnetization shown in the figure are chosen for the sake of clarity.

The degenerate zero-energy edge states, occupied by electrons, leads to ferromagnetic and antiferromagnetic ordering due to the inter-electron exchange interaction. To study the magnetic ordering in graphene QDs, the inter-electron interaction should be introduced, for example, within the density functional theory (DFT) *ab initio* calculations [360,362] or through the Hubbard on-site interaction combined with the Hartree–Fock mean field approach [360,363]. The DFT calculations, although more accurate than the mean field theory, can be performed only for QDs of small size. A comparison of the low-energy spectra of graphene QDs obtained within the Hubbard model and within the DFT approach shows that the Hubbard model captures correctly the low-energy physics of the QD.

The results of the numerical analysis of graphene QDs with zero-energy degenerate states, i.e. for a rectangular QD and a trigonal zigzag QD, illustrate the magnetic ordering in such graphene islands [359,360,362,363]. The magnetic moments are localized on the zigzag edges of the QDs. The type of magnetic ordering is different for rectangular and trigonal dots. For rectangular QDs the stable magnetic phase is antiferromagnetic [362,363], the magnetic structure of which is similar to the magnetic structure of graphene zigzag ribbons, namely, the magnetic moments are localized at two zigzag edges with opposite orientation (Figure 65). The results of *ab initio* DFT calculations show that the antiferromagnetic phase is a stable phase for all rectangular QDs of size larger than 3×3 [362]. For smaller QDs the stable phase is nonmagnetic [362]. For trigonal zigzag QDs the stable phase is ferromagnetic with the same orientation of magnetic moments (Figure 65), i.e. the electron spins [359,360]. The net local spin mostly sits on the edge of the QD and goes to zero in the centre of the dot.

The signature of the zero-energy degenerate edge states in graphene QDs can be observed in optical absorption experiments [358]. The absorption spectra obtained numerically within the tight-binding model clearly show rich peak structures originating from the edge states [358]. The structure is visible only for zigzag triangular graphene QDs, but does not exist for armchair triangular dots. With increasing size of the dot, the relative contribution of the edge states to the absorption spectra is suppressed. The ratio, $f_{\text{edge}}/f_{\text{all}}$, of the oscillator strength corresponding to the edge states to the total oscillator strength has a maximum value of 0.42 at $N_z = 4$ and decreases to 0.15 at $N_z = 50$. Here N_z is the number of atoms along the edge.

A detailed analysis of Coulomb interaction effects in graphene QDs was reported in [368]. The calculations were done for circular QDs within the massless Dirac equation. It was assumed that the QD has a zigzag-type boundary, which supports degenerate zero-energy edge states. The zigzag boundary condition does

not mix the two valleys. In this case each energy level of the QD is twofold valley degenerate and to find the energy spectrum it is enough to consider only one valley. Due to the circular symmetry of the problem the general solution of the Dirac equation is described by the Bessel functions and the two-component wave function for a single valley $s = \pm 1$ has the following form [368]:

$$\begin{pmatrix} \psi_s^{\mathrm{A}}(r,\theta) \\ \psi_s^{\mathrm{B}}(r,\theta) \end{pmatrix} = \begin{pmatrix} J_m(kr)\mathrm{e}^{\mathrm{i}ms\theta} \\ -\mathrm{i}J_{m-s}(kr)\mathrm{e}^{\mathrm{i}(m-s)\theta} \end{pmatrix}. \tag{93}$$

The boundary conditions corresponding to the zigzag edge were introduced:

$$\psi_s^{\mathrm{A}}(R,\theta) = 0, \tag{94}$$

where R is the radius of the QD. This boundary condition allows for surface states of the form

$$\begin{pmatrix} \psi_s^{\mathrm{A}}(r,\theta) \\ \psi_s^{\mathrm{B}}(r,\theta) \end{pmatrix} = \begin{pmatrix} 0 \\ \sqrt{\dfrac{m+1}{\pi R^{2(m+1)}}} r^m \mathrm{e}^{\mathrm{i}sm\theta} \end{pmatrix}. \tag{95}$$

In terms of the tight-binding model with the nearest neighbor hopping, the surface states in which only sublattice B is occupied are degenerate and have zero energy. Introducing next-nearest neighbor hopping to the tight-binding model results in a finite kinetic energy of the surface states and the zero-energy band becomes dispersive [368].

The Coulomb electron–electron interaction has been introduced to describe the charging effects of the dot:

$$\mathcal{H}_C = \frac{e^2}{4\pi\varepsilon_0\varepsilon} \sum_{n<n'} \frac{1}{|\vec{r} - \vec{r}'|}. \tag{96}$$

The charging properties of QDs depend on the electron occupation of the dot. For large number of electrons within the dot, all the surface states are occupied and the Fermi level is far from the neutrality point. In this case the main charging effect is a rigid shift of the electrostatic potential, which results in standard Coulomb blockade effects [368].

A different situation occurs if the number of electrons within the QD is small enough so that the electrons occupy only the surface states [368]. That situation is realized if the Fermi energy is near the neutrality point. In this case the system can be described within the truncated Hilbert state restricted only to the surface states. Since the surface states are almost degenerate, the electrons occupying these states are strongly correlated and the properties of the system are determined by the Coulomb inter-electron interaction. In [368] two trial functions for the correlated ground state were proposed: (i) the Laughlin wave function [72,137]

$$\psi(z_1, z_2, \ldots, z_N) \propto \prod_{i<j} (z_i - z_j)^p, \tag{97}$$

where $z = x + iy$, N is the number of electrons, p is odd and (ii) Wigner crystal-type wave function. Both trial functions show good agreement with the exact numerical results [368].

In [369], a rotating-electron-molecule-type wave function was introduced to describe the correlated electrons at the zero energy edge of the QDs. Based on the numerical diagonalization of the interaction Hamiltonian of the electron system with up to eight electrons, the authors concluded that the rotating-electron-molecule wave function provides a better description of the correlated electron system than the Laughlin trial function or the Wigner crystal [369]. A strongly correlated electron state exists only for the long-range Coulomb interaction. The electron correlations disappear for point-like Hubbard interaction.

A special type of graphene quantum island is a quantum ring. The most non-trivial behavior of the quantum rings is in an external magnetic field. This behavior is due to the Aharonov–Bohm effect [370] and manifests itself as periodic oscillations in the energy spectra and the transport properties as a function of the number of flux quanta through the ring, Φ. The quantum ring in graphene has been realized experimentally [371] and the current through the ring has been studied. The size of the ring is $\sim$1 μm and the system is coherent at temperatures below 1 K. The measured conductance oscillations clearly show the Aharonov–Bohm oscillations (Figure 66). Surprisingly, the amplitude of the conductance oscillations increases with increasing magnetic field strength. This tendency is shown in Figure 66. An analysis of the structure revealed that this behavior does not originate from the magnetic impurities, but rather from the orbital effect of the magnetic field.

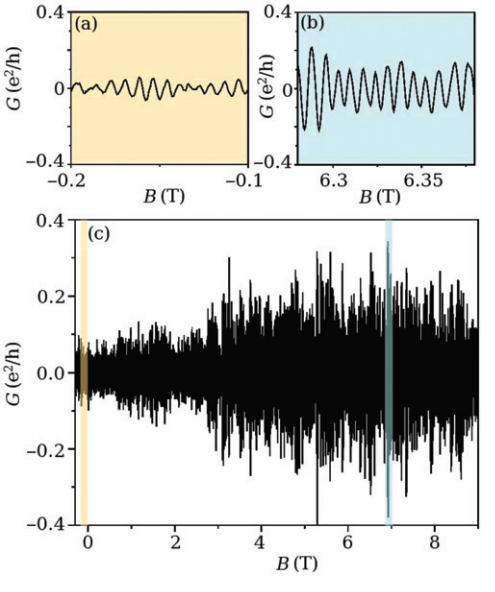

Figure 66. Aharonov–Bohm conductance oscillations measured at a gate voltage +30 V in the different magnetic field range. For $B \sim 3$ Tesla a clear increase of Aharonov–Bohm amplitude is observed. (Reprinted figure with permission from S. Russo *et al.*, Physical Review B, 77, 085413, 2008 [371]. Copyright © (2008) by the American Physical Society.)

Numerical studies of quantum rings were also reported [372–374] within the tight-binding and the continuous Dirac equation approaches. The system is studied as a function of the magnetic field, where the magnetic field in the tight-binding model is introduced through the Peierls substitution. The quantum ring in the form of a disk has been studied in [372] within the Dirac continuous equation. It was shown that even without a magnetic field the quantum ring shows the breaking of the effective time-reversal symmetry, which manifests itself as the lifting of degeneracy between the states with angular momentum m and $-m$ in the same valley in the absence of a magnetic field. Each level, however, still has the double valley degeneracy since the energy of the state with angular momentum m in valley K is equal to the energy of the state with angular momentum $-m$ in the valley K′. A finite magnetic field lifts this twofold degeneracy and breaks the time-reversal symmetry. Finally the energy spectra and the persistent current, defined as $j=-\partial E/\partial\Phi$, show periodic oscillations with the magnetic flux, Φ. Due to breaking of effective time-reversal symmetry at the zero magnetic field, the persistent current for a single valley is non-zero even at $B=0$. The persistent current for both valleys is zero at $B=0$.

In [373] the effect of electron–electron interactions in a cylindrical quantum ring system have been studied. The inter-electron interactions is introduced through the Coulomb Hamiltonian,

$$\mathcal{H}_C=\frac{1}{2}\sum_{i\neq j}\frac{e^2}{4\pi\epsilon}\frac{1}{|\vec{r}_i-\vec{r}_j|}. \tag{98}$$

The exchange Coulomb interaction between the electrons in the same valley is strong, but it is strongly suppressed for electrons in different valleys [373]. This means that there is an exchange contribution for the two-electron singlet valley state (both electrons being in the same valley), but there is no exchange interaction for the triplet valley state (two electrons in different valleys). In a two electron system, by varying the size of the quantum ring the transition from the valley-singlet ground state for small quantum rings to a valley-triplet ground state was observed.

Due to the two types of edges in a quantum ring, i.e. the inner and outer edges, there are two types of edge states [374] in the system. These edge states have been studied within the tight-binding approach in [374] for different geometries of quantum rings: triangular, hexagonal and rhombus. The inner and outer edge states are clearly localized at the inner and outer boundaries of the ring. The edge states behave differently as a function of the magnetic field (magnetic flux). For example, the energy of the outer edge state decreases with increasing magnetic field, while the energy of the inner edge state increases with the magnetic field. This behavior can be understood from a semiclassical picture of the motion of the guiding centre of the edge states in a magnetic field. The guiding centre of the inner edge state moves in the same direction as the cyclotron motion, while the guiding centre of the outer edge state moves in the direction opposite to the cyclotron motion. At the anticrossing point of these two dependencies there is a coupling between the edge states.

6.2. *Electron trapping in graphene QDs*

As it was already discussed earlier, the conventional semiconductor QDs based on a confinement by the electric potential, e.g. a gate potential, cannot be realized in graphene due to Klein tunnelling. Although a confinement potential in graphene cannot localize an electron for infinitely long time, it is still possible to realize a confinement potential that can *trap* an electron for finite but relatively long time. That type of trapping exists only for electron states with transverse momentum [350,351]. The transverse momentum introduces locally a gap and corresponding classically forbidden regions, which results in tunnelling barriers and the trapping of an electron.

To illustrate the possibility of electron trapping in graphene, we consider the semiclassical dynamics of relativistic electrons in a one-dimensional confinement potential, $V(x)$. The effective semiclassical Hamiltonian for such a confinement potential takes the form [351]

$$\mathcal{H}_{\text{eff}} = \pm\hbar v_{\text{F}}\sqrt{k_x^2 + k_y^2} + V(x). \tag{99}$$

This expression shows that the transverse momentum, p_y, introduces an effective mass for the motion in the x direction. Then for a given transverse momentum there are four classical turning points, which satisfy the following equation:

$$E = \pm\hbar v_{\text{F}}|k_y| + V(x). \tag{100}$$

For a parabolic confinement potential, $V(x) = -(x/x_0)^2 U/2$, the classical turning points are given by the expressions [351]

$$\frac{x_{\text{out}\pm}}{x_0} = \pm\sqrt{2\frac{\hbar v_{\text{F}}|k_y| - E}{U}} \tag{101}$$

$$\frac{x_{\text{in}\pm}}{x_0} = \pm\sqrt{2\frac{-\hbar v_{\text{F}}|k_y| - E}{U}}. \tag{102}$$

The turning points with classically forbidden regions are shown schematically in Figure 67. The electron (hole) bounces between two inner turning points, $x_{\text{in}\pm}$, resulting in quasibound state, i.e. the resonances. These bound states have finite width due to quantum tunnelling through classically forbidden region between points x_{in} and x_{out}. Such quasibound states result in oscillations of the current through the *p–n–p* junction as a function of the gate voltage [375]. The trapping properties of one-dimensional confinement potential, e.g. a *p–n–p* junction, are suppressed in the presence of disorder. This is because the disorder makes the boundary between different regions less sharp, which introduces additional escape channels from the trapping region. Thus in the presence of disorder the widths of the quasibound states increase, which can be visible in suppression of oscillations of the current through the *p–n–p* junction with variation of the gate voltage [375].

A similar mechanism of trapping exists for the QD-type confinement potential with trapping in both x and y directions [350]. For a cylindrically symmetric confinement potential, the electron angular momentum, which is a transverse

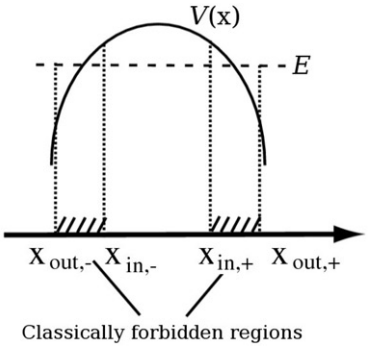

Figure 67. Trapping of an electron in a one-dimensional confinement potential, $V(x)$. The transverse momentum, p_y introduces an effective electron mass in the x direction, which results in four classical turning points, $x_{\text{in}\pm}$ and $x_{\text{out}\pm}$. Two classically forbidden regions are also indicated. The electron is trapped between the inner turning points, $x_{\text{in}\pm}$.

momentum for such a system, introduces a local gap and classically forbidden regions. We assume that the QD is cylindrically symmetric, $V(r)$, and the confinement potential does not introduce any inter-valley mixing. In that case it is enough to consider the states of a single valley only. Then the electron states are described by a two-component wave functions with the following Hamiltonian:

$$\mathcal{H} = \hbar v_{\mathrm{F}} \begin{pmatrix} 0 & k_x - \mathrm{i}k_y \\ k_x + \mathrm{i}k_y & 0 \end{pmatrix} + \begin{pmatrix} V(r) & 0 \\ 0 & V(r) \end{pmatrix}. \tag{103}$$

In the cylindrical coordinate, the corresponding Dirac equations become [253]

$$V(r)\psi_1 + \hbar v_{\mathrm{F}} \mathrm{e}^{-\mathrm{i}\theta} \left(-\mathrm{i}\frac{\partial}{\partial r} + \frac{1}{r}\frac{\partial}{\partial \theta} \right) \psi_2 = E\psi_1 \tag{104}$$

$$V(r)\psi_2 + \hbar v_{\mathrm{F}} \mathrm{e}^{\mathrm{i}\theta} \left(-\mathrm{i}\frac{\partial}{\partial r} - \frac{1}{r}\frac{\partial}{\partial \theta} \right) \psi_1 = E\psi_2, \tag{105}$$

where $\psi_1(r, \theta)$ and $\psi_2(r, \theta)$ are the two components of the wave function, and E is the eigenenergy of a stationary state. For a cylindrically symmetric confinement potential, the solution of the system of equations (104)–(105) can be expressed in the following form:

$$\psi_1(r, \theta) = \chi_1(r) \mathrm{e}^{\mathrm{i}(m - \frac{1}{2})\theta}, \tag{106}$$

$$\psi_2(r, \theta) = \chi_2(r) \mathrm{e}^{\mathrm{i}(m + \frac{1}{2})\theta}, \tag{107}$$

where $m = \pm\frac{1}{2}, \pm\frac{3}{2}, \ldots$ is the electron angular momentum. Substituting these expressions into Equations (104)–(105), we obtain

$$V(r)\chi_1 - \mathrm{i}\hbar v_{\mathrm{F}} \frac{\mathrm{d}\chi_2(r)}{\mathrm{d}r} - \mathrm{i}\hbar v_{\mathrm{F}} \frac{m + \frac{1}{2}}{r} \chi_2(r) = E\chi_1 \tag{108}$$

$$V(r)\chi_2 - \mathrm{i}\hbar v_{\mathrm{F}} \frac{\mathrm{d}\chi_1(r)}{\mathrm{d}r} + \mathrm{i}\hbar v_{\mathrm{F}} \frac{m - \frac{1}{2}}{r} \chi_1(r) = E\chi_2. \tag{109}$$

The system of equations (108)–(109) describes the electronic states of a graphene layer with confinement potential $V(r)$ [350].

The semiclassical dynamics corresponding to the system of equations (108)–(109) has been discussed in [350]. The semiclassical approach can be applied if the angular momentum of the electron is large. We are looking for a solution of the system of equations (108)–(109) in the form $\chi_1, \chi_2 \propto \exp(iq\rho)$. Then under the condition $m \gg 1$ we obtain [350]

$$[E - V(r)]^2 = \hbar^2 v_F^2 \left(\frac{m}{r}\right)^2 + \hbar^2 v_F^2 q^2. \tag{110}$$

This equation describes the semiclassical dynamics. It has two turning points which are determined by the condition $q = 0$, i.e.

$$[E - V(r)]^2 = \hbar^2 v_F^2 \left(\frac{m}{r}\right)^2. \tag{111}$$

Therefore the transverse momentum, m/r, introduces a gap (or effective mass) in the semiclassical energy dispersion law.

For a monotonic confinement potential (Figure 68), if r_0 is a solution of the equation $E - V(r_0) = 0$ then the two classical turning points can be found from Equation (111) in the following form [350]:

$$r_1 = r_0 - \Delta r_1 = r_0 - \frac{m/r_0}{F/\hbar v_F + m/r_0^2}, \tag{112}$$

$$r_2 = r_0 + \Delta r_1 = r_0 - \frac{m/r_0}{F/\hbar v_F - m/r_0^2}, \tag{113}$$

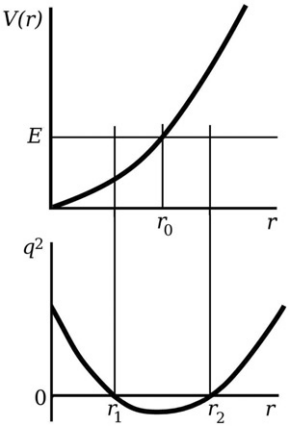

Figure 68. Schematic representation of a cylindrically symmetric confinement potential. The angular motion introduces a transverse momentum, which results in an effective electron mass. The classically forbidden region which is determined by the condition $q^2 < 0$, is realized at large values of the angular momentum. The classical turning points are r_1 and r_2. The electron is trapped inside the classical region $r < r_1$. Tunnelling through the semiclassical barrier ($r_1 < r < r_2$) determines the escape rate from the trapped region.

where $F = \mathrm{d}V(r)/\mathrm{d}r|_{r=r_0}$. The electron can freely propagate within the classical regions $r > r_2$ and $r < r_1$. The tunnelling barrier between two classical regions introduces the electron trapping in the region of the QD, $r < r_1$. Tunnelling through the classically forbidden region ($r_1 < r < r_2$) determines an escape rate from the QD (Figure 68). Under the condition $F \gg \hbar v_F m/r_0^2$, which results in the relation $\Delta r_1 = \Delta r_2 = m\hbar v_F/Fr_0$, the tunnelling exponent is given by the following expression [350]:

$$R = \exp\left(-\int_{r_0-\Delta r_1}^{r_0+\Delta r_1} |q(r)|\mathrm{d}r\right) = \exp\left(-\frac{\pi\hbar v_F m^2}{2Fr_0^2}\right). \tag{114}$$

Therefore, an efficient electron trapping occurs in a smooth confinement potential, i.e. the slope, F, should be small, and at a large angular momentum, m. For a confinement potential of the form $V(r) = (u/p)r^p$, the escape rate from the QD becomes

$$R = \exp\left[-\frac{\pi m^2}{p(E/\epsilon_p)^{p+1/p}}\right], \tag{115}$$

where

$$\epsilon_p = [(\hbar v_F)^p u/p]^{1/(p+1)}. \tag{116}$$

Then the condition for a small escape rate, i.e. a large tunnelling exponent $R \ll 1$ determines the upper limit of the energy of the strongly trapped state at a given angular momentum, m, [350]

$$E < \epsilon_p m^{2p/(p+1)}. \tag{117}$$

Therefore trapping of an electron in a QD realized through a confinement potential is due to the formation of semiclassical tunnelling barrier. The width of the classically forbidden region depends on the transverse momentum, i.e. the angular momentum, and the slope of the confinement potential. Electron trapping can be realized only in a smooth confinement potential, which means that there are no electrons trapped in the confinement potential with sharp boundaries, e.g. a box-like potential. For such a potential the slope F at the boundary of the QD is large and the tunnelling exponent is small. Another requirement for strong electron trapping is a large value of the angular momentum, m. At a small m the tunnelling barrier is narrow and the electron can easily escape from the QD.

6.3. *QDs with sharp boundaries*

The semiclassical analysis describes an electron dynamics only for large values of the angular momentum. To address the problem of electron trapping at small values of the angular momentum and in a confinement potential with sharp boundaries, the system of equations (108)–(109) should be solved exactly. In [376–378] the system

of equations (108)–(109) was analyzed in detail for a confinement potential with sharp boundaries, i.e. box-like potential, which has the following form:

$$V(r) = \begin{cases} 0 & \text{if } r < R \\ V_0 & \text{if } r > R \end{cases}, \tag{118}$$

where $V_0 > 0$ is the strength of the confinement potential and R is the radius of the QD. For such a confinement potential there are no classically forbidden regions and no semiclassical trapping barrier. At the same time it was shown that in this case there are electronic states with very small escape rate [376–378]. Electron trapping in these states is determined by the interference effects within the whole region of the QD. In this case the dependence of the electron trapping time on the parameters of the confinement potential is not exponential but a power law.

The trapped states in the confinement potential can be defined by two methods. In the first method the trapped states are considered as the resonances, which are revealed as the first-order poles of the scattering matrix in the complex energy plane or as the peaks in the scattering cross section. Here the widths of the peaks determine the lifetime of the trapped state. This method has been used in [376], where the scattering cross-section was numerically calculated for a box-like confinement potential. It was shown in [376] that sharp resonances occur only at the energy close to the confinement potential strength, i.e. $E \approx V_0$.

In the second method the trapped states are defined as the time-independent solutions of the Schrödinger equation with purely outgoing boundary conditions. The stationary solutions with outgoing boundary conditions exist only at complex energies. The trapped states in this method are considered as long-lived states in the decay process [378]. The real part of the complex energy is associated with the energy of the trapped state, while the inverse of the imaginary part of the energy determines the lifetime of the decaying state. For example, if E is the complex energy of the trapped state, then the trapping time is $\tau = \hbar/\mathrm{Im}[E]$. Such an approach to the problem of quasibound states was originally introduced by Gamow [379]. The second method allows us to find some analytical expressions which determine the trapping properties of the QD. This method has been used in [377,378]. Here the complex energies, E, of the trapped states are determined from the solution of Equations (108)–(109) with outgoing boundary conditions: $\chi_1, \chi_2 \propto \exp(\mathrm{i}kr)$ at large distance from the QD.

For the box-like confinement potential it is easy to show that the solution of Equations (108)–(109) takes the following form [378]:

$$\begin{pmatrix} \chi_1(r) \\ \chi_2(r) \end{pmatrix} = A \begin{pmatrix} J_{|m-\frac{1}{2}|}(\varepsilon r/R) \\ \mathrm{i}J_{|m+\frac{1}{2}|}(\varepsilon r/R) \end{pmatrix}, \tag{119}$$

at $r < R$ and

$$\begin{pmatrix} \chi_1(r) \\ \chi_2(r) \end{pmatrix} = B \begin{pmatrix} H^{(1)}_{|m-\frac{1}{2}|}[(\varepsilon - v_0)r/R] \\ \mathrm{i}H^{(1)}_{|m+\frac{1}{2}|}[(\varepsilon - v_0)r/R] \end{pmatrix}, \tag{120}$$

at $r > R$. Here J_n is the Bessel function of the nth order, $H_n^{(1)}$is the Hankel function of the first kind, $\varepsilon = RE/\hbar v_F$ is complex, and $\nu_0 = RV_0/\hbar v_F$. The continuity of the wave function determines the energy eigenvalue equation in the following form:

$$\frac{H^{(1)}_{|m-\frac{1}{2}|}(\varepsilon - \nu_0)}{H^{(1)}_{|m+\frac{1}{2}|}(\varepsilon - \nu_0)} = \frac{J_{|m-\frac{1}{2}|}(\varepsilon)}{J_{|m+\frac{1}{2}|}(\varepsilon)}. \tag{121}$$

The energy, ε, in this equation is complex. In terms of the complex energy, the condition of strong trapping means that the imaginary part of the energy is small. Surprisingly, in the box-like geometry of the QD there are special states in which an electron is localized; which means that the imaginary part of the energy of this state is zero and the electron lifetime is *infinitely large* [378]. These states exist only if the dimensional potential strength, ν_0, is a root of the Bessel function $J_{m-\frac{1}{2}}(\nu_0) = 0$. In this case there is a real solution $\varepsilon = \nu_0$ of Equation (121) with infinitely long trapping time.

Therefore a localized state of an electron in a QD with sharp boundary exists only if the confinement potential satisfies the following condition:

$$\nu_0 = \lambda_{n,i}, \tag{122}$$

where $n = m - \frac{1}{2}$ and $\lambda_{n,i}$ is the ith root of the Bessel function of the order $n = 0, 1, 2, \ldots$. In this case the energy of a localized state is exactly equal to the strength of the confinement potential, $\varepsilon = \nu_0$. These localized states have infinitely long trapping time and exist at both small and large values of angular momentum, m. The typical imaginary part of the energies of the other states are of the order of 1 and the corresponding trapping times are relatively short. Any deviation of the parameters of the confinement potential from the condition (122) of localization introduces an electron escape from the highly trapped state of the QD.

If the condition for localization is weakly violated, i.e. $\delta_\nu \equiv \nu_0 - \lambda_{m-\frac{1}{2},i}$ is small, then it is possible to find the imaginary part of the energy of the highly trapped states [378] from the standard perturbation theory based on Equation (121):

$$\mathrm{Im}[\varepsilon] = \frac{\pi}{2}\left(\frac{\delta_\nu}{\ln \delta_\nu}\right) \tag{123}$$

if $m = \frac{1}{2}$ and

$$\mathrm{Im}[\varepsilon] = \frac{\pi}{[2^m(m-\frac{1}{2})!]^2}\left[1 - \frac{1}{2m}\right]^{2m+1} \delta_\nu^{2m} \tag{124}$$

if $m > \frac{1}{2}$.

Electron trapping in a confinement potential with sharp boundaries is very sensitive to the profile and the parameters of the potential. By varying the parameters of the confinement potential, one can tune the trapping time within the confinement region. These parameters could be the strength of the confinement potential, the radius of the QD or the distance between the QDs in a system of coupled QDs with sharp boundaries [377].

6.4. *QDs in a magnetic field: numerical studies*

The semiclassical approach to the problem of trapped states in a confinement potential is applicable only at large values of electron angular momentum. At small angular momentum, even for a smooth confinement potential we need to go beyond the semiclassical approximation. In this case we need to solve the system of equations (108)–(109) exactly. The numerical solution of this system of equations for the confinement potential with a sharp boundary was discussed in Section 6.3. Here we consider the numerical solution of Equations (108)–(109) for a confinement potential with smooth boundary [350]. Similar to the confinement potential with a sharp boundary, the trapped states are defined as the time-independent solutions of the Schrödinger equation with outgoing boundary conditions. Such stationary solutions exist only at complex energies, where the real part of the energy is the energy of the state and the imaginary part of the energy is proportional to the escape rate from the QD, i.e. inversely proportional to the trapping time.

To introduce the outgoing boundary conditions for the system of equations (108)–(109), we consider the solution of these equations at large distances, $r \to \infty$. In this limit, due to the relation $V(r) \gg E \gg \hbar v_F/r$ the confinement potential provides the leading terms in Equations (108)–(109). Therefore, at $r \to \infty$ Equations (108)–(109) take the form

$$V(r)\chi_1 - \mathrm{i}\hbar v_F \frac{\mathrm{d}\chi_2}{\mathrm{d}r} = 0, \tag{125}$$

$$V(r)\chi_2 - \mathrm{i}\hbar v_F \frac{\mathrm{d}\chi_1}{\mathrm{d}r} = 0. \tag{126}$$

The general solution of Equations (125)–(126) can be expressed in the following form:

$$\chi_1 = C_1 \exp\left(\frac{\mathrm{i}}{\hbar v_F}\int^r V(r')\mathrm{d}r'\right) + C_2 \exp\left(-\frac{\mathrm{i}}{\hbar v_F}\int^r V(r')\mathrm{d}r'\right), \tag{127}$$

$$\chi_2 = -C_1 \exp\left(\frac{\mathrm{i}}{\hbar v_F}\int^r V(r')\mathrm{d}r'\right) + C_2 \exp\left(-\frac{\mathrm{i}}{\hbar v_F}\int^r V(r')\mathrm{d}r'\right). \tag{128}$$

The two terms in these solutions correspond to waves propagating towards the QD and away from the dot. Only the solution corresponding to the outgoing waves should be kept, i.e. only the first terms in Equations (127)–(128) should be considered. Thus the outgoing boundary conditions mean that at large distance, the functions χ_1 and χ_2 take the form

$$\chi_1 = -\chi_2 = C_1 \exp\left(\frac{\mathrm{i}}{\hbar v_F}\int^r V(r')\mathrm{d}r'\right). \tag{129}$$

This expression should be considered as the boundary condition for the system of equations (108)–(109) at $r \to \infty$. It is convenient to reformulate the boundary condition (129) in terms of new functions $f(r)$ and $g(r)$ defined by the

following expressions:

$$\chi_1 = f(r)\exp\left(\frac{\mathrm{i}}{\hbar v_\mathrm{F}}\int^r V(r')\mathrm{d}r'\right), \tag{130}$$

$$\chi_1 = -g(r)\exp\left(\frac{\mathrm{i}}{\hbar v_\mathrm{F}}\int^r V(r')\mathrm{d}r'\right). \tag{131}$$

In terms of the functions $f(r)$ and $g(r)$ the boundary condition (129) becomes $f(r\to\infty)=g(r\to\infty)$. Substituting expressions (130), (131) into the system of equations (108)–(109), we obtain

$$V(r)(f-g)+\mathrm{i}\hbar v_\mathrm{F}\frac{\mathrm{d}g}{\mathrm{d}r}+\mathrm{i}\hbar v_\mathrm{F}\frac{m+\frac{1}{2}}{r}g = Ef, \tag{132}$$

$$V(r)(g-f)+\mathrm{i}\hbar v_\mathrm{F}\frac{\mathrm{d}f}{\mathrm{d}r}-\mathrm{i}\hbar v_\mathrm{F}\frac{m-\frac{1}{2}}{r}f = Eg. \tag{133}$$

The system of equations (132)–(133) should be solved numerically with the boundary conditions $f(r=0)=g(r=0)=0$ at the origin and $f(r\to\infty)=g(r\to\infty)$ far away from the QD [350]. Such a solution exists only at complex energies. For a confinement potential of the form $V(r)=(u/p)r^p$, the complex energy spectra is shown in Figure 69 for different values of electron angular momentum. Only the states with small values of the imaginary part of the energy are shown in Figure 69, i.e. in addition to the states shown in the figure there are many continuum states with large imaginary part of the energy.

The strength of the electron confinement is determined by the ratio of the interlevel spacing, ΔE, to the imaginary part of the energy, $\mathrm{Im}(E)$. For strongly

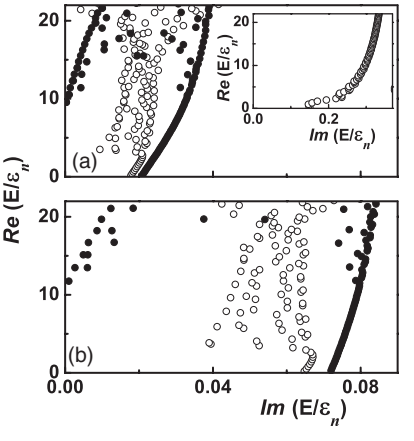

Figure 69. The real and imaginary parts of the energy spectra of an electron in a QD with a confinement potential $V(r)=(u/p)r^p$, shown for various values of the exponent p and the angular momentum m: (a) $p=2$, $m=3/2$ (open circles) and $p=2$, $m=19/2$ (solid circles); (b) $p=4$, $m=3/2$ (open circles), $p=4$, $m=9/2$ (stars) and $p=4$, $m=19/2$ (solid circles). The results for $p=2$ and $m=\frac{1}{2}$ are shown in the inset. The energy is in the units of $\epsilon_p=[\hbar v_\mathrm{F})^p\ u/p]^{1/(p+1)}$ (reproduced from [350]).

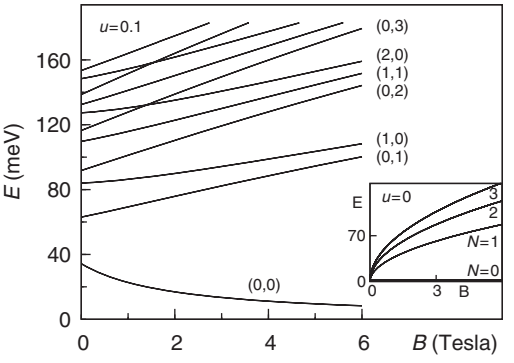

Figure 70. Energy (Fock–Darwin) spectrum of the Dirac QDs with parabolic confinement potential, $V(r) = (u/2)r^2$ is plotted for $u = 0.1$ (meV nm^{-2}) as a function of magnetic field. The numbers in the parentheses correspond to the two quantum numbers N and m, where m is the angular momentum and $N + m = n$ is the Landau level index. The energy spectrum of graphene without confinement potential, i.e. $u = 0$, is given in the inset (reproduced from [350]).

trapped states this ratio is large, while for the deconfined continuum states this ratio is of the order of 1. The formation of the confined states in the QD is already visible at angular momentum $m = 3/2$, for which the ratio $\Delta E/\mathrm{Im}(E)$ is around 50. With increasing angular momentum the electron states become more confined and the imaginary part of the energy decreases. For example, for $m = 9/2$ the ratio $\Delta E/\mathrm{Im}(E)$ is 200, while for $m = 19/2$ the ratio $\Delta E/\mathrm{Im}(E)$ is 800, i.e. the electron with these value of angular momentum can be considered as strongly trapped by the confinement potential [350]. Therefore the confined states within the QD can be observed for states with angular momentum greater than $\sim 9/2$.

Properties of the trapped states of a QD in an external magnetic field have been studied numerically in [350]. To find the energy spectra of such a system a finite set of basis wavefunctions, corresponding to an electron in uniform magnetic field, has been introduced. The basis wavefunctions have the form of Equation (8), where the Landau wavefunctions are expressed in terms of the functions with a given angular momentum, m. Then the matrix elements of the confinement potential between the basis functions are calculated and the eigenvalues and eigenfunctions of the corresponding Hamiltonian matrix are found. To suppress any escape of particles from the QD, i.e. to consider only the confined states within the QD, the basis functions were restricted only by the functions with positive energies.

The calculated low-lying energy states of the graphene QD in uniform magnetic field and in a parabolic confinement potential, $V(r) = (u/2)r^2$, are shown in Figure 71. At zero magnetic field the energy spectrum reproduces the energy spectrum of the confined states in a parabolic QD. In contrast to conventional nonrelativistic parabolic QD, which has equidistant and degenerate energy spectrum, the spectrum of QDs in graphene is not equidistant and the degeneracy of the levels is lifted. At low magnetic fields, the magnetic length, l_B, is larger than the characteristic size, $[(\hbar v_F)^2 u]^{\frac{1}{3}}$, of the confined states in the QD. In this case the magnetic field introduces a mixture between the confined states of the dot [350]. For a large magnetic field the magnetic length becomes smaller than the size of the QD and the electron states can

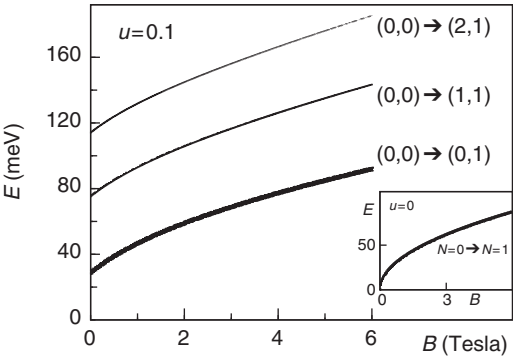

Figure 71. The dipole-allowed optical transitions in a graphene QD with a parabolic confinement potential, $V(r) = (u/2)r^2$ is shown at $u = 0.1$ (meV nm^{-2}). Only optical transitions from the ground state are shown. Inset: the optical transitions in graphene without the confinement potential, $u = 0$. The thickness of the lines is proportional to the calculated intensity. From the bottom to the top, the relative intensities are about 1.0, 0.1, 0.02, respectively (reproduced from [350]).

be considered as the Landau level states mixed by the confinement potential. In this case the inter-Landau level coupling lifts the degeneracy of the Landau levels.

The manifestation of mixing of Landau levels by the confinement potential is clearly seen in optical transitions within the QD. The optical transitions from the ground state, $(0, 0)$, of the QD to the excited states are shown in Figure 71. Without a confinement potential the only allowed transition is $(0, 0) \to (0, 1)$, i.e. from the $n = 0$ to the $n = 1$ Landau levels. The confinement potential introduces mixing of the Landau levels, which results in the allowed optical transitions $(0, 0) \to (1, 1)$ and $(0, 0) \to (2, 1)$. The lowest allowed optical transition, i.e. $(0, 0) \to (0, 1)$ transition, for parabolic confinement potential has an energy [350]

$$\Delta E = [(\hbar v_{\mathrm{F}})^2 u]^{\frac{1}{3}} + \frac{\sqrt{2}\hbar v_{\mathrm{F}}}{l_B}. \tag{134}$$

This expression reproduces the Landau level separation in graphene at large magnetic fields and inter-level separation for the confined states at zero magnetic field. The expression (134) can also be used to extract the band parameter, $\hbar v_{\mathrm{F}}$, from the optical absorption experiments in graphene in a magnetic field and a confined potential.

6.5. *Magnetic QDs*

The combination of a uniform magnetic field and the confinement electrostatic potential can produce strongly confined states [380] even in an ideal graphene system. The origin of such a confinement can be understood from the semiclassical analysis of the electron dynamics. In an uniform magnetic field, Equation (110) takes the form [380]

$$(\hbar v_{\mathrm{F}})^2 q^2 = [E - V(r)]^2 - (\hbar v_{\mathrm{F}})^2 (m/r + eBr/2)^2. \tag{135}$$

The classically forbidden region is determined by the condition $q^2 < 0$. Then the electron motion is confined, i.e. an electron cannot classically propagate at large distances, $r \to \infty$, if at large r the right-hand side of Equation (135) becomes negative. This can be realized if the confinement potential increases slower than r, e.g. becomes constant at large distance [380]. Therefore at large r the behavior of the electron is determined not by the confinement potential but mainly by the uniform magnetic field, which itself produces intrinsically confined electronic states. The electron confinement by a slow varying electrostatic potential and uniform magnetic field can also be understood as a pinning of intrinsically confined magnetic electronic states by the electrostatic potential. The advantage of this type of confinement is that it can be realized for all values of the electron angular momentum, m, and for different types of slow varying electrostatic potential, even non-cylindrically symmetric one. If the confinement potential increases as $V \propto r$ then the system shows confinement–deconfinement transitions, which is controlled by the dot parameters and the strength of the magnetic field [380]. These transitions can also be understood from the semiclassical expression (135). Indeed, if $V = v_0 r$ then from Equation (135) we obtain that the confinement of the state is determined by the sign of the expression $v_0 - \hbar v_F e B$. The electron is confined or deconfined if this expression is negative or positive, respectively.

The confinement of an electron in graphene can also be realized through inhomogeneous magnetic fields [352,353]. For a cylindrically symmetric magnetic QD, the external magnetic field is perpendicular to the graphene plane and the magnitude of magnetic field depends only on radius, $B(r)$. The Dirac equation for a two-component spinor, $\psi = (\psi_1, \psi_2)$, corresponding to a single valley takes the form

$$\vec{\sigma}\left[\vec{p} + \frac{e}{c}\vec{A}(x,y)\right]\psi(x,y) = \epsilon\psi(x,y), \tag{136}$$

where $\vec{A}(x,y)$ is the vector potential and $E = v_F\epsilon$. For a cylindrically symmetric magnetic QD, the electron angular momentum is conserved. Then the solution of the Dirac equation has the form of Equations (106)–(107) and the Dirac equation reduced to the following system of equations [352]:

$$\frac{\mathrm{d}\chi_1(r)}{\mathrm{d}r} - \frac{m + \frac{1}{2} + \phi(r)}{r}\chi_1(r) = \epsilon\chi_2 \tag{137}$$

$$\frac{\mathrm{d}\chi_2(r)}{\mathrm{d}r} + \frac{m - \frac{1}{2} + \phi(r)}{r}\chi_2(r) = \epsilon\chi_1, \tag{138}$$

where $\phi(r) = \frac{e}{c}\int_0^r \mathrm{d}r' r' B(r')$ is the magnetic flux through a disk of radius r in units of the flux quantum.

For the simple model of a magnetic QD for which $B = B_0$ outside a disk of radius R and zero inside the disk, the general solution of the system of equations (137)–(138) can be expressed in terms of the Bessel functions inside the dot and hyperbolic functions Φ and Ψ outside the dot. The continuity of the two-component wave function determines the energy eigenequation for the

magnetic QDs [352]

$$1 - |\tilde{m}|\theta(-\tilde{m})/\delta - \frac{\varepsilon l_B}{\sqrt{2\delta}} \frac{J_{m+\frac{1}{2}}(\epsilon l_B\sqrt{2\delta})}{J_{m-\frac{1}{2}}(\epsilon l_B\sqrt{2\delta})} = \frac{\mathrm{d}}{\mathrm{d}\eta} \ln \Psi(\alpha, 1 + |\tilde{m}|; \eta = \delta), \tag{139}$$

where $l_B = \sqrt{c/eB_0}$ is the magnetic length, $\delta = R^2/2l_B^2$, $\tilde{m} = m - \delta$ and $\alpha = 1 + \tilde{m}\theta(\tilde{m}) - (\varepsilon l_B)^2/2$. The solutions of Equation (139) determine the energies of the localized states of an electron within the magnetic QD. Electrons in these states are strongly confined with zero escape rate.

The many electron system in parabolic magnetic QDs, i.e. $B(r) \propto r^2$, was studied in [354]. Employing Sucher's projector formalism [381], i.e. restricting the Hilbert space to the positive-energy eigenspace for each particle, allowed the authors to obtain the energy spectra of the many electron interacting system. For a two-electron system, a singlet-triplet ground-state spin transition was observed as a function of the inter-electron interaction strength.

6.6. *Confinement of massive relativistic electrons in graphene*

Another way to overcome the problem of Klein tunnelling and to confine an electron in a graphene layer is to introduce gap in the energy dispersion, i.e. introduce a finite electron mass. Due to the presence of the gap, there are no freely propagating states (hole states) inside the barrier, which suppresses the Klein tunnelling. The effective electron mass can be introduced through a constant mass term in the Hamiltonian. The QD in this case can be straightforwardly defined through a confinement potential. The final Hamiltonian of the system has the following form [382]:

$$\mathcal{H} = v_{\mathrm{F}}\vec{p} \cdot \vec{\sigma} + \tau\Delta\sigma_z + V(x, y), \tag{140}$$

where $\tau = \pm 1$ corresponds to the two valleys K and K′, Δ is a constant mass term and $V(x, y)$ is the electrostatic confinement potential. The mass term, Δ, introduces a gap of 2Δ. The Hamiltonian (140) generates localized states which decay exponentially away from the QD. The constant mass term can be realized, for example, by introducing the underlying substrate [383].

The mass term appears also in bilayer graphene with different potentials at the two layers [184,384]. The different potentials result from the influence of doping on one of the layer or from an electric field perpendicular to the layer, i.e. by gating. In this case the mass term in the Hamiltonian has the form $((V_1 - V_2)/2)\sigma_z$. Here V_1 and V_2 are the potentials at two layers. By varying the potential difference between the layers, one can realize the QD with localized states [384]. For example, by introducing a position-dependent potassium doping, the position-dependent mass term can be introduced [384]. A special example of the position-dependent mass term in the Hamiltonian of a single layer of graphene is an infinite-mass boundary conditions [385]. The Hamiltonian of an electron in graphene layer with mass-dependent term then has the form

$$\mathcal{H} = v_{\mathrm{F}}\vec{p} \cdot \vec{\sigma} + \tau V(r)\sigma_z. \tag{141}$$

Then the infinite mass boundary conditions means that the mass of the electron is zero inside the dot, $V(r) = 0$ if $r < R$, and infinitely large outside the dot, $V(r) = \infty$ if $r > R$. For a circular confinement, the infinite-mass boundary condition has a simple form

$$\psi_2/\psi_1 = \mathrm{i}\tau \mathrm{e}^{\mathrm{i}\phi} \tag{142}$$

at $r = R$. With this boundary condition the energy eigenequation takes the form [385]

$$\tau J_{m+\frac{1}{2}}(kR) = J_{m-\frac{1}{2}}(kR), \tag{143}$$

where $m = \frac{1}{2}, \frac{3}{2}, \ldots$ is the angular momentum and $k = E/\hbar v_{\mathrm{F}}$. The states of such QDs are strongly confined. Each level has twofold valley degeneracy, which follows from the property $E(m, \tau) = E(-m, -\tau)$ [385]. There is no zero energy state, which leads to the energy gap between the states with positive and negative energies.

6.7. *QDs in bilayer graphene*

The Klein paradox which manifests in monolayer graphene indicates that it is impossible to confine electrons by electrostatic methods. This problem is circumvented in bilayer graphene, where the lifting of the band degeneracy by the gap caused by the inter-layer potential suppresses the perfect tunnelling through an electrostatic barrier [376]. Matulis *et al.* calculated the energy spectrum and lifetime (or inverse width) of quasibound states in monolayer and bilayer QDs assuming a step-like potential profile. They found that states in the bilayer with energy lower than the potential step are much narrower (i.e. are much longer-lived) than the corresponding states in the monolayer (Figure 72). The reason for this is the differing behavior of electrons incident on a potential barrier in the two forms of graphene. At normal incidence, the monolayer barrier is completely transparent, while in the bilayer the barrier always reflects the incident electron. The longitudinal component of momentum destroys this perfect behavior, but this nonetheless serves to illustrate why confinement is much better in a bilayer dot.

Similarly, Pereira, *et al.* [386] theoretically considered dots defined by gating or inhomogeneous doping in bilayer graphene. The doping is assumed to generate

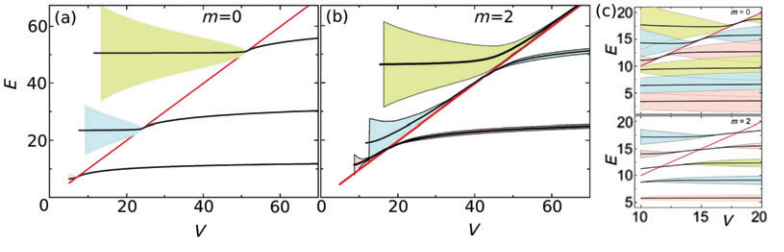

Figure 72. Quasibound states for QD in bilayer: orbital momenta (a) $m = 0$, (b) $m = 2$. The energies of these states are given by the black curves and its width (i.e. the inverse of the lifetime) by the shadowed regions. The straight slanted line corresponds to $E = V$. (c) The equivalent plots for the monolayer (Reprinted figure with permission from A. Matulis and F.M. Peeters, Physical Review B, 77, 115423, 2008 [376]. Copyright © (2008) by the American Physical Society.).

a quadratic potential which is cut off at some radius R so that the potential difference between the layers ΔU is, as a function of the radial distance r:

$$\Delta U(r) = \begin{cases} \dfrac{U_M r^2}{R^2}, & r/R < 1 \\ U_M, & r/R \geq 1. \end{cases}$$

Unusually, the $m = 0$ state (where m is the total angular momentum) is found to have the maximum of its wave function's amplitude at $r \neq 0$. In contrast, $m = 1$ is the ground state and the angular momentum phase of 2π cancels the Berry's phase of -2π. The energy levels are also not symmetric in their angular momentum: the authors find that $E(m) = -E(-m)$, in contrast to the usual semiconductor case with parabolic confinement. The energy levels are also not equally spaced, and this manifests itself in the spectrum of allowed optical transitions, where multiple frequencies will show absorption lines in a far-infrared spectroscopy measurement.

Recher *et al*. [382] study QDs in gapped bilayer graphene under the influence of a magnetic field. They show that the broken inversion symmetry of the gapped system allows bound states to be formed. They plot the dependence of the energy levels on the magnetic field, and show that the valley degeneracy is lifted in this system. The enhanced density of states near the band edge in the gapped system manifests as an increased density of levels in the dot. The trigonal warping term is also important near the band edge, although the authors argue it is less vital in the large magnetic field regime. The authors also describe the regime where the dot levels merge into the bulk Landau levels, and the combination of propagating and decaying modes that this crossover represents. A novel feature of this model is the existence of a bulk Landau level characterized by $n = 0$ which persists in the dot. When states bound to the dot cross this level, the dot becomes 'leaky' and electrons may escape from the dot. However, the energy range between

$$E_< = \frac{s\xi U}{l_B^2(\gamma_1^2 + U^2)} \pm \sqrt{\frac{U^2\gamma_1^2}{4(\gamma_1^2 + U^2)} - \frac{t_\perp^2}{l_B^4(t_\perp^2 + V^2)^2}}$$

and $E_> = E_< + U$ (where l_B is the magnetic length and $s = \mathrm{sgn}(B)$) is never crossed by this Landau level, and as such constitutes a region where well-behaved bound states are known to exist.

7. Localized states at the edges of graphene nanoribbons

Carbon systems, such as graphite, carbon nanotubes and graphene, are characterized by their π electron structure mostly controlled by the sp^2 carbon network. Bulk graphene is a zero gap semiconductor whose lattice has hexagonal symmetry with two equivalent sublattices A and B (Section 1.1). The carbon atoms belonging to the two different sublattices form equilateral triangles, therefore each sublattice is invariant under 120° rotation which preserves the D_{6h} symmetry. The band structure of bulk graphene is presented by cone-shaped conduction and valence bands touching at Dirac points (K and K′) in the Brillouin zone. Therefore, at each K-point

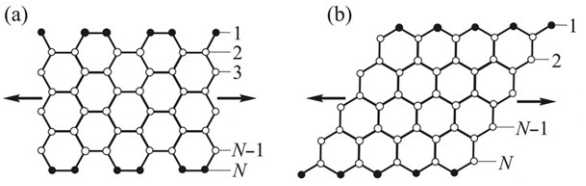

Figure 73. Graphene ribbons confined by (a) armchair and (b) zigzag edges in transverse direction. The arrows show the longitudinal (infinite) direction.

the bands are degenerate and the electronic bands $E(k)$ show linear dispersion near the K points. The Fermi level lies in the plane formed by the K points (Figure 2).

The main difference between bulk graphene and graphene nanoribbons is the presence of edges in nanoribbons. The π network of graphene nanoribbons still consists of sp^2 bonded carbons, but the carbon atoms at the edges have only two neighbors, thereby developing many sp carbon bonds and unsaturated dangling bonds. Saturation of such dangling bonds through termination by hydrogens decreases the amount of sp hybridization. Disruption of the sp^2 carbon network can also be caused by defects and dislocations, which may have less (or more) than three neighboring atoms. As a result, the electronic properties at the edges and at the defect locations are modified in comparison to that of bulk graphene. Most significantly such discontinuities modify the electronic properties of finite nanoscale graphene, which is confined by the edges from all sides. In graphite-like structures there are two basic shapes of the edges – armchair or zigzag (Figure 73). Disruption of the sp^2 carbon network at the edges generates localized states. Because the structure, lattice orientation and proportion of the sp^2 and sp hybridization of the armchair and zigzag edges are different, their electronic properties differ, particularly in the formation of localized states. The distinction of the electronic properties between the zigzag and armchair edges was initially discussed for graphite and only zigzag edges were predicted to create localized edge states near the Fermi level [387–390].

Graphene nanoribbons – idealized quasi one-dimensional systems – can be built with solely armchair or zigzag edges, i.e. the shape of graphene ribbon can be chosen in such a way that the ribbon in finite directions is confined by either the armchair or the zigzag edges (Figure 73). In this section, we consider the electronic properties of the graphene nanoribbons, both armchair and zigzag, through distribution of the localized electrons at the edges and their spin orientation. Because the localization of the edge states is influenced by many factors, such as size of the nanoribbons, edge geometry and edge termination, their effect on the electronic properties of graphene nanoribbons are included in this section as well.

7.1. *Localization of the electron density at the edges*

Armchair and zigzag graphene nanoribbons have attracted considerable attention due to their unique edge properties [391]. Initially, the electronic properties of graphene nanoribbons were investigated via the tight-binding model, also known as

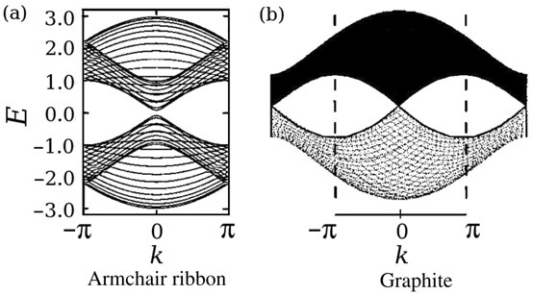

Figure 74. (a) The band structure of an armchair ribbon of width N=30 and (b) the band structure of two-dimensional graphite projected onto the armchair axis (Reprinted figure with permission from K. Nakada *et al.*, Physical Review B, 54, 17954, 1996 [391]. Copyright © (1996) by the American Physical Society.).

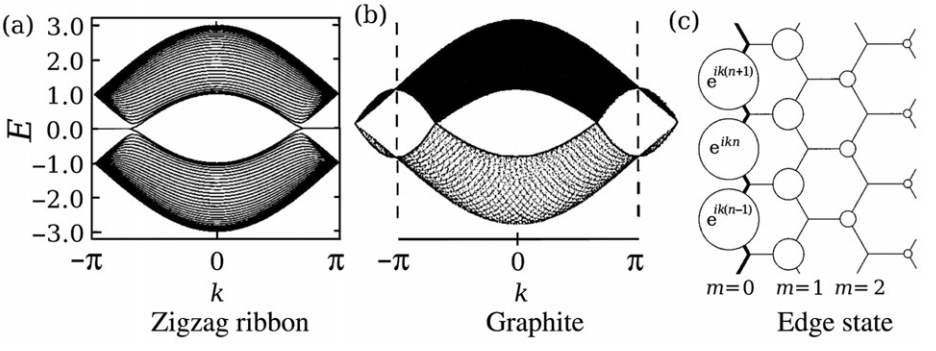

Figure 75. (a) The band structure of a zigzag ribbon of width N=30. (b) The band structure of the 2D graphite projected onto the zigzag axis. (c) An analytical solution of wave function for the localized edge state ($k = 7\pi/9$) (Reprinted figure with permission from K. Nakada *et al.*, Physical Review B, 54, 17954, 1996 [391]. Copyright © (1996) by the American Physical Society.).

the Hückel approximation [391]. In this model, the transfer integral was set as t for all nearest neighbor interactions. The dangling bonds at the edge sites were terminated by hydrogen to minimize the contribution of the sp-carbon bonds to the electronic properties. The wave vector k was replaced by the translation vector and the energy E by the transfer integral. The obtained band structure of an armchair ribbon of width $N = 30$ is displayed in Figure 74 (a). For comparison, the band structure of two-dimensional graphite projected onto the armchair axis is also shown in Figure 74 (b), where the dashed lines are the boundaries of the first Brillouin zone. The band structure of an armchair ribbon is found to be similar to that for two-dimensional graphite: in both cases the conduction and valence bands approach the Dirac points. The main difference is a small direct gap for nanoribbons, whose size was found to be controlled by the nanoribbon width. An increase in N was shown to close the gap.

Similar calculations have been performed for zigzag nanoribbons. The band structure of a zigzag nanoribbon and its comparison with that of 2D graphite

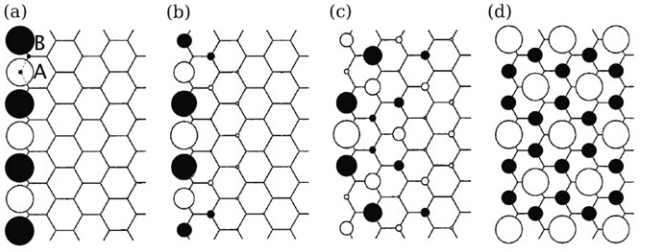

Figure 76. The real part of the wave function obtained from the analytical solution for the semi-infinite graphite. (a) $k=\pi$, (b) $k=8\pi/9$ (c) $k=7\pi/9$ (d) $k=2\pi/3$. Here, the shaded and open circles denote the different sign of the wave functions. A and B denote the two sublattices (Reproduced from M. Fujita *et al.*, Journal of the Physical Society of Japan, 65, 1920 1996 [390]. Copyright © (1996) The Physical Society of Japan).

projected onto the zigzag axis are shown in Figure 75. For graphite, the cone-shaped conduction and valence bands touch at $k \simeq \pm 2\pi/3$ corresponding to the Dirac points, while in graphene after touching these bands remain degenerate. Therefore, the flatness of the conduction and valence bands begins at $k \simeq 2\pi/3$ and extends up to $k=\pi$. The wave functions corresponding to these bands are completely localized on the zigzag edges. The analytical solution for the wave function localized at the zigzag edges, which has been derived within the method of the linear combination of atomic orbitals where the translational symmetry was considered, is presented in Figure 75(c). The charge density at the zigzag edge for each non-nodal site was found to be proportional to $[2\cos(k/2)]^{2m}$, where m is the lattice site ($m=0$ for zigzag edge). In Figure 75(c), the circle radius was chosen to be proportional to the charge density. It was observed that the charge density diminishes with increasing distance from the edge sites and the damping factor is $-2\cos(k/2)$ per zigzag chain. Due to the translational symmetry considered in the model, the analytical solution implements non-zero charge density only for the sites belonging to one graphene sublattice.

For the zigzag nanoribbon, an analytical solution for the wave functions corresponding to the flat bands within the interval $2\pi/3 \leq | k | \leq \pi$ was also derived in [390]. The alteration of the real part of the wave function with the reduction of wave vector k is presented in Figure 76. The wave function obtained for $k=\pi$ is completely localized on the edges and starts to penetrate into the inner sites for decreasing k. The extended state, when the wave function is completely delocalized over the graphene structure, is for $k=2\pi/3$.

The localized states at the zigzag edges are distinguished by a peak of the density of states near the Fermi level, whose amplitude depends on the size of the ribbon and is found to decrease with increasing nanoribbon size [391] (Figure 77). The peak in the density of states almost disappears with increasing nanoribbon width up to $N=51$. The structure of the zigzag edge is found to be responsible for the appearance of localized edge states close to the Fermi level.

7.2. *Experimental evidence for localized edge states*

The existence of localized states only at zigzag edges, as predicted theoretically, received experimental validation later [392–395]. In the first work, where

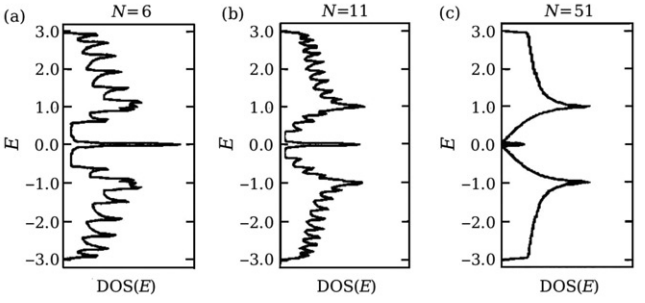

Figure 77. (a) Density of states of the zigzag nanoribbons of different width: (a) $N=6$, (b) $N=11$, (c) $N=51$ (Reprinted figure with permission from K. Nakada *et al.*, Physical Review B, 54, 17954, 1996 [391]. Copyright © (1996) by the American Physical Society.).

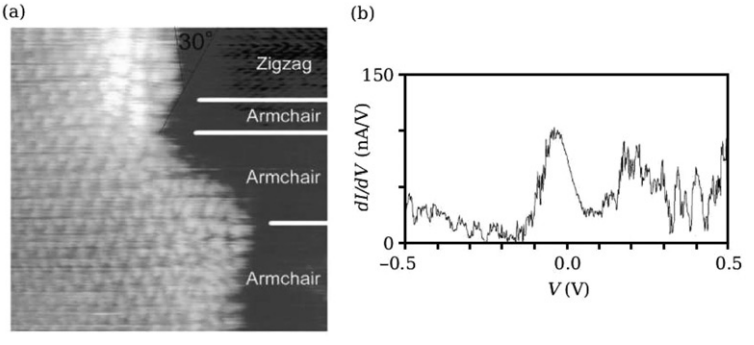

Figure 78. (a) The image of the zigzag and armchair edges ($9 \times 9\,\text{nm}^2$) obtained by scanning tunneling microscopy. The bright points were attributed to the top of the zigzag edges of the monolayer graphite. (b) dI/dV data from scanning tunnelling spectroscopy at the zigzag edges (Reprinted figure with permission from Y. Kobayashi *et al.*, Physical Review B, 71, 193406, 2005 [393]. Copyright © (2005) by the American Physical Society.).

investigation of the edge properties was performed by scanning tunnelling spectroscopy, the peak in the local density of states in the energy range of 90–250 meV above the Fermi level was observed for hydrogenated graphite [392]. The peak has appeared close to a monolayer edge ($\leq$1.5 nm) while the peak intensity kept growing as the conducting tip approached the edge. Moreover, close to the monolayer edge, bright areas of nearly atomic size were observed on images from the scanning tunnelling microscopy. The brightness indicated the efficiency of the tunnelling current between the conducting tip and the graphite surface. Since the tunnelling current is a function of the local density of states, it was concluded that these bright areas can be generated by localized electrons. The main disadvantage of that experiment was that the nature of the edges was unclear: the type of edges generating bright spots could not be distinguished.

However, in subsequent experiments [393,394] it was clearly shown that localized states occur only at the zigzag edges [Figure 78]. The contrasting bright spots were found to appear at the top part of the zigzag edges. The different edges were distinguished from application of the hexagonal lattice to the images. Moreover,

new data were also obtained for formation of the peak in the local density of states on dI/dV versus bias voltage curves. In contrast to the first experiment where the peak was shifted by 90–250 meV relative to the zero voltage [392], the latter experiments have shown an appearance of the peak at negative bias voltages in the range of -100 to -20 meV [394] and in the range of -30 meV [393]. It was also confirmed that the intensity of the peak depends on the distance from the edge [394]. Therefore, the peak almost disappears when the distance exceeds 3.5 nm [394] against 1.5 nm in [392]. The intensity and width of the peak were also found to be dependent on the type of graphite [394]. A sharp peak of high intensity was seen for the ZYX exfoliated graphite with maximum amplitude at ~ -25 meV, while for the highly oriented pyrolytic graphite the peak was broad with maximum at ~ -0.40 meV. In another experiment [396] on graphene sheets employing Raman spectroscopy the blue shift of the G band relative to its position for graphite oxide has been observed and attributed to the alteration of the pattern of the single-double carbon bonds at the zigzag edges of graphene sheets, in particular to the formation of the sp^3 carbons [396].

The experimental data therefore clearly confirmed that only the zigzag edges are responsible for the occurrence of localized states in monolayer graphite, thereby validating the theoretical prediction for graphene. However, the experiments have also shown that the peak of the density of states is shifted relative to zero voltage, i.e. indicating a shift of the energy band of the localized states relative to the Fermi level, which was not foreseen in the theoretical studies [391]. It was proposed much later that this shift of the energy bands is a result of doping of graphene through its interaction with the adsorbates in the gaseous environment or with other materials, such as the contacts or the substrate [397,398]. For example, exposure of the graphene sample to NO_2 gas was found to shift the Hall resistance and the minimum of the density of states towards higher positive gate voltages with increasing NO_2 concentration [397]. Similarly, the shift of the point where the resistance of the graphene monolayer samples reach the maximum relative to zero voltage due to doping by dipolar adsorbates has indeed been observed [398]. The problem of doping by external sources and its influence on the electronic properties of graphene will be considered in Section 8.

7.3. *Stabilization of the edge states*

7.3.1. *The nearest neighbor interactions*

The flat conduction and valence bands induced by the localized states at the zigzag edges remain degenerate and totally dispersionless for $2\pi/3 < k < \pi$. Therefore, the degenerate bands and high density of states at the Fermi energy possessing a peak in the local density of states suggest an instability of these localized states. Experimental observation of a shift of the peak away from the Fermi level [392–394] is evidence of such an instability. Studies of localized states by first-order perturbation theory for the tight-binding Hamiltonian have demonstrated the role of the nearest neighbor interactions, γ_0, and the next-nearest neighbor hopping processes, γ_n, in the stabilization of these edge states [399]. The band structures of graphene obtained with and without contributions from next-nearest neighbor interactions are

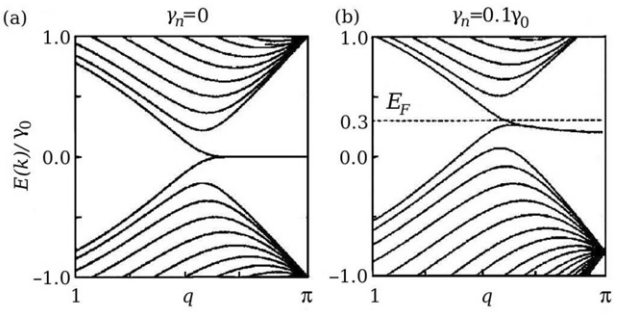

Figure 79. The energy band structure of the zigzag nanoribbon: (a) with nearest neighbor interactions $\gamma_0 = 3.0\,\text{eV}$ and (b) with both nearest neighbour $\gamma_n = 0.1\gamma_0$ and next-nearest neighbor interactions (Reprinted figure with permission from K. Sakaki *et al*., Applied Physics Letters, 88, 113110, 2006 [399]. Copyright © (2006) American Institute of Physics.).

presented in Figure 79. In the case when the next-nearest neighbor interaction is zero, the Fermi level is located at the zero energy ($E(k)/\gamma_0 = 0$), while the conduction and valence bands are flat after they meet at $q = 2\pi/3$ at the Fermi level, where q is the wave vector. If the next-nearest neighbor interactions γ_n are taken into account, the shift of the energies of the whole band structure and the Fermi level occurs. The energy shift of the band structure has been evaluated as $\Delta E \approx \gamma_n(2\cos q + 1)$. The magnitude of ΔE is maximum when $q = \pi$, thereby generating a stronger stabilization at the edges and larger shift of the bands corresponding to the localized states. If the value of the hopping integral is not zero ($\gamma_n = 0.1\ \gamma_0$ in Figure 79 (b)), the entire band structure including the Fermi level is shifted up on the energy scale $E(k)/\gamma_0$ in such a way that the nearly flat band of the localized states is found to be located below the Fermi level (Figure 79(b)). The localized states at $q = \pi$ exhibit a sharp peak in the local density of states with a maximum at the Fermi level, which is also shifted to negative energy by the stabilization effect. The lowering of the peak amplitude of the local density of states has been seen as one moves away from the edges, and diminishing of the peak when the distance exceeds 2.5 nm is in good agreement with the experimental data (~3.5 nm in [394]).

In the next paper by the same authors, the stabilization of the localized states at the edge has been attributed to the presence of a deformation potential at the edges and the interaction between the magnetic field induced by the localized states and pseudospin polarized nature of these states [400]. The local lattice deformation was considered through the weak next-nearest neighbor interactions at the edges. It was found that the next-nearest neighbor interactions break the particle-hole symmetry in graphene, thereby stabilizing the edge states. Band structure calculations performed for different magnitudes of the deformation stress at the edges have shown that undeformed graphene (zero stress) has a band structure with cone-shaped conduction and valence bands meeting at the K points. For zigzag nanoribbons if the stress at the edges is insignificant, a narrowing of the band gap occurs for $q > 2\pi/3$, while an increase of the stress leads to additional gap narrowing and finally to band closing and flattening of the bands for $q \geq 2\pi/3$. In other theoretical work [401] the deformation of the carbon bonds at the edges was predicted to influence the size of the band gap as well. Based on the results indicating a strong effect of the

deformation stress on the electronic properties, it was predicted that not only the stress at the edges, but also the external stress applied to the undeformed graphene, impurities, vacancies and external magnetic field may induce lattice deformation thereby stabilizing the localized states [400].

The edge stress occurs not only at zigzag edges, but also at armchair edges. Investigations of the compressive edge stress at armchair and zigzag edges performed with the density functional theory (DFT) have shown the dependence of the stress value on the type of edges [402]. The nature of the C–C bonds at the armchair and zigzag edges is different. The C–C bond of length $\sim$1.24 Å at the armchair edges exhibits a higher rate of sp hybridization and higher charge density than that at the zigzag edge of length $\sim$1.37 Å, against the C–C bond of length $\sim$1.42 Å possessing sp^2 hybridization of bulk graphene [403]. As a result, the compressive edge stress at the armchair edges is found to be larger than that at the zigzag edges, while termination of the dangling bonds by hydrogen provides almost stress-free edges [402]. In terms of the edge energy the armchair and zigzag edges are different as well. According to the theoretical [402,403] and experimental investigations [395], the energy of the armchair edge is much lower than that of the zigzag edge. It was also theoretically predicted that a simple reconstruction of the zigzag edge leads to significant lowering of its energy [404] and, therefore, to its structural stabilization. The activation barrier of the applied reconstruction was found to be only 0.6 eV, indicating the metastability of the zigzag edge at room temperature. Therefore, it was concluded that the clean zigzag edges would rarely exist [403] and this can be a way to perform the edge-selective termination of the dangling bonds. Experimental evidence for the formation of stable reczag graphene edges due to reconstruction of the zigzag edges has been reported in [405].

7.3.2. *Coulomb interactions*

Coulomb interactions have also been considered for understanding the mechanism of stabilization of the localized states. Simulations performed for graphite ribbons with the Hubbard model using unrestricted Hartree–Fock approximation have shown that magnetic polarization resulting from electron–electron interactions between the spin-polarized states may lead to spontaneous ordering of the spins of the electrons localized at the zigzag edges [390]. Further investigations have shown that a large magnetic moment occurs at zigzag edges even for weak Coulomb repulsion, while no magnetic structure has been found at armchair edges. For the border atoms at the zigzag edges, maximum magnetization was observed, while a move to the inner site of the ribbon reduces the magnitude of the magnetization due to the diminishing density of the localized states. Magnetic ordering of the spin states at the zigzag edge interfaces for a ribbon of width $N = 10$ is presented in Figure 80. The border atoms at the two opposite zigzag edges belong to different sublattices. According to the wave function distribution presented in Figure 76(a), the wave function localized on one edge is nonzero only for the A sublattice, and the increase of the magnetic moment selectively on this sublattice leads to the formation of a local ferrimagnetic spin configuration. The localized state on the opposite zigzag edge belongs to the B sublattice and the spin orientation of the magnetic states localized on the B sublattice is opposite to that on the A sublattice, preserving the total zero

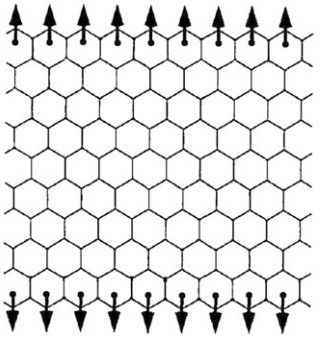

Figure 80. Spin ordering at the edges in the zigzag ribbon for $U/t = 0.1$, where U is the on-site Coulomb repulsion and t is the transfer integral (Reproduced from M. Fujita *et al.*, Journal of the Physical Society of Japan, 65, 1920, 1996 [390]. Copyright © (1996) The Physical Society of Japan.).

magnetization of the graphite ribbon. It was noted that the nanometer-scale size of the graphite fragments is the main requirement for spontaneous spin ordering.

The contribution of Coulomb interactions to the stabilization of the ferromagnetic state has been also considered in later works [406–409]. The results reported in [406] have shown that graphene sheets can have two ferromagnetic phases. One is characterized by the strong magnetization and maximally polarized spin (Nagaoka ferromagnetism), while the other is a weak ferromagnetic state. Moreover, strong Coulomb interactions in conjunction with high electron density at the lattice site (which is higher at the edges) can lead to an antiferromagnetic phase, while weak Coulomb interactions will switch the system to a paramagnetic state. In [407] it was shown that the exchange interactions between Dirac fermions can be the stabilizing factor for the ferromagnetic phase. The transition from the paramagnetic phase to the ferromagnetic one for pure graphene was predicted to occur at low strength of electron–electron interactions, and doping was found to increase the magnitude of the interactions required for the transition. The effect of electron–electron interactions and the doping of graphene lattice on the transition to a ferromagnetic state was also investigated in [409], but the reverse transition from the ferromagnetic to the nonmagnetic state was seen to occur only when large hole doping was applied.

The charge polarization process was also considered as an alternative mechanism for stabilization of the ferromagnetic state for the localized states [410–412]. In the case of the formation of the charge polarized state, the Coulomb interaction between the nearest sites was shown to be responsible for stabilization of this state, which on the opposite zigzag edges is distinguished by the electrical charges characterized by the opposite sign [410]. Therefore, the charge polarized state has a finite electric dipole moment directed from one zigzag edge to the other. The on-site Coulomb interaction has been found to trigger the formation of the spin-polarized state competing with a charge-polarized state. The external electric field due to the coupling with the internal dipole moment leads to stronger stabilization of the charge polarized state, that can make it energetically favorable as compared to the spin-polarized state [410,413]. However, Pisani *et al.* [412] have indicated that

according to the first-principles calculations the charge polarized state is highly metastable.

7.4. *Spin ordering, symmetry and band gap*

The concept of spontaneous spin polarization of the localized states at zigzag edges has received wide attention. A better understanding of the spin behavior was later provided by many research groups, and is the main subject of the present section, where the influence of spin ordering of the localized states on the magnetism of graphene nanoribbons and on the stabilization of the ground state is considered.

The first-principles calculations were used in [414] to study magnetism in graphene nanoribbons. The spin ordering along the zigzag edges was described by the three states (Figure 81): (i) ferromagnetically ordered spins along each zigzag edge and between the zigzag edges (FM-F), (ii) ferromagnetically ordered spins along each zigzag edge but with opposite spin direction between the zigzag edges (FM-A) and (iii) antiferromagnetically ordered spins along the zigzag edges but with spin alignment between the edges (AF-E). Calculations of the total energy performed with the DFT method based on the local spin-density approximation have shown that FM-A is the lowest energy state characterized by a magnetic moment of $m = 1.28\mu_B$ per edge atom, where μ_B is the Bohr magneton. The next energetically preferable state is the FM-F state with magnetic moment of $m = 1.19\mu_B$ per edge atom, whose total energy is higher than that of FM-A by $\sim$2.3 meV per edge atom. The total energy of the AF-E state is higher than that for the FM-A state by 81.4 meV per edge atom, while the magnetic moment of the AF-E state is $m = 0.82\mu_B$ per edge atom. The huge difference between the total energies of the FM-A and the AF-E states is the result of destructive interference between the spin-up and spin-down tails of the localized states in the AF-E state. The destructive interference at the inner sites of the graphene nanoribbon is also responsible for the stabilization of the FM-A

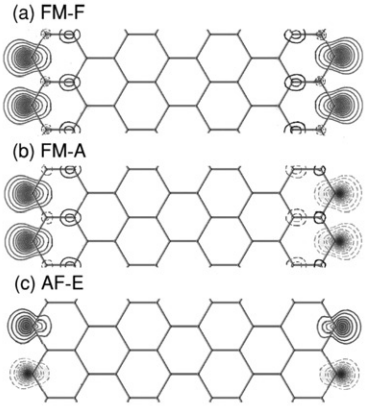

Figure 81. The electronic spin densities of (a) FM-F, (b) FM-A and (c) AF-E states in the graphitic strips. The solid line indicates the spin-up density, and the dashed line is for spin-down density (Reprinted figure with permission from H. Lee *et al.*, Physical Review B, 72, 174431, 2005 [414]. Copyright © (2005) by the American Physical Society.).

in comparison to the FM-F. The energy difference between FM-A and FM-F decreases with increasing nanoribbon width as a result of the reduction of the density of states at the inner sites that suppress the destructive interference. However, it was found [362,412] that the energetic preference of the spin-polarized state over the nonmagnetic state increases with increasing ribbon size. Several reports have confirmed the FM-A state to be the lowest energetic state of graphene [362,412,414–416].

The electronic structure of the FM-A and FM-F states are displayed in Figure 82 [412]. The border atoms at opposite zigzag edges belong to different sublattices. In the spin-polarized state, if the spin ordering between two zigzag edges is ferromagnetic, the sublattice symmetry is preserved and as a result the band gap vanishes for the FM-F state (Figure 82(a)). For the FM-F state the spin-up and spin-down bands cross each other close to the Fermi level without the formation of the electron pair at $k = 2\pi/3a$. For $k \geq 2\pi/3a$, the energy band of the spin-up state is located below the Fermi level, while for the spin-down state, in contrast, the band is located above the Fermi level.

For the FM-A state (see the band diagram in Figure 82(b)), the sublattice symmetry is broken due to the antiferromagnetic ordering of the spin states between the zigzag edges, whose border sites belong to different sublattices. Therefore, over the whole structure the spin-up state is completely localized on the A sublattice, while the spin-down state is localized on the B sublattice, making a singlet pairing between the neighboring sites. The antiparallel spin alignment of the localized states

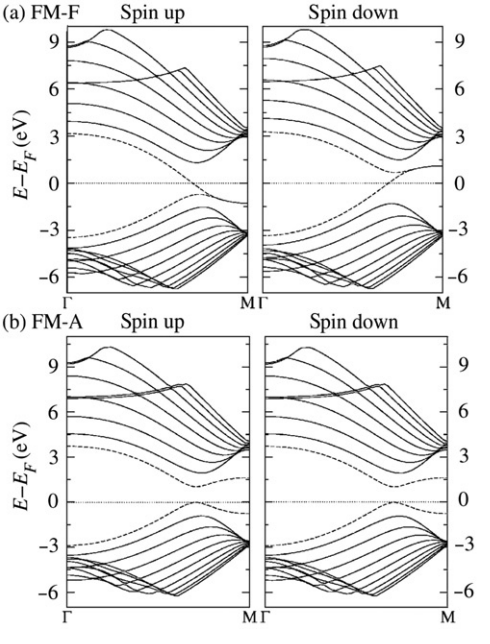

Figure 82. The band structure of the spin-polarized states (a) FM-F and (b) FM-A of the graphene nanoribbons (Reprinted figure with permission from L. Pisani *et al.*, Physical Review B, 75, 064418, 2007 [412]. Copyright © (2007) by the American Physical Society.).

between the opposite zigzag edges breaks the sublattice symmetry because carbon atoms possessing the localized states belong to different sublattices, thereby opening a gap at $k = 2\pi/3a$. An increase in the width of the zigzag ribbon leads to a reduction of the gap following an algebraic decay as $1/N$, i.e. with increasing distance between opposite zigzag edges. For $N \to \infty$ the valence and conduction bands tend to be degenerate, but the spin-polarized edges still would not show the inter-edge magnetic order. The hopping integral t and the on-site Coulomb repulsion U used in earlier works within the Hubbard model have been calculated within the DFT theory [412]. The values within the gradient corrected functional PBE and local-density approximation LSDA are t=2.5 eV and $U \sim t$.

Therefore, the lowest energy state of graphene nanoribbons is expected to have ferromagnetic ordering of the localized spin states along the zigzag edge and antiparallel spin orientation between the opposite zigzag edges, thereby breaking the sublattice symmetry and opening a gap. In this state both the band gap and the destructive interference between the spin-up and spin-down tails of the localized states decrease with increasing width of the zigzag nanoribbons. In [416], the antiparallel spin orientation at the opposite zigzag edges was also found to form the states characterized by zero total spin and a lower energy with respect to both the kinetic and interaction energies. However, in [411] the ground state of zigzag nanoribbons of regular rectangular shape was shown to have the high spin state if the many-body configuration interaction within the Hubbard Hamiltonian is taken into account. It was found that the charge polarization rather than spin-polarization is preferable in this case. For the charge polarized state, the spin-up and spin-down states are not localized at the edges but rather mixed through the nanoribbon lattice, while the electron density prefers to accumulate at the edges. As a result, the ground state of the armchair ribbon is a singlet and that of the zigzag ribbon is a high spin state, both showing the insulating behavior. Moreover, doping of graphene by *p*-type or *n*-type charge carriers [417] and oxidation of the edges [418] were found to destroy the magnetism of zigzag nanoribbons.

7.5. *Band gap: confinement effect and edge shape*

In addition to spin ordering between the edges, the shape of graphene edges also contributes significantly to the band structure. For localized states, the width of an armchair ribbon was shown to control its band gap [361,391,401,403,419–431]. Initially, the influence of the width on the electronic structure of graphene was reported in [391], where the band structure calculations were performed within the Hubbard model for armchair ribbons (Figure 83). Here the ribbon width dictates whether the band gap is semiconducting or metallic. The insulating band gap has a tendency to decrease with growing structure size due to the decrease of the weight of the edge states in the normalized density of states. However, for zigzag nanoribbons, where the flat band occurs for $2\pi/3 \leq |k| \leq \pi$, the width has not been found to bring any significant changes into its electronic properties.

Investigation of the electronic structure of graphene ribbons performed with the first-principles methods has clearly indicated the role of graphene size on its properties. Several groups [403,419–425,428–430,432] have seen the oscillatory

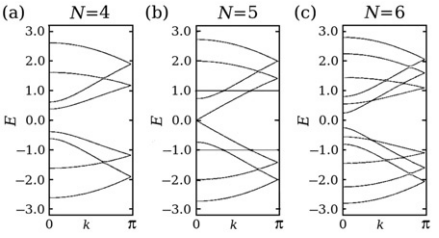

Figure 83. The band diagram of armchair ribbons, whose structure is presented in Figure 73(a), for various widths N (a) $N=4$, (b) $N=5$ and (c) $N=6$. The energy E is scaled by the transfer integral and the wave number k is normalized by the primitive translation vector of the graphene ribbon (Reprinted figure with permission from K. Nakada *et al*., Physical Review B, 54, 17954, 1996 [391]. Copyright © (1996) by the American Physical Society.).

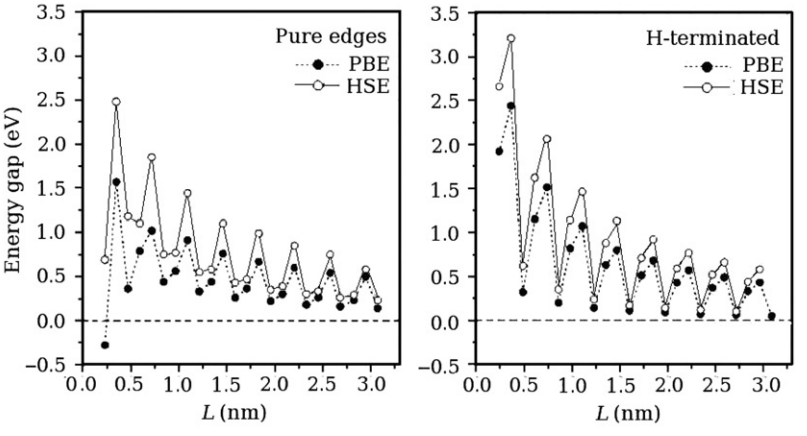

Figure 84. The dependence the size of the band gap on the ribbon width for pristine and hydrogen-terminated armchair ribbons (Reprinted with permission from V. Barone *et al*., Nano Letters, 6, 2748, 2006 [420]. Copyright © (2006) by the American Chemical Society.).

behavior of the size of the band gap on the width of the armchair nanoribbon. The period of oscillations as N varies is three. The results of DFT calculations performed with the PBE and HSE approximations for nanoribbons with pure edges or edges passivated by hydrogen atoms (to saturate the dangling bonds) are presented in Figure 84. The data were separated in three groups: the points of envelope of the maxima, of the minima and intermediate points. The envelope of the maxima was described as $N=3p+1$, where p is the positive integer number, intermediate points as $N=3p$ and the minima as $N=3p+2$ [419]. The points of the minima were found to belong to the metallic state, while both intermediate and maxima points are characterized as semiconductor states. Hydrogen termination, which takes care of the dangling bonds, changes the obtained dependence so that the intermediate points are shifted closer to the envelope of the maxima in comparison to the pristine edges, where they are located closer to the envelope of the minima. In other work, the shift of the intermediate points away from the envelope of the maxima has been obtained for graphene with hydrogen-terminated edges [433].

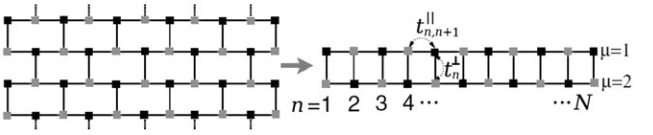

Figure 85. The periodic ladder (left) is topologically equivalent to the armchair ribbon structure in the tight-binding approximation. The condition $k=0$ is a special case when the periodic ladder (left) can be folded into a two-leg ladder (right) (Reprinted figure with permission from Y.-W. Son *et al.*, Physical Review Letters, 97, 216803, 2006 [419]. Copyright © (2006) by the American Physical Society.).

The influence of the edges on the band gap size has been found to remain for ribbon lengths up to few micrometers [435].

The periodicity of the electronic properties of armchair graphene is a result of the nature of the graphene lattice. To explain this phenomena, Son *et al.* [419] proposed to represent graphene by a lattice model describing the armchair nanoribbons within the tight-binding approximation (Figure 85). The Hamiltonian describing the electronic interactions in the longitudinal, μ, and transverse, n, directions within the lattice model is

$$\mathcal{H} = \sum_{n=1}^{N}\sum_{\mu=1}^{2}\varepsilon_{\mu,n}a^{\dagger}_{\mu,n}a_{\mu,n} - \sum_{n=1}^{N}t^{\perp}_{n}(a^{\dagger}_{1,n}a_{2,n} + h.c.) - \sum_{n=1}^{N-1}\sum_{\mu=1}^{2}t^{\parallel}_{n,n+1}(a^{\dagger}_{\mu,n}a_{\mu,n+1} + h.c.), \tag{144}$$

where $\varepsilon_{\mu,n}$ are the site energies, $t^{\parallel}_{n,n+1}, t^{\perp}_{n}$ are the nearest neighbor hopping integrals, $a_{\mu,n}$ is the annihilation operator of π electrons on site μ, n. It was assumed that the charge transfer integrals at the borders are $t^{\perp}_{1} = t^{\perp}_{N} \equiv (1+\delta)t$ and the site energies $\varepsilon_{\mu,1} = \varepsilon_{\mu,N} \equiv \varepsilon_0$, while inside the graphene structure $t^{\perp}_{n} = t^{\parallel}_{n,n+1} \equiv t$ and $\varepsilon_{\mu,n} = 0$, regardless of μ. Therefore, the edge effect has been taken into account through the modification of the site energies ($\varepsilon_{\mu,1}$ and $\varepsilon_{\mu,N}$) and charge transfer integrals ($t^{\perp}_{1}$ and $t^{\perp}_{N}$). The model Hamiltonian was solved [419] perturbatively with the energy gaps

$$\begin{aligned}
\Delta_{3p} &\simeq \Delta^{0}_{3p} - \frac{8\delta t}{3p+1}\sin^2\frac{p\pi}{3p+1},\\
\Delta_{3p+1} &\simeq \Delta^{0}_{3p+1} + \frac{8\delta t}{3p+2}\sin^2\frac{(p+1)\pi}{3p+2},\\
\Delta_{3p+2} &\simeq \Delta^{0}_{3p+2} + \frac{2|\delta|t}{p+1},
\end{aligned} \tag{145}$$

where $\Delta^{0}_{3p} = t[4\cos\frac{p\pi}{3p+1} - 2]$, $\Delta^{0}_{3p+1} = t[2 - 4\cos\frac{(p+1)\pi}{3p+2}]$, $\Delta^{0}_{3p+2} = 0$ are the gaps for ideal ribbons terminated at $\delta = \varepsilon_0 = 0$. The solution suggests that armchair ribbons with lattice deformation at the edges have a nonzero band gap such that $\Delta_{3p+1} > \Delta_{3p} > \Delta_{3p+2}$. However, this dependence was found to work only when the characteristic length of the deformation is less than the ribbon width [425].

The periodicity of the electronic structure of armchair ribbons lies in the change of shape of the armchair edges with increasing N. It has been shown that such changes initiate a shift and replacement of the subbands along the energy axis [425].

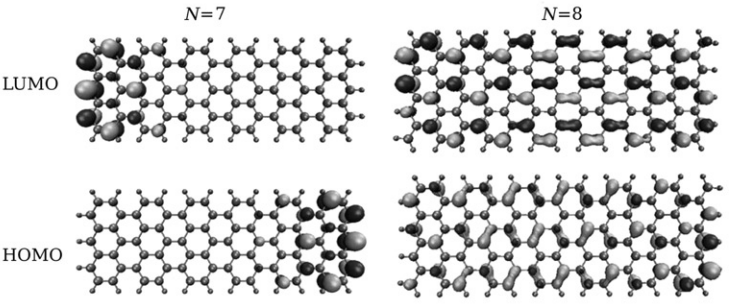

Figure 86. The spatial projection of the LUMO and HOMO molecular orbitals plotted for different zero-dimensional graphene nanoribbon: semiconductor ($N=7$) and metallic ($N=8$) (Reprinted with permission from P. Shamella *et al*., Applied Physics Letters, 91, 042101, 2007 [423]. Copyright © (2007) by the American Institute of Physics.).

If the subbands are labelled by the quantum number q, then the eigenenergy E_c in the center of the first Brillouin zone ($k=0$) is

$$E_c = \pm t\left|2\cos\frac{q\pi}{n+1}+1\right|. \tag{146}$$

For the metallic ribbon ($N=3p+2$), the first conduction or valence band is $q_1=2p+2$, the second one corresponds to $q_2=2p+3$ while the third subband is $q_3=2p+1$. The same analysis for one of the semiconductor ribbons where $N=3p+1$ gives $q_1=2p+1$, $q_2=2p+2$, and $q_3=2p$, while for the second semiconductor ribbon with $N=3p$ we have $q_1=2p+1$, $q_2=2p$, and $q_3=2p+2$ [425]. Therefore, the order of the subbands is changed with the modification of the width of the armchair nanoribbon. Additional confirmation has been obtained in [423,428], where localization of the lowest unoccupied molecular orbital (LUMO) and the highest occupied molecular orbital (HOMO) were found to be a function of the ribbon size. A good example that clearly shows the difference of the electron density distribution of the LUMO and HOMO orbitals between the semiconductor ($N=7$) and the metallic ($N=8$) cases is presented in Figure 86 for zero-dimensional graphene flakes. According to the density distribution, the semiconductor behavior ($N=7$) occurs when the HOMO and LUMO are strongly localized at the opposite zigzag edges. These localized states can be assigned to the $q_1=2p+1$ subbands ($q=5$ if $p=2$) for $N=3p$ and $N=3p+1$ armchair ribbons. For metallic ribbons ($N=3p+2$) assigned to $q_1=2p+2$ subband ($q=6$ if $p=2$) [425], the LUMO and HOMO are delocalized (extended) states (see $N=8$ in Figure 86), i.e. they are distributed over the whole graphene surface. The electron density distribution of the HOMO and LUMO orbitals for a one-dimensional armchair nanoribbon is also different when the system is metallic ($N=3p+2$) or semiconducting ($N=3p+1$ or $N=3p$) [428].

Clearly, the metallic or semiconductor states of graphene result from the ordering of the electronic bands near the Fermi level. For the semiconductor behavior, the HOMO and LUMO are formed by localized states belonging to the subband of $q_1=2p+1$ ($q=5$ if $p=2$), while the delocalized states belonging to subband of $q_1=2p+2$ are shifted deeper into the conduction and valence bands, thereby

becoming HOMO-2 and LUMO+2 if $N = 3p$ and HOMO-1 and LUMO+1 if $N = 3p + 1$. Opposite behavior is observed for the metallic ribbon, where the HOMO and LUMO are composed of the delocalized states $q_1 = 2p + 2$, which replaces the localized states by shifting them deeper into the conduction and valence bands. For the metallic behavior, the crossing of the bands near the Fermi level is similar to that of the bulk graphene, where the conduction and valence bands meet at the K points in the Brillouin zone. However, for armchair nanoribbons, the strong confinement effect increases the band gap for the semiconducting states ($N = 3p$, $N = 3p + 1$) and opens a gap for the metallic state ($N = 3p + 2$). It should be mentioned that there is another point of view for the increase of the gap with the reduction of the width of the armchair nanoribbons. In [401] it was shown that the bond deformation which is dominant at the edges is responsible for the appearance of a gap in metallic nanoribbons ($N = 3p + 2$) and its enhancement for nanoribbons in semiconductor states ($N = 3p$, $N = 3p + 1$). In a recent work [436], Rozhkov *et al*. noted that for the metallic state the gap can be closed in nanoribbons of finite size through substitution of the radicals passivating the armchair edges.

The influence of edge passivation on the gap has already been briefly discussed (Figure 84) for armchair ribbons. There are different ways of passivating the carbon atoms at the edges. The passivation by single hydrogen gives sp^2 hybridization at the edges, while passivation by two hydrogens leads to sp^3 hybridization. The variation of the percentage of the sp^3-like bonds has been found to significantly change the electronic properties of the armchair nanoribbon [428]. An increase in the proportion of sp^3-like bonds leads to an interplay between the metallic and semiconductor states. Thus the metallic state of the armchair ribbon of width $N = 8$ becomes a semiconductor state for sp^3 proportion larger than 20%. The semiconductor state $N = 9$ is found to be metallic if sp^3 percentage is $\sim$35%, while the semiconductor state $N = 10$ is switched to the metallic state when the proportion of sp^3-like bonds is $>60\%$. The transition occurs as a result of band reorganization, i.e. the shift of the subbands relative to each other along the energy scale. The electronic properties of armchair nanoribbons are also found to affect the formation energy of the armchair edges [403], a conclusion based on common oscillatory behavior of the formation energy and band gap versus the width, N, of armchair ribbons.

Zigzag nanoribbons have been found to possess a direct band gap which also is suppressed with increasing structure size [419,424]. However, the nature of the gap is different from that of armchair nanoribbons (for details, see Section 7.4). The HOMO and LUMO orbitals of the zigzag nanoribbon are formed by the edge states localized at the zigzag edges. The ground state of the zigzag nanoribbon is the FM-A state, characterized by ferromagnetic ordering of the spins of the localized states along each zigzag edge but their antiparallel orientation between the edges. The FM-A state has broken sublattice symmetry, which coupled with the destructive interference between the spin-up and spin-down tails of the localized states at the opposite zigzag edges leads to opening of a gap Δ_z^0 [414]. This gap decreases with increasing width w_z of zigzag ribbons (Figure 87) [414,419,424] due to the vanishing of the confinement effect. The Δ_z^1 band of the edge states close to the zone boundary is found to be highly confined, have dominant edge-state character and is insensitive to the width w_z. Therefore, the energy gap Δ_z^1 at the Brillouin zone is virtually independent of the width when $w_z > 12\,\text{Å}$ [419,424].

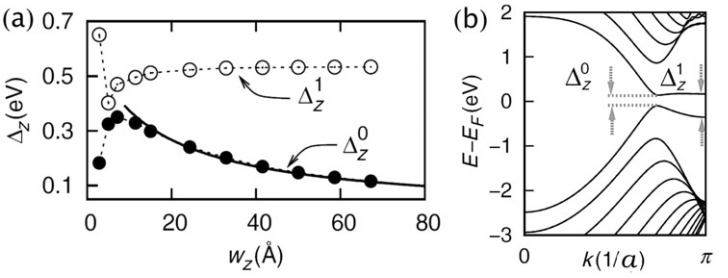

Figure 87. The dependence of the size of the direct band gap Δ_z^0 and energy splitting Δ_z^1 at $ka=\pi$ (a is the unit cell size) on the width w_z of the zigzag nanoribbon (Reprinted figure with permission from Y.-W. Son *et al.*, Physical Review Letters, 97, 216803, 2006 [419]. Copyright © (2006) by the American Chemical Society.).

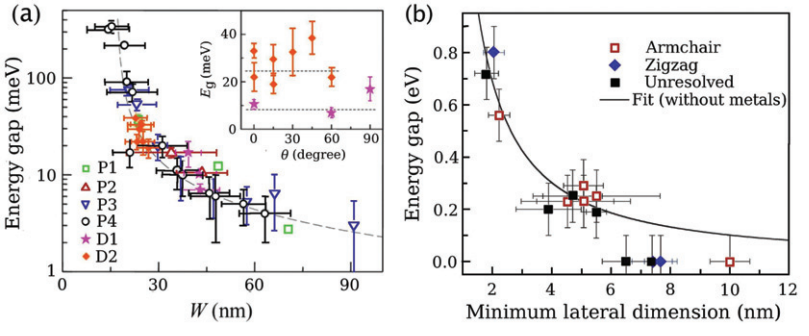

Figure 88. (a) The band gap size (E_g) as a function of nanoribbon width for six devices: four (P1–P4) of the parallel type, which contain many parallel ribbons of varying width, and two (D1,D2) devices having ribbons of uniform width and varying orientations described through the relative angle θ (Reprinted figure with permission from M.Y. Han *et al.*, Physical Review Letters, 98, 206805, 2007 [437]. Copyright © (2007) by the American Physical Society.). (b) The band gap variation (E_g) as function of QDs size for the zigzag and armchair systems (Reprinted figure with permission from K.A. Ritter *et al.*, Nature Materials, 8, p. 235, 2009 [441]. Copyright © (2009) Nature Publishing Group.).

Opening of a band gap in graphene induced by the confinement effect has been confirmed experimentally [29,437–440]. The experiment [437] was carried out for graphene nanoribbons fabricated from single sheets of graphene and contacted with the Cr/Au metal electrodes. Two types of devices were designed: one contained many parallel ribbons of varying width (P1–P4) while the second of uniform width and varying orientation described by an angle θ (D1–D2). The size of the band gap of these devices was found to decrease with increasing nanoribbon width (Figure 88(a)). The band gap was estimated through the dependence of the differential conductance on the gate and bias voltage in the nonlinear response regime. The band gap size was estimated from increasing conductance near the Dirac point with increasing nanoribbon width. Fitting the data gives the dependence of the conductance G on the width w as $G=\sigma(w-w_0)/L$, where σ is the sheet conductivity, $(w-w_0)$ is the active width and L=2 μm is the uniform length. A fit of the experimental data shows the following dependence of the band gap size on the nanoribbon

width: $E_g = \alpha/(w - w^*)$, where $\alpha = 0.2\,\text{eV}\cdot\text{nm}$ and $w^* = 16\,\text{nm}$. The conductance of the nanoribbon is found to be suppressed not only by reduction of the nanoribbon width, but also with a decrease in the temperature T. Similar measurements of the size of the band gap in graphene dots was reported in [441] by using scanning tunnelling spectroscopy. The graphene dots were labelled as armchair or zigzag systems by the highest fraction of the edge type presented. The data are shown in Figure 88(b). The confinement effect was found to be present in all the samples, but the zigzag systems were transformed into the metallic state at a smaller lateral dimension than that of the armchair systems. Therefore, the observed results have confirmed the influence of the crystallographic orientation of the edges in nanoscale graphene on its electronic properties and shown the metallic-like behavior of the zigzag nanoribbons.

In summary, for armchair nanoribbons a gap is found to open due to the crucial role of the edge effects which rearrange the subbands in the conduction and valence bands with varying size of nanoribbons. For zigzag nanoribbons, the broken sublattice symmetry resulting from antiferromagnetic spin ordering of the localized states at the zigzag edges also opens a gap. In addition, for both types of graphene nanoribbons, the quantum confinement is found to increase the gap, but an increase of the size of nanoribbons leads to vanishing of the gap.

7.6. *Graphene nanoribbons in an electric field*

Graphene is a unique material, where the spin distribution at the zigzag edges creates several metastable states energetically close to each other. The antiferromagnetic state of zigzag nanoribbons for which spins align along the zigzag edges but have opposite orientations between the two opposite zigzag edges, is energetically favorable in comparison to the nonmagnetic state or the ferromagnetic state with the same spin orientation between the zigzag edges [412,414]. Opposite zigzag edges belong to different sublattices, and therefore, in the antiferromagnetic state the spin-up state (α-spin state) is completely localized on the A sublattice, while the spin-down state (β-spin state) is localized on the B sublattice. Moreover, because of the strong localization of the electron density at the zigzag edges, the α-and β-spin states localized on the opposite zigzag edges are spatially separated. An electric field E_{ext} applied along the armchair edges shifts the energy of the states localized on one zigzag edge downwards and the opposite edge upward, thereby modifying the band gap for different spin states. Therefore, the applied electric field shifts the bands in such a way that if the occupied and unoccupied bands for one spin state move closer in energy, the bands for another spin state will move apart [442]. Modification of the band gap in an applied transverse electric field is presented in Figure 89. For zero electric field (see the left panel in Figure 89), the α-and β-spin states are degenerate in all bands, so the spin degeneracy is not lifted. The applied electric field strongly lifts the bands corresponding to states localized on the opposite zigzag edges apart, thereby increasing the band gap for the α-spin state and decreasing for the β-spin state. Therefore, for a certain electric field that is large enough to close the gap of the β-spin state, a half-metallic behavior is achieved. The critical electric field required to close the gap for the β-spin state decreases as the nanoribbon width increases, as the

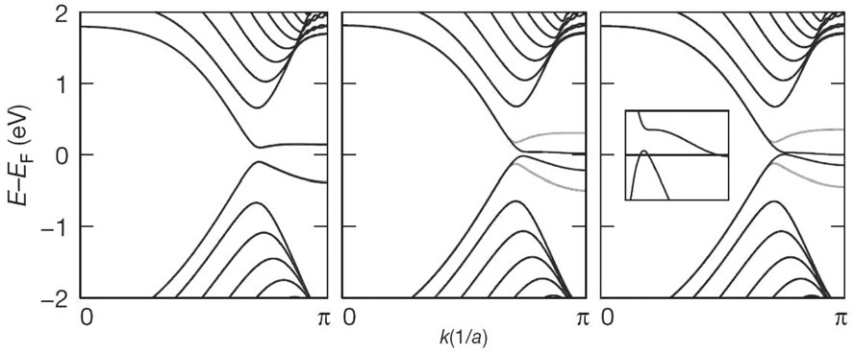

Figure 89. The influence of the transverse electric field on the band structure of zigzag graphene nanoribbons. Left panel: no electric field ($E_{ext} = 0\,V/Å$), middle panel: $E_{ext} = 0.05\,V/Å$ and the right panel: $E_{ext} = 0.1\,V/Å$. The gray color denotes the α-spin state, while the black one – β-spin state. Inset: band structure in the range of $E - E_F < 50\,meV$ and $0.7\pi \leq ka \leq \pi$, where the horizontal line is E_F (Reprinted figure with permission from Y.-W. Son *et al.*, Nature, 444, p. 347, 2006 [442]. Copyright © with permission from Nature Publishing Group.).

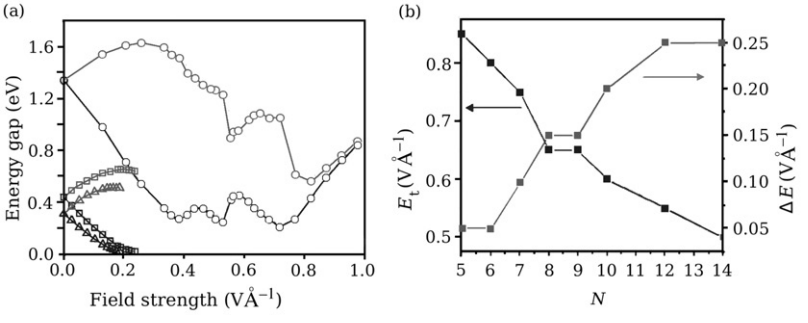

Figure 90. (a) Band gaps for the α- spin state (grey line) and the β-spin state (black line) as a function of the electric field calculated within the DFT methods using three different exchange-correlation functionals: LDA (triangles), BLYP (squares) and B3LYP (circles) (Reprinted figure with permission from E. Rudberg *et al.*, Nano Letters, 7, 2211, 2007 [446]. Copyright © (2007) by the American Chemical Society.). (b) The critical electric field E_t required to obtain the half-metallicity and the range of the electric field strength (from E_t to $E_t + \delta E$) to preserve the half-metallicity as a function of the nanoribbon size (n is the number of the carbon cells along the zigzag edge). The simulation is performed with the B3LYP functional (Reprinted with permission from E.-J. Kan *et al.*, Applied Physics Letters, 91, 243116, 2007 [447]. Copyright © (2007) American Institute of Physics.).

potential difference between two opposite zigzag edges is proportional to the distance between the zigzag edges. For nanoribbons with oxidized zigzag edges, the critical electric field varies with the choice of oxidation scheme [443]. Moreover, the oxidation stabilizes the state with antiferromagnetically ordered spins between the zigzag edges. The possibility to control the gap through breaking of the inversion symmetry by the potential from an external superlattice (e.g. by applying a gate voltage) was also discussed in [444,445]. The band gap size is found to be affected by the strength of the external potential and the lattice constant of the superlattice [444].

Interestingly, the size of the gap estimated by the DFT methods was found to depend on the choice of the exchange-correlation functional [446]. For the B3LYP functional the absence of the half-metallic regime in zigzag graphene nanoribbons was reported even at high electric fields. Results show the closing of the band gap for the α- and β-spin states, as the transverse electric field is applied are presented in Figure 90(a) for three different exchange-correlation functionals: B3LYP, LDA and BLYP. The data obtained within the hybrid B3LYP functional suggest that the condition when the band gap for the β-spin state vanishes cannot be reached. First of all, at zero electric field the band gaps for the α- and β-spin states are much larger than that obtained within the LDA and BLYP functionals, thereby raising the value of the critical electric field required to close the gap for the β-spin state. Moreover, at a high electric field (0.8 V/Å) the band gap of the β-spin state, which is not suppressed to zero, starts to grow again. The band gap for the α-spin state also behaves differently at high electric fields than that obtained with the LDA and BLYP functionals. Hence, at a field of 0.3 V/Å, the band gap starts to decrease and for fields higher than 0.8 V/Å, the gap for both spin states has the same size. A study of the influence of the applied electric field on the spin-density distribution has shown that in the middle of the ribbon the spin-density is reduced significantly by the field in comparison to that at the edges.

However, several other theoretical works reported that the non-local exchange correlation should not remove the half-metallicity in zigzag graphene nanoribbons [447,448]. Using a hybrid B3LYP functional, Kan *et al*. [447], found a spin gap asymmetry caused by the applied electric field, where the β-spin state is gapless. The magnitude of the critical electric field required to transfer the system into a half-metallic state was however larger (about 0.7 V Å^{-1}) than that obtained in [442] within the local-density functional approximation (LDA), which is known to underestimate the size of the band gap. The magnitude of the critical electric field E_t decreases with increasing nanoribbon size (Figure 90b). However, in a strong electric field the half-metallicity is found to be destroyed due to the transition to a spin-unpolarized state. Similar results suggesting that at high electric field the system is spin-unpolarized were also reported in [443]. The non-local exchange correlation term (B3LYP functional) was also shown to have negligible impact on the size of the band gap in an electric field [411], but the critical electric field required to achieve half-metallicity was of similar magnitude for different exchange-correlation functionals (about 0.2 V Å^{-1}).

Simulations of the zigzag nanoribbon in an electric field reported in [449] with the π-orbital Hubbard model SCF theory, however, revealed that the gate-induced charge carriers alter the charge distribution, spin configuration and total net spin polarization. For graphene in its antiferromagnetic state, when the localized states of opposite spin are located on the opposite zigzag edges, the gate-induced charge carriers break the charge distribution symmetry around the ribbon center. This leads to coupling of the charge density and spin polarization. Therefore, if the non-colinear regime is allowed within the Hubbard model, the non-colinear spin solution becomes energetically favorable, where spins localized on opposite edges are no longer antiparallel.

For the armchair nanoribbons, the influence of the geometry of nanoribbons on the suppression of the band gap by an electric field and the transition from semiconductor to metallic behavior were investigated within the Peierls approximation [451]. It was found that the magnitude of the critical electric field required to

close the band gap for the β-spin state can fluctuate in the range of 0.06–0.2 V Å^{-1} depending on the geometry of the nanoribbon. In another investigation [452], the transverse electric field applied across armchair nanoribbons was found to dramatically change the electron bands and affect the longitudinal electronic dispersion. Thus the Fermi velocity in metallic nanoribbons is found to be reduced by the field and this leads to an increase in the density of states at the band center. Moreover, the Fermi velocity and the effective mass were found to change sign in an electric field, while the band gap was suppressed by the external field resulting in extra plateaus in the conductance characteristics. The influence of the electric field and the size of graphene on the band gap and the effective mass was also considered in [427]. The magnitude of the effective mass grows with decreasing ribbon width, whereas the sign of the effective mass is reversed in the electric field, similar to the data in [452].

In summary, the external electric field applied to zigzag graphene nanoribbons opens the possibility to induce half-metallicity in the ribbons which has enormous potentials for application in spin-related electronic devices [48,450,453–464].

7.7. *Nanoscale graphene*

The band gap of nanoscale graphene with edges of arbitrary shape is found to vary as a function of the edge size and shape [361,420,433,435,465–469]. For graphene nanodots, the band gap deviation induced by the increasing width of the armchair edges was observed [423,466], and was similar to that of graphene nanoribbons. The amplitude of the energy gap oscillation with the length of the edges has been found to be smaller than that for the infinite size ribbons [423,466], while the periodicity of the oscillation was larger, i.e. the number of points between the maxima and minima was near 3, instead of 1 for the nanoribbon. For nanoscale graphene of rectangular shape, the deviation of the band gap with changing width was found to depend on the chirality angle ϕ [420,431]. The maximum amplitude of the deviation was achieved for $\phi = 0^\circ$, and this amplitude decreases with increasing ϕ [420]. For $\phi = 23.4^\circ$ the band gap is almost zero and independent of the nanoribbon width.

For nanoscale graphene flakes of arbitrary shape, the edges are still characterized by the stronger magnetic moment than the inner sites [470]. However, the applied magnetic field changes the localization of spin density at the edges [361]. In a magnetic field the electron density localized at the edges for the HOMO and LUMO orbitals is shifted closer to the center of graphene dot. Hence for the graphene dot, just as for the nanoribbon, the spin orientation of the localized states at the zigzag edges are associated with the sublattice site. If the zigzag edges belong to two different sublattices then, according to Lieb's theorem [471], the spin-polarized states at different edges exhibit opposite spin orientation [466,469,470,472]. For graphene flakes with mixed edges, it is enough for the defect-free segment of the zigzag edge to be greater than three or four repeat units to have a significant amount of magnetization [470]. The average edge magnetization along all the edges grows with decreasing proportion of the armchair edges and increasing proportion of zigzag edges [470]. Therefore, an obvious way to increase the magnetization of graphene

Figure 91. The structures of the nanoscale graphene characterized by the non-zero total spin S. The closed and open circles denote the A and B sublattices, respectively (Reprinted with permission from O.V. Yazyev *et al.*, Nano Letters, 8, 766, 2008 [472]. Copyright © (2008) by the American Chemical Society.).

would be to design it with high density of zigzag edges [472–474]. The same rule would apply for structures with mixed edges: the spin-polarized states localized on the border carbon atoms at the zigzag edges will exhibit opposite spin orientation if the carbon atoms belong to different sublattices. Therefore, if graphene has the same amount of zigzag edges in A and B sublattices, the net spin density is zero. Non-zero spin density of nanoscale graphene with high density of zigzag edges can be achieved by increasing the number of zigzag edges belonging to one sublattice (Figure 91) [472]. For triangular structures, sublattice A dominates at the edges over the whole structure resulting in non-zero net spin. Such structures with high spin states can open a new avenue in nanoscale spintronics.

The possibility to create multiple quantum well structures using repeated junctions of armchair graphene nanoribbons was considered in [433,468]. By altering the width and shape of the quantum well, it was shown that the fixed spin state can be confined in the well, and this is a promising direction for engineering the spintronics devices. The transmission coefficient though such devices shows resonant peaks which can be assigned to electronic states localized in the quantum well. Accurate understanding of the dependence of the electronic and magnetic properties of nanoscale graphene on its edge shape is crucial for developing electronic devices based on this system [475–482].

7.8. *Bilayer graphene nanoribbons and the effects of edges*

The effects of the arrangements of atoms at the edges of finite-sized graphene flakes are well known in the case of the monolayer [391]. Tight-binding models predict significantly different band gaps depending on the number of atoms across the width of the ribbon (modulo 3), and the magnetic properties of zigzag and armchair edges are also significantly different. This complexity carries over to the bilayer case, and while there is currently no clear picture of the properties of bilayer ribbons and their edges, we shall present the current state of knowledge of this topic.

Recently, it was reported [483] that chemical methods could manufacture graphene nanoribbons with widths ranging from 50 nm to <10 nm with possibly well-defined zigzag or armchair edges. Exfoliated graphene was placed in solution, deposited on a substrate, and fashioned into field effect transistors. Figure 1 in [483] shows several nanoribbons which the authors claim are two layers thick – i.e. they are bilayer nanoribbons. Figure 92 shows the current–voltage characteristics for two nanoribbons, and the authors claim that all their ribbons with width $w < 10$ nm

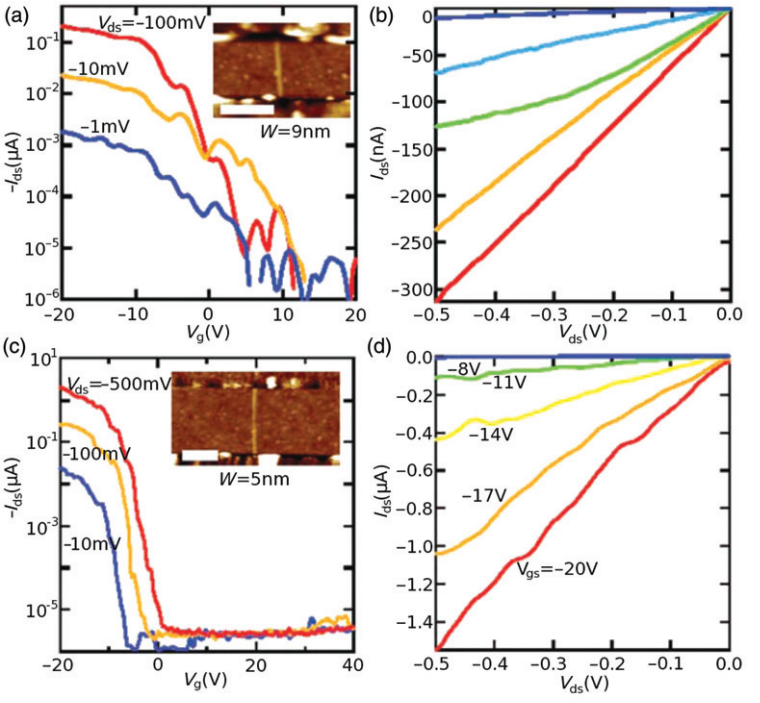

Figure 92. Room-temperature graphene nanoribbon FETs with high on–off ratios. (a) Transfer characteristics (current versus gate voltage) for a $w \approx 9$ nm (thickness ~1.5 nm, ~two layers) and channel length $L \sim 130$ nm GNR with Pd contacts and Si backgate. (Inset) AFM image of this device. Scale bar is 100 nm. (b) Current–voltage curves recorded under various gate voltages for the device in (a). (c) Transfer characteristics for a $w \approx 5$ nm (thickness ~1.5 nm, ~two layers) and channel length $L \sim 210$ nm GNR with Pd contacts. (Inset) The AFM image of this device. Scale bar is 100 nm. (d) Current–voltage characteristics recorded under various gate voltages for the device in (c) (Reprinted figure with permission from X. Li *et al.*, Science, 319, p. 1229, 2008 [483]. Copyright © (2008) The American Association for the Advancement of Science.).

had an on-off ratio of better than 10^5. The band gaps extracted from these transport data fitted the empirical form of $E_g(\text{eV}) = \frac{0.8}{W(\text{nm})}$. However, these band gaps fall between the theoretically predicted values for ribbons with zigzag and armchair edges, and the precise structure of the edges of the flakes is not known.

From a theoretical point of view, the alignment of atoms at the edges of the ribbon are a key factor in the determination of the ribbon's electrical and magnetic properties. As well as the zigzag and armchair terminations (which carry over their definition from the monolayer), there are two alignments of atoms in the layers which must be considered. They are shown in Figure 93 where the commonly-used nomenclature of α and β alignments has been adopted. The distinguishing feature of the two alignments is where the dimer bonds are positioned relative to the edge. In the β alignment they constitute one part of the last row of atoms, while in the α alignment they do not. Both tight-binding and DFT methods have been used to address the electronic and magnetic properties of finite-sized bilayer graphene. There are some difficulties in the approach of DFT methods, since traditional formulations

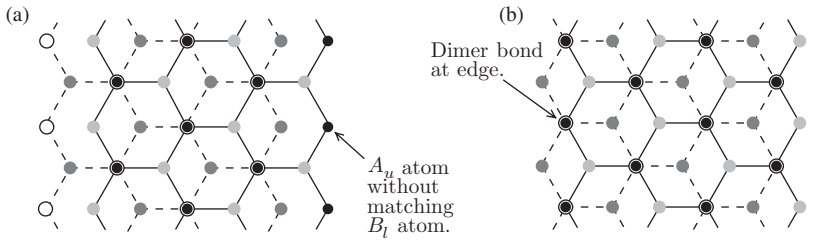

Figure 93. The two orientations of the bilayer ribbon: The α alignment (left), the β alignment (right). The essential difference is that the β alignment has dimer bonds at the edge, while the α alignment does not.

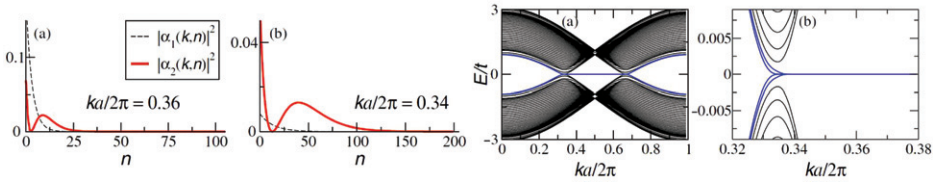

Figure 94. (a) Charge density for bilayer edge states at $ka/2\pi = 0.36$ and (b) $ka/2\pi = 0.34$. (c) Energy spectrum for a bilayer ribbon with zigzag edges: $N = 400$, $\gamma_1 = 0.2\gamma$. (d) Zoom of (c) (Reprinted figure with permission from E.V. Castro *et al.*, Physical Review Letters, 100, 026802, 2008 [486]. Copyright © (2008) by the American Physical Society.).

do not account well for the van der Waals interactions between the layers. Lima [484] accounted for this by adding a nonlocal potential in the Kohn–Sham equations, but otherwise there is some doubt over the accuracy of DFT calculations. For example, Sahu *et al.* [485] find that LDA and GGA make different predictions on the magnetic properties of the lowest energy state in zigzag ribbons in the α alignment.

We shall present a summary of the effects of the finite system size on the band structure, and the possible modes of magnetic ordering at the edges. Most work has so far been done on the β-aligned zigzag edged system. Castro [486] has shown the existence of two classes of edge state within the tight-binding model: those that are localized in one layer only, and those that have wave function amplitude on both layers. In a semi-infinite system, the edge states exist in the momentum range $2\pi/3 < ka < 4\pi/3$, as in the monolayer case. Figure 94(a) and (b) show two examples of charge density for the edge of a semi-infinite bilayer, i.e. those derived by solving the Schrödinger equation with zero eigenvalue. The penetration depth is of the order of a few tens of lattice sites, $\lambda = -1/\ln|-2\cos(ka/2)|$. The energy spectrum of the nanoribbon is shown in Figure 94(c) and (d) for a ribbon of width $N = 400$, and $\gamma_1 = 0.2t$. The four-fold degeneracy of the edge states (one per class per edge) is clear from (d), and the overall sinusoidal dependence of the energy bands is evident in (c). The lifting of the degeneracy is due to the overlap of the wave functions from the two edges, which occurs where the penetration depth is highest, i.e. at $ka = \pm 2\pi/3$. When an inter layer bias is applied, the degeneracy of the flat bands is lifted. The two 'monolayer' edge states retain their flat dispersion, but split into the conduction and valence bands. The two 'bilayer' edge states gain a dispersion, and cross at $\epsilon = 0$ near the Dirac points. This crossing is justified by treating the inter

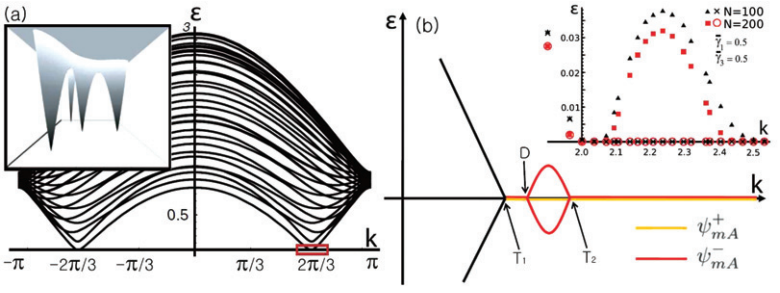

Figure 95. (Colour online) (a) Projected band structure of the 2D graphite bilayer along the direction of the zigzag axis. The boxed region near the Dirac point is magnified in the inset, which shows the trigonal warping. D is the Dirac point at $k = 2\pi/3$ and three L points are the Fermi points of three nearby pockets. (b) A schematic diagram of the zero-energy edge states of a semi-infinite Z-BGNR near the Dirac point within the red box in (a). At $\varepsilon = 0$, the two eigenstates are drawn with different colors. Red (dark gray) for ψ_- and yellow (pale gray) for ψ_+. D is the Dirac point while T_1, T_2 and the two warped bands reflect the effect of trigonal warping of the graphite bilayer. The inset shows the energy dispersion curve obtained by a numerical method for Z-BGNRs with finite widths $N = 100$, 200 (Reprinted figure with permission from J.-W. Rhim *et al.*, Journal of Physics: Condensed Matter, 20, p. 365202, 2008 [487]. Copyright © (2008) IOP Publishing Ltd.).

layer potential as a perturbation to the tight-binding model. Yao *et al.* [445] find the same picture, but emphasize that the dispersive edge states have valley-dependent velocity near the Dirac points, and that the behavior of edge states is determined by the valley-dependent topological charges in the bulk.

Rhim *et al.* [487] introduced the trigonal warping to the analysis of β-aligned zigzag bilayers (Figure 95). The effect of the Lifshitz transition, and the complex structure of the Fermi surface at low-energy was taken into account, and it was found that the nature of the edge states reflects this complexity. In particular, a forbidden region is introduced for one of the edge states (between D and T_2 in Figure 95(b)), a feature unique to zigzag bilayer nanoribbons. The locations of the position of the pockets in the Fermi surface agreed exactly with those calculated for the bulk system [139]. Inclusion of the other next-nearest neighbor inter-layer hopping parameter γ_4 lifted the electron–hole degeneracy and moves the Fermi points back toward the Dirac point. Also, within the half-filled Hubbard model with the Hartree–Fock approximation, and for realistic values of the Coulomb interaction, ferromagnetic alignment of inter-layer spins is preferred along each edge.

Lima *et al.* [484] reported on the electronic, magnetic and structural properties of both α- and β-aligned ribbons within the DFT framework. They assumed hydrogen passivation, and established that the alignment of the edges is a significant factor for the band structure (see Figure 96(a) and (b)). In the β alignment, the state with antiferromagnetic order both along and between the edges was the lowest energy state, although by an amount less than $k_B T$. The α-aligned ground state was qualitatively different because there is a strong attractive interaction between the edge atoms of the two layers which produced a geometrical distortion of the lattice. This allowed a gapped, non-magnetic ground state to form, in contrast to other analysis. In fact, the α-alignment yielded a lower overall ground state energy than the β-alignment. The inter-edge interaction can be split into a part which depends

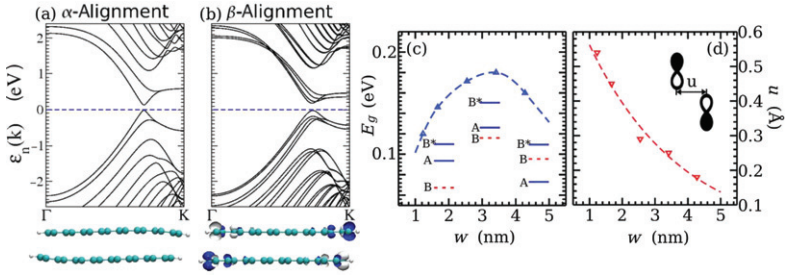

Figure 96. (a) Ground state of fully relaxed bilayer ZGNRs generated by stacking two (7,0) monolayer ZGNRs. Below each band structure the geometry and local magnetization are presented. (i) α-alignment. This state is nonmagnetic and presents a geometric distortion near the edge. (ii) β-alignment. This state shows an antiferromagnetic in-layer and antiferromagnetic inter-layer magnetic order. (b) Dependencies of the (i) energy gap and (ii) the lateral deviation $u = d_{CC} - d$ of the width w (Reprinted figure with permission from M.P. Lima *et al.*, Physical Review B, 79, 153401, 2009 [484]. Copyright © (2009) by the American Physical Society.).

on the ribbon width (and is therefore due to the edge), and a part which is constant (and therefore due to the bulk). Binding energies per unit length fit $E_b(w) = a + bw$, with $b = -2.0\,\text{eV}$ per atom for both alignments. However, $a = -0.26\text{eV}\,\text{nm}^{-1}$ for the α alignment, and $a = +0.13\,\text{eV}\,\text{nm}^{-1}$ for the β-alignment, explaining the overall energy reduction in the former case. The gap which opened in the α-aligned case was dependent on the ribbon width, as shown in Figure 96(c). The reason for the peak is the reordering of the electron localization between different sublattices. For narrow ribbons, the top of the valence band is located on the A sublattice, whereas for larger ribbons it is on the B sublattice, as with the Fermi level orbitals in the infinite system.

Sahu *et al.* [485] considered all four types of bilayer ribbon, and showed that the band gaps in armchair ribbons are rather smaller than those in zigzag ribbons using both a tight-binding theory and DFT. They linked the occurrence of edge magnetism to the existence of flat bands, and derived a critical band gap above which applying an interlayer bias will increase the gap, and below which will decrease it. They commented on the sensitivity of the band gap and magnetic ordering to the details of the exchange-correlation potential taken in their DFT.

Finally Lam *et al.* [488] showed DFT calculations of the band structure of α-aligned armchair ribbons as a function of the ribbon width, interlayer spacing, and concentration of dopants along the ribbon edges (Figure 97). They found that the optimal interlayer distance is slightly smaller for bilayer ribbons that for the bulk bilayer system. As in the monolayer case, they find a dependence of the band gap on the ribbon width which is periodic in the number of atoms, as shown in Figure 97(a), although the gaps in the bilayer ribbons are systematically smaller than those in the monolayer ribbons. When the optimum interlayer distance is taken, ribbons with $N = 3p+2$ (where p is an integer) are found to have metallic behavior, whereas the cases $N = 3p$ and $N = 3p + 1$ are semiconducting. The authors suggest that this metallic behavior and the consistently smaller gaps are due to the electron–electron interactions between layers at the edges which diminishes the edge effects and helps to restore the bulk (metallic) behavior. If the edges are doped (either with n-type or p-type dopants, e.g. nitrogen or boron, respectively), the Fermi level is shifted as

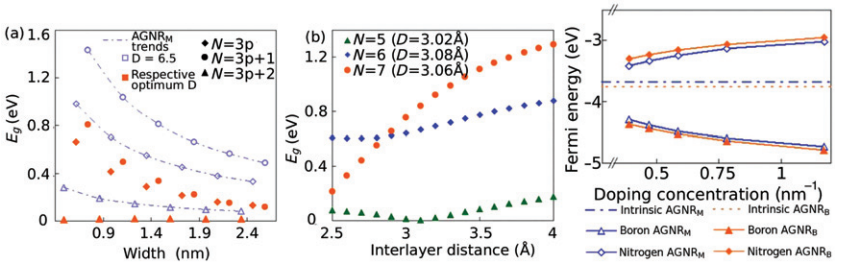

Figure 97. (Colour online) (a) Energy gap as a function of the width of the bilayer AGNR for interlayer distance 0.65nm (hollow points) and the respective optimum inter layer distance D (solid points). Diamond, circle and square points represent the three different families of $N=3p$, $3p+1$, $3p+2$, respectively. Unlike the monolayer ribbons, the family of $N=3p+2$ shows almost zero band gap for any width. The dot-dash lines show the three trends in the monolayer AGNR which coincide with the bilayer trends when the interlayer spacing is large. (b) Dependence of the band gap on D for the bilayer for $N=5,6,7$. The electronic structure depends strongly on its interlayer distance. (c) Fermi level vis-a-vis different boron (triangle) and nitrogen (diamond) doping concentrations for monolayer (blue) and bilayer (red) 7-AGNRs. The dot-dash and dotted lines are the original Fermi level of the undoped mono- and bilayer ribbons, respectively. As doping concentration increases, the band gap of all four cases also decreases (Reprinted with permission from K.-T. Lam *et al.*, Applied Physics Letters, 92, 223106, 2008 [488]. Copyright © (2008) American Institute of Physics.).

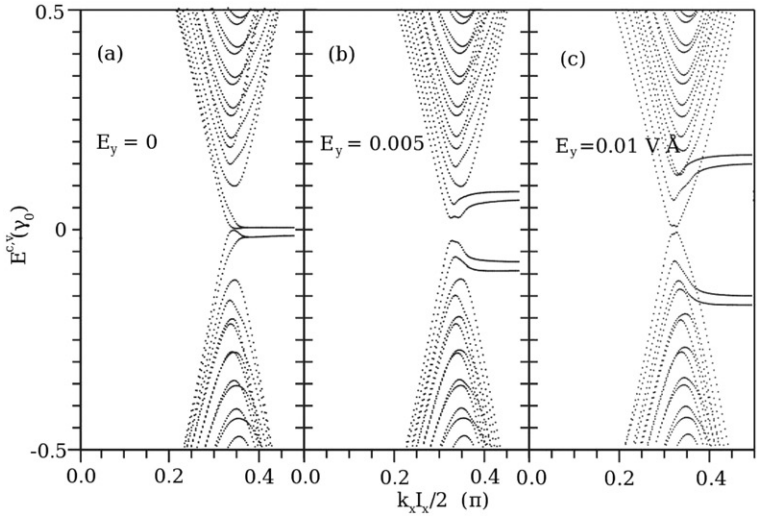

Figure 98. The low-energy electronic structure of *AB*-stacked zigzag GNRs with 40 dimer lines in the y direction, and infinite extent in the x direction. (a) Zero parallel field; (b) parallel field $E_y=0.005$ V Å^{-1}; (c) $E_y=0.01$ V Å^{-1} (Reprinted with permission from Y.C. Huang *et al.*, Journal of Applied Physics, 104, 103714, 2008 [489]. Copyright © (2008) American Institute of Physics.).

shown in Figure 97(c). The effect of dopants is marginally smaller on the bilayer ribbons than on the equivalent monolayers.

Huang *et al.* [489] showed using exact diagonalization of an explicit tight binding model, that the application of an electric field across the width of the nanoribbon

(i.e. parallel to the plane of the ribbon) will also cause a gap to open in the low-energy spectrum. In fact, this field can also cause subband crossings and anticrossings, alter band features and lift the degeneracy of the flat bands, as shown in Figure 98. The application of successively stronger fields moves the flat bands away from the charge-neutrality point, lifts the degeneracy in both the conduction and valence bands, and distorts their shape so that they are no longer flat. The size of the band gap in zigzag nanoribbons is non-monotonic in the strength of the parallel field, E_y, since the effect of application of stronger field is two-fold: it moves the partially flat bands away from each other, but the lowest higher energy (nearly parabolic) bands come down in energy. The two types of band cross at approximated $E_y = 0.006\,\mathrm{V\,\AA^{-1}}$, and the largest gap is $E_g \approx 0.08\gamma_0 \approx 0.24\,\mathrm{eV}$. The gaps are smaller in armchair ribbons, and there are some values of E_y for which the gap closes completely. The authors also discussed the density of states for zigzag and armchair ribbons.

The properties of bilayer ribbons placed in magnetic fields were investigated by Nemec *et al*. [191], who computed the Hofstadtter butterflies for this material, and Huang *et al*. [197], who not only examined the LLs and magneto-optical absorption of wide bilayer nanoribbons and found many of the same features as exhibited in the bulk system, but also included the second-order interlayer couplings. The existence of bilayer-type edge states in few-layer graphene stacks has also been discussed [490].

8. Manipulation of the band gap and magnetic properties of graphene

Despite all the fascinating properties of graphene, such as relativistic massless dispersion and high mobility, the gapless band structure makes its difficult to find a direct application for graphene in field-effect transistors. However, an easy way to avoid a gapless band structure is to decrease its size to the nanoscale, so that the confinement effect induces a gap. The size of the gap is found to fluctuate depending on the geometry of the edge of graphene, which makes it somewhat difficult to manufacture graphene structures with the desired electronic properties because of limitations imposed by current fabrication techniques. However, the problem of the formation of sharp graphene edges with ideal atomic structures [491] has been resolved by unzipping carbon nanotubes to graphene nanoribbons of controllable size [492,493]. This is a significant breakthrough in the fabrication of graphene. These techniques should enhance the interest in manipulation of the electronic properties of graphene nanoribbons by external sources, such as edge modification, adsorption of dopants and introduction of defects into the graphene lattice.

The gapless low-energy band structure is protected by the symmetry of the hexagonal lattice, so any local changes in the lattice or an imbalance of electrons of different spins can break the group or sublattice symmetries and induce a gap. An example of how the hexagonal symmetry [433,434,494,495] can be broken could be done by an external strain applied to the graphene lattice. A symmetrical strain distribution will keep the hexagonal symmetry unchanged and band structure will remain gapless [494]. An asymmetrical strain breaks the translation symmetry of the lattice which opens a gap at the charge-neutrality point, that can be used to tune the size of the gap [434,494]. Such a strain, depending on its strength and direction

is found to move the band crossing away from the K point [434]. This influence of uniaxial strain on the electronic properties of graphene has been observed experimentally [495,496]. A significant red shift of the 2D and G bands in the Raman spectra, which was attributed to the presence of a gap, has been obtained due to stretching in one direction of the substrate with graphene deposited on top. The G band splitting into two subbands as a result of symmetry breaking has indeed been observed [496]. Good reversibility and an upward shift of the Raman peaks when the strain is released was also indicated.

Practical application of the strain induced band gap would primarily be in developing strain sensors. The most useful route to manipulate the electronic properties of graphene would be inducing permanent changes in the graphene lattice, which can break the symmetry and open a gap. The breaking of sublattice symmetry, which can be done by unequal doping of graphene sublattices is one such possibility. Very intensive research is now being undertaken in this direction, such as interaction of the graphene layer with the substrate or adsorbates, the influence of defects and dislocations, doping and functionalizing of the graphene lattice or edges. All these possibilities are dealt with in the present section.

8.1. *Interaction of graphene with a substrate*

Experimental [35,140,497–501] and theoretical [383,502–510] studies of epitaxial graphene have shown that the charge exchange between graphene and the substrate directly influences the electronic properties of graphene. It is known that the interaction between two layers of graphene is weak, but for the first layer epitaxially grown on the substrate, the bonding to the substrate can induce structural changes in the graphene lattice. These changes may lead to the formation of a buffer layer, whose electronic properties are different from that of the isolated graphene sheets. This issue has opened a wide discussion in this subfield.

There are two main theoretical models proposed for the description of the interaction between the first graphene layer and the substrate. According to the first model, the graphene layer epitaxially grown on the Si-terminated (0001) or C-terminated $(000\bar{1})$ SiC substrates, forms strong covalent bonds with the substrate [502,503] (Figure 99). The strong bonding occurs because the binding energy between the layers is stronger than the elastic stress at the interfaces [503]. The two dangling

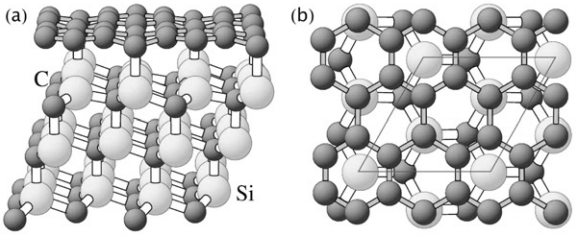

Figure 99. The buffer graphene layer on the SiC (0001) surface (Si-terminated) (a) side view and (b) top view (Reprinted figure with permission from A. Mattausch and O. Pankratov, Physical Review Letters, 99, 076802, 2007 [503]. Copyright © (2007) by the American Physical Society.).

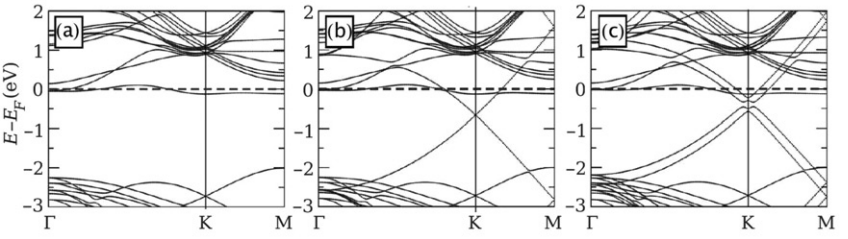

Figure 100. The band structure of epitaxial graphene on the SiC substrate with Si-terminated surface. (a) buffer layer of graphene on the surface, (b) single layer of graphene on the surface, (c) double layer of graphene on the surface (Reprinted figure with permission from F. Varchon *et al.*, Physical Review Letters, 99, 126805, 2007 [502]. Copyright © (2007) by the American Physical Society.).

states of the Si-terminated substrate form covalent bonds to the carbon atoms in graphene, while the third dangling bond is unsaturated, thereby generating half-filled metallic states close to the Fermi level. For the buffer layer on the C-terminated SiC substrate, there are two bands resulting from splitting of the interface state into single occupied and unoccupied states. The crossing of cone-shaped conduction and valence bands of the buffer layer is shifted deeper into the valence band for the Si-terminated case [502,503]. Therefore, the Fermi level of the first undeformed graphene layer on a Si-terminated substrate is located at 0.4 eV above the Dirac point [502], i.e. the graphene is *n*-doped, as was also reported in experimental work [504]. The new conduction band formed by the SiC substrate overlaps with the upper band of the buffer layer thereby making a wide energy gap, as presented in Figure 100(a). For the C-terminated substrate, the Fermi level location corresponds to the Dirac point and the first graphene layer remains undoped. The next layer for both types of substrates exhibits pure graphene properties because of the weak van der Waals interaction with the buffer layer. The electronic structure of this undeformed layer is similar to those for the isolated graphene sheets (Figure 100(b)). In particular, the dispersion of cone-shaped conduction and valence bands is restored. Systems containing two undeformed graphene layers, due to weak interaction between them, shows the properties of bilayer graphene (Figure 100(c)).

The second model assumes a different behavior of the buffer layer. According to the second model, the first graphene layer interacts weakly with the substrate. It was predicted that this model is appropriate for the C-terminated face of the SiC surface, which was experimentally seen to have weaker coupling between the graphene layer and SiC substrate [501] in comparison to the Si-terminated face. This C-terminated face of the SiC surface was later theoretically predicted to exclude formation of the buffer layer between graphene and the substrate [510]. Therefore, in the absence of a buffer layer, the first layer would possess a graphene-like band structure with the cone-shaped conduction and valence bands.

However, according to the experimental data obtained with angle-resolved photo-emission spectroscopy (ARPES), different results for the interaction of the epitaxially grown graphene with SiC substrate have been observed [35]. Formation of a buffer layer has been confirmed and its properties were found to be different from that of graphene, namely the σ bands remain similar to that of graphene, while the π

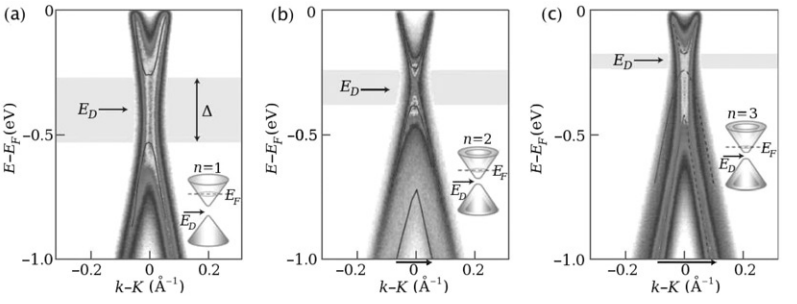

Figure 101. The intensity map obtained with ARPES for (a) single layer of graphene on a 6H-SiC substrate ($\Delta \sim 0.26$ eV), (b) double layer of graphene on a 4H-SiC substrate ($\Delta \sim 0.14$ eV), and (c) triple layer of graphene on a 6H-SiC substrate ($\Delta \sim 0.066$ eV). Here E_D is the energy of the Dirac point (Reprinted figure with permission from S.Y. Zhou *et al.*, Nature Materials, 6, p. 770, 2007 [35]. Copyright © (2007) Nature Publishing Group.).

bands were modified due to hybridization with the dangling bonds from the substrate. The unchanged σ bands indicate the presence of a honeycomb lattice in the buffer layer. The interaction of the buffer layer with the next layer was predicted to break the sublattice symmetry structurally and open a gap of $\Delta \sim 0.26$ eV [35]. It was observed for the buffer layer that only three Dirac cone replicas out of six were intense and formed a small hexagon around each corner of the Brillouin zone, thereby implying that the six-fold rotational symmetry of graphene was broken by only three-fold. Breaking of the symmetry was seen only near the Dirac points (E_D), whereas near the Fermi level the symmetry was preserved. The first undeformed graphene layer was also found to be *n*-type doped and E_D was shifted relative to E_F by ~ 0.4 eV. Increasing the number of layers resulted in a decrease of the band gap. Experimental data for single, double and triple layers of graphene are presented in Figure 101. For bilayer and trilayer graphene, occurrence of the gap was attributed to the breaking of the sublattice symmetry as a result of AB stacking between the graphene layers. Increasing the number of layers causes a shift of E_D towards E_F, so that the $E_D - E_F$ is ~ 0.3 eV for the double layer and ~ 0.2 eV for the triple layer. This shift has been attributed to the presence of an electric field formed by the accumulation of charges at the graphene surface, and its reduction with thickness was explained by an increase in distance between the surface layer and the interface. The size of the gap and shift of the Fermi level were found to be independent of the sample preparation and doping of the substrate. Epitaxial graphene thicker than five layers behaves like bulk graphite. Theoretical computations [509] have confirmed that for stacked graphene layers, if the A sublattice is stacked above the B sublattice, the band gap will decrease with increasing number of layers. However, it is expected that the appearance of AB stacking between the buffer and the first graphene layer would be dependent on the type of substrate. For example, according to the experimental data [498], growing graphene on the 4H-SiC sublattice does not provide AB stacked films. Instead, the two graphene sheets are rotated relative to each other, and this produces an electronic structure for multilayer graphene that is similar to an isolated graphene sheet.

There are other points of views relating to the cause of the opening of a band gap in graphene epitaxially grown on the SiC substrate [140,511]. The band gap observed

in the experiment [140] was attributed to the breaking of graphene symmetry by the built-in dipole field induced between the depleted SiC substrate and the charge accumulated on the surface of the graphene layer. However in [511], the presence of the Stone–Wales defects in the graphene layer was proposed to be responsible for breaking of the symmetry. There, the gap is found to decrease with increasing graphene thickness, which is in good agreement with experiments [35]. The influence of the Fermi level position on the sample preparation and doping of the substrate also was discussed [499,505]. An independence of the Fermi level position on the doping of the substrate and the substrate type were indicated in experiments performed with Raman spectroscopy [499]. Moreover, it was observed that graphene on an SiC substrate shows a blue shift in the position of the G-peak, which has not been observed for graphene transferred to a SiO_2 substrate. However, in theoretical works [505] it was claimed that for graphene on the GaAs substrate, the graphene layer can be doped by doping the GaAs substrate.

The importance of the interaction of graphene with the substrate and its impact on the electronic properties was also considered for other types of substrates. Graphene supported on the Si/SiO_2 substrate [497] was found to be doped. As-prepared graphene on the Si/SiO_2 substrate has shown to be *p*-doped, but after the samples are exposed in vacuum for 20 h at 200°C they evolve to be *n*-doped. It was proposed that the *p*-doping of the as-prepared samples is a result of its interaction with the gas dissolved in the environment, while the *n*-type behavior in the gas-free environment has been attributed to the intrinsic properties of graphene on an Si/SiO_2 substrate. The *n*-doping was explained to be a result of electron donation to graphene from the surface states of SiO_2, which are energetically located just below the conduction band edge of graphene. However, it was predicted theoretically that the electronic properties of graphene on an SiO_2 substrate can depend on the surface polarity, which is controlled by the substrate termination [506]. It was shown that the O-terminated SiO_2 surface provides a strong interaction between the carbon atoms of graphene and the oxygen atoms of the substrate, which can significantly modify the band structure of graphene by removing its cone-shaped bands. If the interaction of the oxygen atoms with one carbon sublattice is stronger than with the other, the appearance of a graphene-like band structure with broken sublattice symmetry and a small gap of 0.13 eV was predicted. Moreover, the strong interaction of the O-terminated substrate with graphene leads to *p*-doping of graphene. The Si-terminated SiO_2 surface possessing active dangling bonds has shown weak interaction with *n*-doped graphene. Opening of a gap has also been predicted theoretically in [508]. Thus, the oxygen passivated surface of the SiO_2 substrate was found to make covalent bonds to the graphene layer, significantly modifying the electronic properties of graphene by removing the cone-shaped bands (similar to that of graphene on a SiC substrate) and forming a gap. Hydrogen-passivation of the oxygen atoms on the SiO_2 substrate removes the covalent bonding between the substrate and the graphene layer and leads to a band structure comparable to that of the isolated graphene sheet. Moreover, the type of doping from the SiO_2 substrate in [500] was suggested to depend on the difference between the contact potentials of the graphene layer and the substrate because this difference defines the direction of the dipole orientation generated due to the charge exchange between graphene and the SiO_2 substrate.

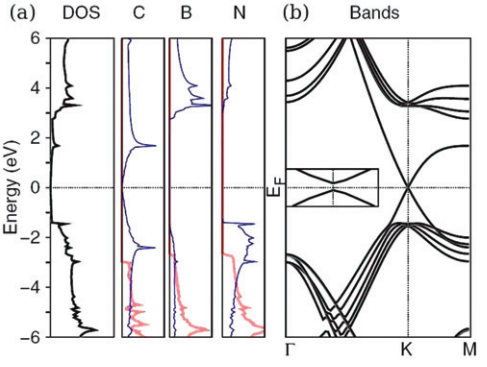

Figure 102. (a) Total density of states for a graphene layer on hexagonal boron nitride substrate with contribution from carbon, boron and nitrogen atoms projected on the *p* states in plane (thick gray line) and out of plane (narrow dark line). (b) Band structure of graphene along the Γ K and KM directions in reciprocal space with band gap of 53 meV, which is magnified in inset (Reprinted figure with permission from G. Giovannetti *et al.*, Physical Review B, 76, 073103, 2007 [383]. Copyright © (2007) by the American Physical Society.).

There are some theoretical predictions for the substrate induced gap in graphene on a boron nitride substrate [383,507]. For graphene on the N-terminated cubic boron-nitride [507], the equivalence between the A and B sublattices of graphene is broken which results in a gap. The effect occurs because the two sublattices are located at different places on the boron-nitride lattice, and therefore have different chemical environments. When the carbon atoms belonging to one sublattice are located on top of the nitrogen atoms, the charge exchange between the dangling bonds of the nitrogen and carbon atoms is significant in comparison to that between the carbon atoms of the other sublattice and the boron atoms. The obtained band gap was ~0.13 eV and the majority and minority spin bands were split. The electronic structure of graphene on a boron nitride substrate was also found to be affected by the termination of the substrate surface. Thus, for the B-terminated cubic boron-nitride the surface states on substrate are energetically located higher than the Fermi level of graphene, thereby having no effect on its properties. Similar results showing opening of a gap were obtained for graphene on a hexagonal boron nitride substrate [383], whose band structure is presented in Figure 102. The opening of a gap is attributed to the inequivalence of the carbon sites belonging to different sublattices due to their location: one carbon atom is placed on top of the boron atom, while the other in the center of the boron-nitride ring. The band structure of graphene on a boron-nitride substrate was found to be similar to that of the isolated graphene sheet, i.e. the appearance of the Dirac cones around the K points has been predicted. However, the dispersion around the Dirac points was quadratic (see inset in Figure 102b). The gap decreases with increasing distance between graphene and the substrate.

When graphene is placed on a metal substrate, the cone-shaped electronic structure of graphene is predicted to be preserved but the Fermi level is shifted relative the Dirac point [512,513]. It was found that the shift can be in either direction giving rise to either *n*-type or *p*-type doping. The shift of the Fermi level ΔE_F and difference of the workfunctions between the metal-graphene system and the

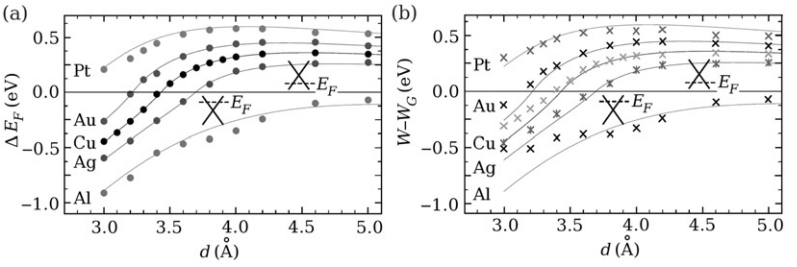

Figure 103. (a) Shift of the Fermi level position (ΔE_F) relative to the Dirac point with increasing distance between graphene and the metal substrate. (b) Estimated difference of the work function between the graphene-metal systems and a pure graphene sheet ($W - W_G$) as a function of the distance between graphene and the metal substrate. The dots and crosses are results obtained from DFT-LDA calculations and solid lines – from phenomenological model (Reprinted figure with permission from P.A. Khomyakov *et al.*, Physical Review B, 79, 195425, 2009 [513]. Copyright © (2009) by the American Physical Society.).

pure graphene sheet ($W - W_G$) as a function of the graphene-metal separation is presented in Figure 103. These results allowed the authors to predict that the charge distribution at the graphene-metal interface depends on both the electron transfer between the metal and graphene (that tends to bring the Fermi level of graphene and the metal to equilibrium), and on the metal-graphene chemical interactions. It was concluded that the shift of the Fermi level position is governed by the magnitude of the charge transfer between the metal and graphene. The switch from *p*- to *n*-type doping occurs as a result of the coincidence of the Fermi level and the Dirac point. The critical value of the metal work function $W(d) = W_G + \Delta_c(d)$ corresponds to this crossover point, where $\Delta_c(d)$ describes the short-range interactions resulting from the overlap of the metal and graphene work functions. Moreover, the presence of the metal-graphene interactions induces the asymmetry of the spin-up and spin-down bands in graphene. For graphene on a Cu(111) substrate [383], the influence of the substrate on the electronic properties was found to be rather weak. It was shown that the inequivalence of the carbon sites belonging to different sublattices is not essential for this substrate, thereby preserving the almost metallic behavior of graphene.

Therefore, we can conclude that the interaction of graphene with the substrate modifies the electronic properties of graphene. The nonequivalent charge exchange between the substrate or the buffer layer and the carbon atoms belonging to different sublattices of graphene, the built-in dipole field induced due to the charge accumulation in the system may break the symmetry of graphene, which results in the formation of a gap. For graphene on a metal substrate the main effect corresponds to doping of graphene as a result of charge exchange between the substrate and graphene.

8.2. *Doping of graphene through adsorption*

8.2.1. *Adsorption of non-metals on graphene: experimental results*

Most organic molecules interact rather weakly with the surface of pure graphene and because there is no covalent bonding to the surface, the interaction is mostly

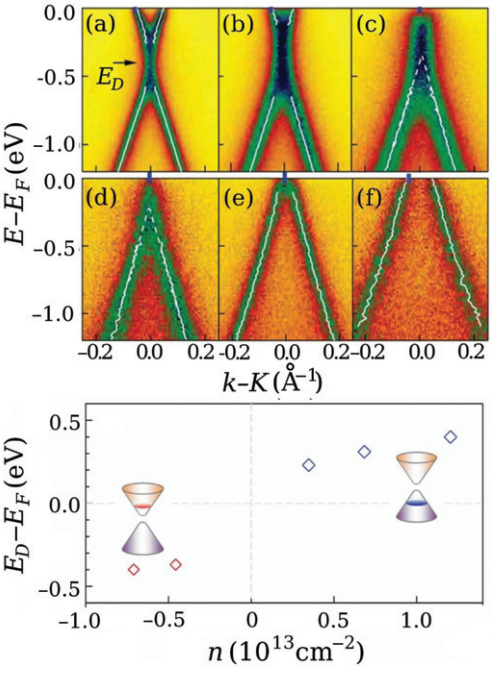

Figure 104. Evolution of the band structure of graphene for increasing concentration of adsorbed NO_2 gas molecules on its surface. (a) As-grown sample and (b–f) various doping level of graphene. The lower panel is the plot of the Dirac point energy E_D as a function of carrier concentration (Reprinted figure with permission from S.Y. Zhou *et al.*, Physical Review Letters, 101, 086402, 2008 [515]. Copyright © (2008) by the American Physical Society.).

composed of repulsive interactions and van der Waals interactions [514]. However after exposure to adsorbates, the intra-molecular charge transfer and re-hybridization of the molecular orbitals of graphene due to the interaction with adsorbates lead to a change in the electronic properties. Thus, the conductance of graphene is sensitive to adsorption of gas molecules such as NO_2, H_2O, NH_3 and CO [49]. According to Hall measurements, the NO_2 and H_2O behave as acceptors on the graphene surface while NH_3 and CO are donors. An increase in the concentration of adsorbed molecules leads to an increase of the induced charge carriers in a single layer of graphene, and step-like changes in its resistance. Moreover, experimental investigation of the adsorption of gas molecules on graphene [515] has shown that adsorption changes the electronic properties of graphene through breaking of its symmetry and doping. A metal–insulator transition has been observed in graphene after exposure to the NO_2 gas. This transition was reversible since annealing of the sample or exposure to high proton flux led to closing of the graphene bands. The evolution of the band structure obtained with ARPES as a result of increasing the concentration of NO_2 on the graphene surface is presented in Figure 104. The doping by adsorbed molecules shifts the energy bands of graphene. The Dirac points E_D for the as-grown sample is located 0.4 eV below the Fermi level, i.e. the sample is *n*-doped. The adsorption of NO_2 results in hole doping. Therefore, an increase in the gas concentration shifts the whole band structure up converting

the doping to *p*-type. The Fermi velocity and the electron–phonon coupling have been found to be independent of doping.

The adsorption of aromatic molecules has been studied experimentally with Raman spectroscopy and has been shown to break the symmetry of graphene [516,517]. It was observed that monolayers of graphene sandwiched by aromatic molecules resulted in splitting of the *G*-band [516]. This *G*-band splitting was attributed to breaking of the six-fold symmetry of the graphene sheet and lifting of the two-fold degeneracy of the optical phonon bands at the Γ point resulted from the change of the spring constant induced by the adsorption. The adsorption of the aryl group, which was shown to form a bond with the graphene surface [517], has been found to increase significantly the electrical resistance of graphene. It has been proposed that bonding between the adsorbates and the graphene surface changes the sp^2 hybridization to sp^3, which induces a gap. Additionally, it was experimentally found that the type of doping and its magnitude can be controlled by the type of adsorbed molecules [518,519]. Moreover, the adsorption of dipolar molecules (such as water) has been observed in [398] to provide *p*-type doping of graphene. Doping by dipolar molecules also has been found to induce hysteresis in the field effect behavior of graphene, i.e. a shift of the maximum of the resistance relating to zero voltage arising from the dipolar nature of the adsorbates. Exposure in vacuum was found to reduce the hysteresis effect for some dopants due to the removing of the adsorbed molecules from the graphene surface, but additional heat treatment was seen to be more effective in removing the adsorbed molecules. Moreover, an exposure of graphene samples to NH_3 gas converts the *n*-type graphene to *p*-type.

8.2.2. *Adsorption of non-metals on graphene: theoretical approaches*

Several theoretical groups have been working extensively on adsorption of different molecules on graphene, which will be discussed below. The interaction between adsorbed organic molecules and the graphene surface is found to be rather low [514]. The long-range electron correlation was found to be responsible for the attraction of the adsorbed molecule to graphene. However in some cases, the adsorbed molecules were found to be able to bond to the graphene surface [520–524].

The very first theoretical paper devoted to the adsorption of organic molecules on the graphene surface was reported in [520] and demonstrated that adsorption can induce magnetism in graphene. The C adatom on the surface of graphene was found to make a bond to two neighboring carbon atoms, which resulted in disturbance of the graphene planarity. The distribution of the four valence electrons of the adatom is shown in Figure 105. There, two electrons participate in bonding with the graphene surface (sp^2 hybridization): one forms a dangling sp^2 bond and the other one is shared between the sp^2 bond and π orbital, which is orthogonal to the surface. This π orbital does not form a band, therefore remaining localized and spin-polarized. It was shown that the magnetic moment of the adatom is non-zero only for the equilibrium position, where its magnitude is $0.5\mu_B$.

In the graphene lattice, the carbon atoms having four valence electrons donate three of them to form bonds with the nearest carbon atoms, while the fourth electron participates in the formation of the π orbitals. Moreover, the fourth electron can participate in interactions with an adsorbate, such as a F, O and N atom, which lack

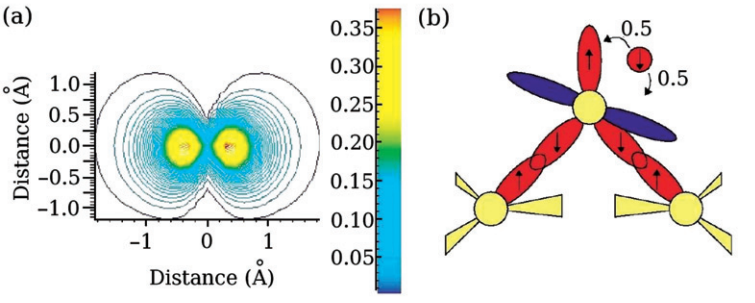

Figure 105. (a) The spin density ($e\,Å^{-3}$) of an adatom in its equilibrium position on the graphene surface. (b) The bond orbitals through the adatom and two carbon atoms belonging to graphene (Reprinted figure with permission from P.O. Lehtinen *et al.*, Physical Review Letters, 91, 017202, 2003 [520]. Copyright © (2003) by the American Physical Society.).

one, two and three electrons in their outer electron shell, respectively [522]. The F atom adsorbs above the carbon atom with an adsorption energy of −2.01 eV and inter-atomic distance of 1.56 Å. The O atom adsorbs to two carbon atoms with adsorption energy of −2.41 eV and inter-atomic distance of 1.46 Å. The electrons of the F and O atoms are paired and possess no polarization. The adsorption of polarized molecules, such as a N atom which has unpaired electrons, results in a magnetic moment of $0.84\,\mu_B$ per N atom. The N atom adsorbs above the carbon atom with adsorption energy of −0.88 eV and inter-atomic distance of 1.46 Å. The unsaturated electrons of the N atom are spin polarized, inducing polarization of the electrons near the carbon atoms in graphene. Moreover, the N atom is an electron acceptor and its adsorption leads to *p*-type doping of graphene. The orbitals of the N atom generate a peak in the DOS and create a strong acceptor level 0.39 eV below the Dirac point. The partially occupied orbital of the N atom is split by the Hund-like exchange interaction in such a way that the spin-up component is fully occupied and located 2.05 eV below the Dirac point, while the spin-down component is unoccupied and located at 0.39 eV, thereby producing strong acceptor behavior by the N atom. The P atom adsorbed on graphene is also spin-polarized and exhibit a magnetic moment of $0.86\,\mu_B$ [525]. Moreover, the S and P atoms has been found to make chemical bond to the carbon atoms in graphene and for the S atom due to the strong hybridization between S 2p states and C 2p states the band gap of 0.6 eV has been induced.

Theoretical investigations [521] do provide support to the experimental results, where the gap was opened by adsorption [515,516]. In fact, CrO_3 adsorbed on graphene was found to act as an acceptor [521]. The alteration of the electronic properties of graphene with CrO_3 adsorption for several stable configurations of CrO_3 is presented in Figure 106. Orientation of the CrO_3 molecule on the graphene surface and its adsorption site are found to affect the efficiency of the charge transfer between graphene and the adsorbate, thereby gradually modifying the properties of graphene. The charge exchange between graphene and the CrO_3 molecule was found to lower the Fermi level and the graphene band. Charge transfer of $0.17\bar{e}$ shifts the Fermi level by 0.69 eV, that of $0.11\bar{e}$ by 0.64 eV, and $0.20\bar{e}$ by 0.8 eV, as shown in Figure 106(b–d), respectively. The binding of the CrO_3 molecule to graphene (Figure 106b) induces a gap of 0.12 eV at the Dirac point due to the breaking of the

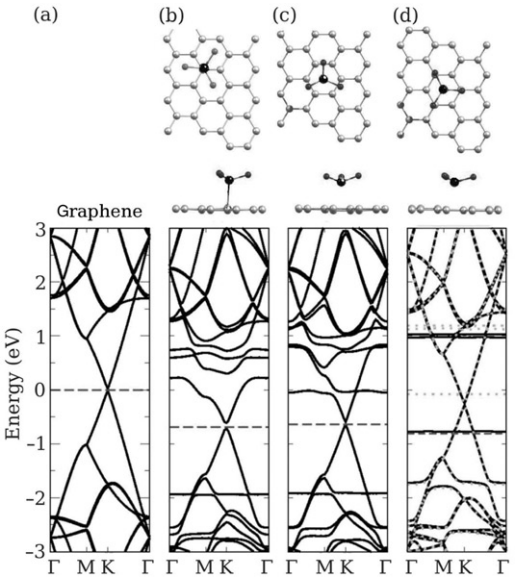

Figure 106. Influence of the adsorption of a CrO_3 molecule and its orientation on the graphene surface on the electronic properties of graphene: (a) pristine graphene, (b–d) graphene with adsorbed molecules. The horizontal dashed line is the Fermi level. In (d) the filled and dotted lines corresponds to the majority and minority of the spin levels, respectively (Reprinted with permission from I. Zanella *et al.*, Physical Review B, 77, 073404, 2008 [521]. Copyright © (2008) by the American Physical Society.).

sublattice symmetry. Another confirmation of the influence of the adsorbed molecules on the band gap has been found in [526], where the adsorption of polar molecules, such as $NH_3(CH)_6CO_2$ and $NH_3(CH)_{10}CO_2$ was shown to be able to change the spin symmetric gap to be spin asymmetric. The modification of the gap has been explained by the presence of an electric field induced by the adsorption of polar molecules. It was also shown that induced spin-asymmetry can be controlled by the modification of the dipole moment in the chain through changing the size of the chain formed by the adsorbed molecules.

The interaction of the graphene surface with the adsorbed gas molecules, such as NO_2 and N_2O_4, is found to lead to paramagnetic or diamagnetic behavior, depending on whether strong doping or no doping occurs, respectively [397]. The diamagnetic N_2O_4 has no unpaired electrons, its HOMO is more than 3 eV below the Fermi level of graphene and no charge transfer from N_2O_4 to graphene occurs. However, the LUMO of the N_2O_4 molecule is localized near the Dirac point and can be populated by the electrons from the graphene flake through thermal excitation, thereby allowing the N_2O_4 to act as an acceptor. A paramagnetic adsorbate (such as NO_2) on the graphene surface possesses a partially occupied molecular orbital split by the exchange interaction. As a result, its spin-up component is located 1.5 eV below the Dirac point of graphene and is fully occupied, while the spin-down is unoccupied and located 0.4 eV below the Dirac point, thereby producing strong acceptor behavior in the NO_2 molecule. It was assumed that for graphene exposed to the NO_2 gas, both NO_2 and N_2O_4 components should participate in charge exchange

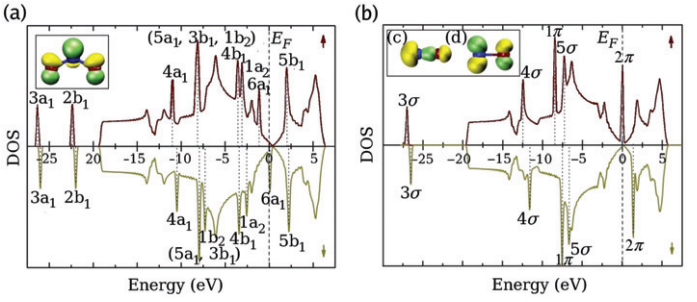

Figure 107. (a) The spin-polarized DOS of NO_2 on graphene where the inset is HOMO and LUMO for NO_2. (b) The spin-polarized DOS of NO on ghraphene, where insets are (c) the 5σ orbital and (d) the HOMO and LUMO (Reprinted figure with permission from O. Leenaerts *et al.*, Physical Review B, 77, 125416, 2008 [527]. Copyright © (2008) by the American Physical Society.).

with the graphene surface, so that several acceptor levels would be induced in the graphene band structure. One is far below the Dirac point, while second is close to it.

However, according to [527,528] not all paramagnetic molecules are strong dopants. The paramagnetic NO_2 molecule significantly dopes graphene with holes (as was also seen in [397]). The spin-polarized DOS of the NO_2 molecule is presented in Figure 107(a). The LUMO of NO_2 ($6a_1,\downarrow$) was found to be located 0.3 eV below the Dirac point, thereby providing large charge transfer from the graphene surface to the NO_2 molecule. The HOMO ($6a_1,\uparrow$) is located close to Dirac point and causes the charge transfer in the opposite direction from the NO_2 molecule to graphene. The total charge transfer from graphene to the NO_2 molecule lies in the range 0.89ē–1.02ē depending on the orientation of the NO_2 molecule. The magnetization of such a system is $0.862\,\mu_B$. The NO molecule, which is also paramagnetic, acts as a weak donor, providing a transfer of 0.005ē–0.018ē to graphene. The DOS for a NO molecule on graphene is presented in Figure 107(b). In this system, the half-filled HOMO is degenerate and located only 0.1 eV below the Dirac point of graphene. Therefore, charge transfer from graphene to the NO molecule is insignificant and can be compensated for by orbital mixing which causes charge transfer in the opposite direction. In the same paper [527], adsorption of diamagnetic molecules, such as NH_3 (donor) and CO (donor) was found to cause the low charge transfer between graphene and the adsorbate. Similarly, the acceptor behavior of NO_2 and donor behavior of NH_3 was seen in [529], while CO was found to be a weak acceptor and NO a weak donor. The *p*-doping of graphene by NO_2 molecules is also found in [530], where a shift of the graphene bands occurs and the Dirac point is shifted by ~0.2 eV above the Fermi level. Oxygen molecule was also found to be a possible acceptor. In [531], tetracyanoethylene molecule was shown to act as electron acceptor as well, converting graphene to *p*-type. The concentration of the adsorbed tetracyanoethylene molecules has been shown to control the position of the Fermi level relative to the Dirac point. The adsorption of an anion radical of tetracyanoethylene was effective in inducing a spin density in graphene because of the spin splitting and the partially filled π^* orbitals of this anion radical.

The effect of interaction of a single water molecule with the graphene surface was found to depend on the orientation of the water molecule [527]. In an energetically

favorable position of a water molecule placed on graphene (when one of the hydrogen atom is located closest to the surface, thereby providing efficient electron transfer from graphene to the water) it acts as an acceptor. However, if the oxygen atom is located closest to the surface, the electron transfer is from the oxygen atom to graphene so the molecule acts as a donor. When several water molecules are near the graphene surface, they tend to build a cluster [532,533], where each water molecule uses one of its hydrogen atoms to make a hydrogen bond with the oxygen atom of the neighboring molecule. It was found in [532] such that a water cluster tends to contain as many water molecules as possible, but this cluster has a weak influence on the electronic properties of graphene. The impact of the water adsorbates on the electronic properties of graphene has been found to be more effective when graphene is placed on a defective SiO_2 substrate [534] because the dipole moments of adsorbates shift the defect states of the substrate according to position of the conduction band of graphene thereby initiating doping.

Berashevich and Chakraborty [533] showed that adsorption of water molecules on nanoscale graphene, where the edge states and the symmetry of the lattice play the most important roles, and exhibit different effects on its electronic properties than those observed in [532]. Here the water cluster makes a link to the graphene surface through the oxygen atom of a single water molecule. The water link donates an electron to graphene, while most of the water molecules in the cluster act as acceptors. The water cluster, which is linked to the graphene surface somewhere close to the center of the nanoscale graphene, unrolls in the direction of the armchair edges, which are known to have lower energy than the zigzag edges [402,403]. The highest possible symmetry of pristine nanoscale graphene was found to be D_{2h} planar symmetry with an inversion center, which is a metastable state competing with the state with C_{2v} symmetry. The interaction of graphene with water molecules and the charge transfer between them, which is unequal for the two sublattices, leads to the breaking of the D_{2h} symmetry and gives rise to a state with C_{2v} symmetry. The state with C_{2v} symmetry is characterized by ferromagnetic ordering of the spin states along the zigzag edges and antiferromagnetic ordering between the edges. This enhances the gap in nanoscale graphene. The size of the gap is found to depend on the efficiency of the charge transfer between graphene and the adsorbate. Thus, alteration of the number of water molecules in the cluster changes the cluster orientation relative to the graphene surface and therefore the charge exchange between the adsorbate and graphene. This leads to a modification of the band gap (Figure 108a). Moreover, because of the influence of the efficiency of the charge exchange on the band gap, adsorption of different gas molecules on the graphene surface induces band gaps of different sizes, as presented in Figure 108(b) for single NH_3, H_2O, CO or HF molecules.

Opening of a band gap in monolayer and bilayer graphene has also been demonstrated by adsorption of water molecules on the surface [535]. There, the sublattice symmetry was broken due to the displacement of the carbon atoms (namely the vertical distortion of the graphene lattice) as a result of interaction with the adsorbed molecules. For monolayer graphene, the adsorption of water induces a gap of 18 meV, while ammonia opens a gap of 11 meV. For bilayer graphene (characterized by the parabolic bands near the charge neutrality point) a direct gap

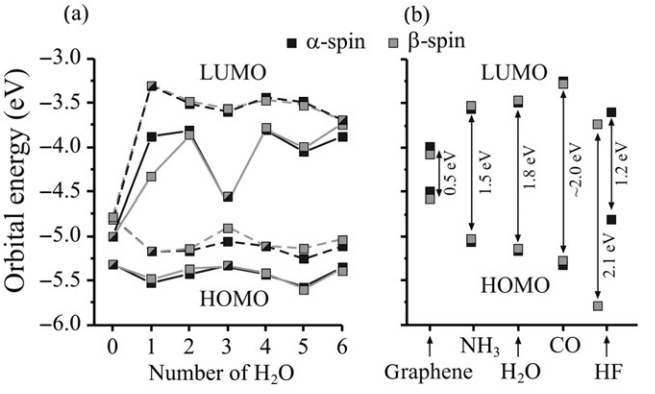

Figure 108. The effect of adsorption of water and gas molecules on the energy of the HOMO and LUMO orbitals of graphene. (a) The band gap for graphene for different numbers of carbon rings along the zigzag edges, $N=3$ (solid line) and $N=5$ (dashed line). (b) The alteration of the gap with the adsorption of different molecules on its surface. The pure graphene due to the presence of the confinement effect is characterized by the band gap of 0.5 eV (from [533]).

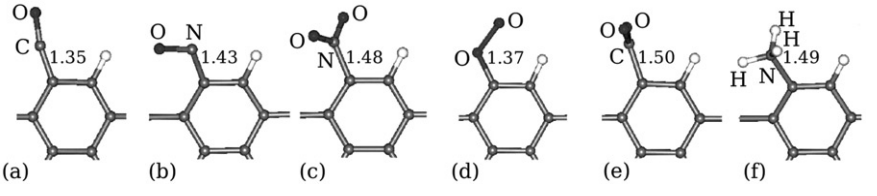

Figure 109. Optimized structures of molecules adsorbed on armchair nanoribbon with single unsaturated dangling bond: (a) CO, (b) NO, (c) NO_2, (d) O_2, (e) CO_2 and (f) NH_3 (Reprinted with permission from B. Huang *et al*., The Journal of Physical Chemistry, C112, 13442, 2008 [523]. Copyright © (2008) by the American Chemical Society.).

of 30 meV was obtained for water adsorption and an indirect gap, located far from the K point, of 42 meV for ammonia.

Adsorption of gas molecules on the surface of a graphene ribbon with armchair-shaped edges, where each armchair edge had a single unsaturated dangling bond while the other dangling bonds are saturated with hydrogen, was studied in [523]. The dangling bonds at the armchair edges are chemically active, and the adsorbed molecules prefer to bond to carbon atoms possessing a dangling bond. The optimized structures of armchair nanoribbons with adsorbed gas molecules are presented in Figure 109. The armchair nanoribbon is naturally in the semiconducting state, but adsorption is found to change its electronic properties. Adsorption of CO and NO molecules leads to the formation of impurity states in the band gap, thereby decreasing its size. For a CO molecule adsorbed on graphene, two half-occupied states are induced, while adsorption of NO induces non-localized, fully-occupied states which are hybridized with states in the valence band. The adsorption of CO_2 and O_2 molecules leads to *p*-type doping. The band structure of graphene with an adsorbed O_2 molecule is presented in Figure 110(a). The impurity states induced by

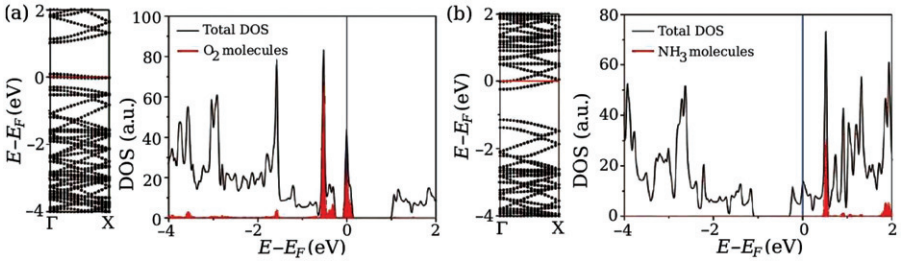

Figure 110. The band structures and DOS of the armchair nanoribbon with adsorbed molecules: (a) O_2 and (b) NH_3. The Fermi level is set to zero (Reprinted with permission from B. Huang *et al.*, The Journal of Physical Chemistry, C112, 13442, 2008 [523]. Copyright © (2008) by the American Chemical Society.).

these molecules are localized near the valence band. These impurity states are strongly localized and mainly contributed by the adsorbed molecules, therefore suggesting insignificant enhancement of the conductance of graphene in an applied electric field. Adsorption of a NH_3 molecule significantly changes the electronic properties of graphene by changing it to an *n*-type semiconductor, whose band structure is presented in Figure 110(b). The transition to an *n*-type semiconductor occurs because of the shift of the Fermi level into the conduction band. Moreover, the states near the Fermi level are found to be created mainly by the carbon atoms, thereby suggesting a significant enhancement of the conductance of graphene in the NH_3 gas environment. The *n*-doping of graphene by adsorption of NH_3 molecules has received experimental confirmation in [536,537], where the Dirac peak was found to be shifted after exposure to NH_3 gas. The possibility of chemical doping of graphene through adsorption was also discussed in [538], where adsorption of organic complexes was found to induce *n*- or *p*-type doping depending on the type of the adsorbates, due to the charge exchange between them and the graphene surface.

Combination of several adsorbed molecules play important roles in the formation of stable configurations of the molecules adsorbed on graphene. When several molecules are adsorbed on the graphene surface, they are found to interact with each other [539]. The interaction strength between two molecules is found to diminish very slowly with increasing distance between them. The sign of the interaction was shown to depend on the location of the adsorbed molecules relative to the sublattice site: two molecules residing on the same sublattice repel each other but they attract when on different sublattices. Another example is adsorption of several hydrogen molecules on a boron-doped structure, which was found to form a H dimer-like structure due to the interaction between hydrogen molecules [540]. Another interesting result is the adsorption of the phenyl group (C_6H_5), where the armchair edges have shown higher reactivity than the zigzag edges [541]. The stability of a C_6H_5 molecule adsorbed on the graphene surface is found to increase due to the adsorption of a second C_6H_5 molecule. The possibility of manipulating the interaction between aromatic compounds and the graphene surface by introducing functional groups was proposed in [542].

Vacancy defects and dopants within the graphene sheet are predicted to attract the adsorbed molecules as well [529,543–548]. In [545], Al-doped graphene sheets

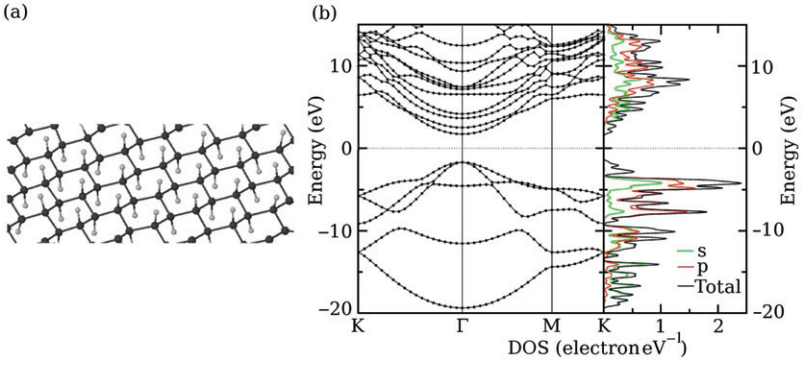

Figure 111. (a) The lattice structure of graphane in the chair conformation. (b) The band structure and DOS of graphane in the chair conformation. The DOS is presented for s and p symmetries (Reprinted figure with permission from J.O. Sofo *et al.*, Physical Review B, 75, 153401, 2007 [549]. Copyright © (2007) by the American Physical Society.).

were shown to have a higher binding energy with H_2CO molecule than for the pristine graphene and occurrence of the orbital hybridization between the H_2CO molecule and the induced Al atom has been reported. Boron-doped graphene is found to have significantly decreased the adsorption energy for hydrogen, due to the electron deficiency [540,546]. Another example of the reduction of the binding energy of the adsorbed molecules is the presence of the Stones–Wales defects or single vacancy defect. The presence of defects initiates the bonding between a SH group and the graphene surface [547], whereas pristine graphene has shown low reactivity against the triol group. Similarly, graphene doped with B, N, Al or S is found to be more reactive in binding with gas molecules whose adsorption was predicted to modify the conductivity of graphene [548]. Moreover, since defects attract the adsorbates, it was found in [544] that the adsorption of O_2, H_2 or N_2 is able to remove adatom defects from graphene.

The main effect of the adsorption of gas and organic molecules on the electronic structure of graphene consists of doping of graphene as a result of charge exchange between the adsorbate and the graphene surface. In cases when an unequal doping of the two sublattices of graphene occurs, the adsorption is found to be capable of breaking the symmetry of the lattice, thereby opening a band gap.

8.2.3. *From graphene to graphane*

It was predicted theoretically that adsorption of hydrogen atoms over the whole graphene surface leads to formation of a two-dimensional hydrocarbon – graphane [549]. Graphane, hydrogenated from both sides of the carbon plane has two main conformations: a chair conformation where the carbon atoms belonging to different sublattices are hydrogenated from different sides of the plane, and the boat conformation for which the bonded hydrogen atoms alternate in pairs at the plane sides. The lattice structures of these two conformations are different. In the chair conformation all carbon bonds are of the same length (1.52 Å), while for the boat conformation there are two types of carbon bonds with different lengths, one is

1.52 Å and the other 1.56 Å. The chair conformation is more stable and the difference in the binding energy between two conformations is 0.055 eV per atom. There is not much of a difference in the electronic structure of each conformation, since they both have a direct band gap of 3.5 eV (chair) and 3.7 eV (boat) at the Γ point (within the GW approximation, the size of band gap of the chair conformation is 5.4 eV [550]). The lattice structure, band structure and the density of the states for the chair conformation are presented in Figure 111. The top of the valence band is mainly of *p* symmetry and is doubly degenerate, thereby possessing two different effective masses. Attaching a hydrogen atom to each carbon atom changes the hybridization of the bonds from sp^2 to sp^3, and leads to opening of a gap as a result of the removal of the conducting π bands. However for graphane nanoribbons, the size of the band gap is found to slightly decrease [551] with increasing width of the nanoribbons. Another theoretical investigation [552] predicted that for the chair conformation covering of the graphane surface by hydrogen atoms most likely would not be uniform, in particular the sequence of the up and down H atoms would be broken (frustrated). In the ideal structure of the chair conformation for each side of the graphene lattice, the hydrogen atoms are supposed to bond to carbon atoms belonging to the same sublattice. Therefore, the H frustration forming the uncorrelated H frustrated domains of significant percentage would induce the in-plane dimensional shrinkages into the graphane lattice.

Experimentally it was shown that hydrogenation by the e-beam irradiation of single- and double-layer graphene deposited on the Si wafer coated with SiO_2 changes the lattice structure of graphane [553]. The e-beam irradiation of graphene induces the intense D band in the Raman spectra thus indicating the presence of sp^3 distortion, and its intensity gradually grows with increasing dose of e-beam irradiation. The following intense laser excitation of the hydrogenated structure reduces the D band intensity. Moreover, it was found that the hydrogenated graphene can be restored by thermal annealing which disorbes the bound hydrogen atoms. It was found that near the room temperature, the hydrogen atoms are more reactive to single-layer graphene than that with a double layer. The effective reactivity of single-layer graphene was explained by distortion, or a degree of freedom in the single layer, not present in a double-layer graphene. The possibility of the reversible hole doping of hydrogenated graphene by oxygen molecules has been indicated.

In a later experiment, opening of a gap with hydrogenation of the graphene surface from one side was reported [280]. Treating the graphene surface with atomic hydrogen, the behavior of graphene changed from the conducting to the insulating state. In fact, the resistivity of graphene is increased by up to 100 times (Figure 112). The characteristics of hydrogenated graphene were stable at room temperature for many days. It was proposed that the deformation of the graphene lattice due to the convex shape of the graphene surface stabilizes the hydrogenated graphene. Further annealing of the sample restores the metallic behavior. However, both the hydrogenated graphene and the restored metallic graphene were *p*-doped, while as-prepared graphene was undoped. The changes in the characteristics of graphene after annealing have been attributed to the presence of induced vacancies. Graphene on SiO_2 substrate hydrogenated from one side had the D peak (attributed to the formation of C-H sp^3 bonds) half that for hydrogenated free-standing graphene membrane, thereby proving that membrane is hydrogenated from both sides.

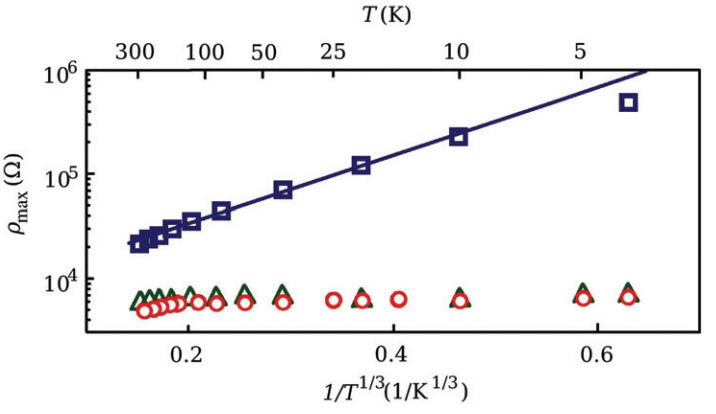

Figure 112. Temperature dependence of the resistivity of pristine graphene (circles), the hydrogenated graphene (squares) and graphene after annealing (triangles). The solid line is a fit obtained from the hopping dependence $\exp[(T_0/T)^{\frac{1}{3}}]$, where T_0 is a parameter that depends on gate voltage (Reprinted figure with permission from D.C. Elias *et al.*, Science, 323, p. 610, 2009 [280]. Copyright © (2009) The American Association for Advancement of Science.).

Influence of hydrogenation on the electronic and magnetic properties of graphane has been recently investigated in several theoretical works [554–556]. H-vacancy in the graphane lattice generates a localized state characterized by unpaired spin. Therefore, for several H-vacancy defects their spins can be ferromagnetically or antiferromagnetically ordered. In [554], it was shown that for the graphane sheet hydrogenated from one side the ferromagnetic ordering of the spins of the localized states located on other side of the sheet occurs. The Curie temperature has been estimated to be in a range between 278 and 417 K. The size of the band gap of such sheets is found to be 0.46 eV which is much smaller than that for graphane, hydrogenated from both sides. The possibility to generate the magnetic moment for graphane containing H-vacancy pockets has also been considered in [555]. However, in [556] it was predicted that the ordering of the H-vacancy defects located from one side of the graphane plane depends on its distribution over the plane. It was found that only for the nearest location of the defects significant energy gap between the states characterized by the ferromagnetic and antiferromagnetic ordering is achievable. However, with increasing distance between the defects, the energy difference decreases because the constructive contribution of the spin tails of the localized states located on the same sublattice (considered for the graphene lattice) to the total energy of the system diminishes. Moreover, for graphane containing many vacancy defects on one side of the plane significant distortion of its lattice is noticed and contribution of this distortion into the total energy is found to be destructive for the energy difference between the states with ferro- and antiferromagnetic spin ordering. For the H-vacancy defects distributed between two sides of the graphane plane but located close to each other, the antiferromagnetic ordering of their spins is found to be energetically preferable as a result of the location of the localized states on different sublattices. The influence of the degree of hydrogenation on the electronic properties also has been considered in [556]. Hydrogenation of the edges of the graphane sheet therefore plays an important role

in defining the size of the gap. The gap is found to increase from 3.04 to 7.51 eV when hybridization of the edges is changed from sp^2 to sp^3 type, which is performed by hydrogenation of the edge carbon atoms by one or two hydrogen atoms, respectively. The fluctuation of the size of the gap also takes place with changing the concentration of the H-vacancy defects and their distribution between the sides of the plane.

The interplay of pure graphene and hydrogenated graphene due to the different size of their gaps has been shown to be a way to create periodic multi-quantum systems [557] that has the potential for application in nanoelectronic devices. The possibility of tuning the gap by functionalization of the entire graphene surface has been also discussed elsewhere [558,559]. It was shown that the gap can be changed between 0.64 and 3 eV by using various functional groups. For example, bonding of lithium atoms to graphene has been shown to disrupt the planarity of the graphene lattice and gives rise to the metallic behavior in graphene [560]. Another way to manipulate the size of the bandgap in graphane is via the elastic strain [561]. The stiffness of graphane is less (27%) than that of graphene due to the modification of its lattice (hybridization and planarity) induced by bonding of the carbon atoms with the hydrogen atoms. The strain (ϵ) applied in the elastic range significantly modifies the gap. For example, for a strain ranging from 0.0 to ~0.13 the gap grows from 5.5 to 6.5 eV (in the G_0W_0 approximation), but for higher values of strain the gap decreases. For $\epsilon > 0.3$ it drops down to 2.0 eV.

8.2.4. *Adsorption of metal atoms on graphene: experimental results*

The adsorption of metal atoms on the graphene surface has been extensively studied by several experimental groups [140,255,504,562–564]. In investigations [564] involving ARPES, the adsorption of Na atoms was found to change the band structure of graphene (degradation of the linear π band and developing new parabolic band), while in others [140,255,504] the adsorption of the adatoms induced doping of graphene. The adsorption of potassium on the surface of bilayer graphene grown on a SiC substrate was considered elsewhere [140]. It was declared that the symmetry of bilayer graphene in an as-prepared sample was broken due to the dipole field created between the depleted SiC and the charge accumulated on the surface of the top layer. The adsorption initiated electron exchange between the lone valence electron in potassium and the surface layer of graphene, thereby altering the concentration of the accumulated charge on the surface. This led to modification of the induced dipole field, which controls the size of the gap through the symmetry breaking process. The alteration of the band structure of bilayer graphene by potassium adsorption is presented in Figure 113. Low concentration of potassium on the graphene surface results in a band gap while increasing its concentration leads to reduction of the gap and finally closing of the gap. When the contribution of doping from the adsorbates exceeds the impact from the built-in dipole field, the gap is reopened. Therefore, when the number of electrons per unit cell transferred from potassium to graphene is $0.0125\bar{e}$, the built-in dipole field of the sample is neutralized, which closes the gap. Extra doping induces a field in the direction opposite to the built-in dipole field. Therefore, if charge transfer of $0.0125\bar{e}$ is considered to be non-doped because of suppression of the intrinsic dipole field

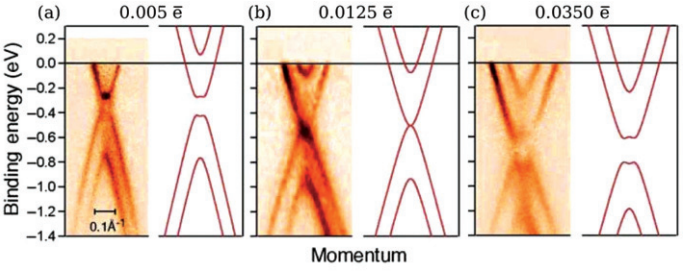

Figure 113. Alteration of the band structure of bilayer graphene by the potassium adsorption. The left picture in each panel are the experimental results, the right are the theoretical estimations obtained from tight-binding calculations. The number of electrons per unit cell transferred from a lone pair of a valence electron of potassium to the graphene surface is indicated at the top of the panels (Reprinted figure with permission from T. Ohta *et al.*, Science, 313, p. 951, 2006 [140]. Copyright © (2006) The American Association for the Advancement of Science.).

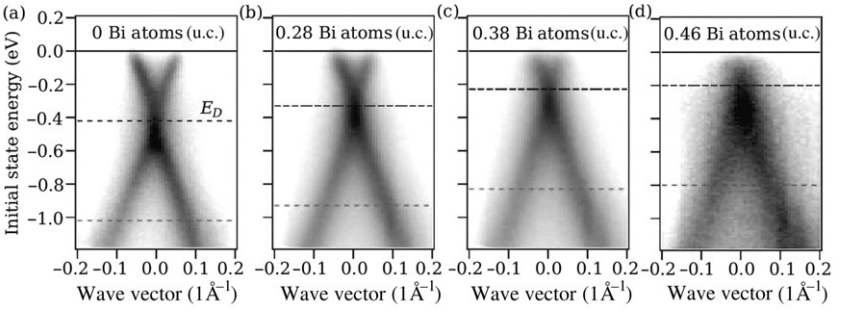

Figure 114. The experimentally obtained band structure of the epitaxial graphene on the SiC substrate doped by the adsorbed Bi atoms. Light and dark areas correspond to the low and high photoelectron current, respectively (Reprinted with permission from I. Gierz *et al.*, Nano Letters, 8, 4603, 2008 [504]. Copyright © (2008) by the American Chemical Society).

(see the crossing of the conduction and valence band of graphene in the middle panel in Figure 113), then relative to this case graphene in the left panel is *p*-doped, while that in the right panel is *n*-doped. Therefore, the built-in dipole field is acting as an external electric field which shifts the bands relative to the Fermi level and allows one to regulate the doping of graphene. Similar experiments have been performed for a single graphene layer on a *n*-type 6H-SiC substrate [255], and *n*-type doping by potassium adsorption has been obtained: the doping shifted the bands to higher binding energy. Moreover, the bands were found to be strongly renormalized near the Dirac point and the Fermi level, due to contributions from electron–electron, electron–phonon and electron–plasmon couplings.

The doping of epitaxial graphene on SiC substrate through adsorption of Bi and Sb alkali atoms has been performed experimentally in [504]. The evolution of the band structure of graphene due to its *p*-doping by alkali atoms is presented in Figure 114. Epitaxially grown graphene on a SiC substrate is naturally *n*-doped and its Dirac point is shifted into the valence band by ~420 meV, as shown in

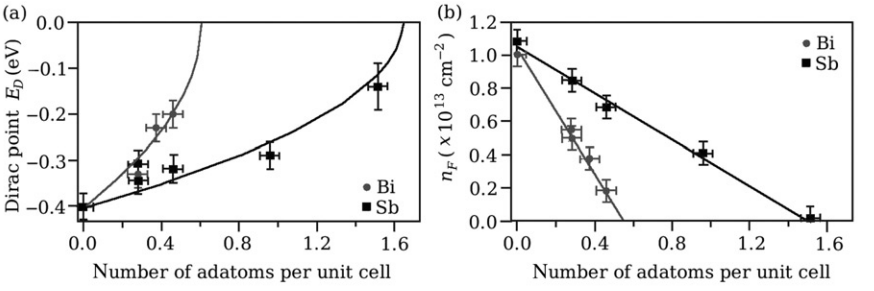

Figure 115. The alteration of (a) the position of the Dirac point E_D and (b) the free charge density n_F due to doping of graphene by the Bi and Sb atoms. Solid line – theoretical estimation is from $E_D = -\sqrt{\pi}\hbar\upsilon_F\sqrt{N_0 - N_h}$, where the Fermi velocity $\hbar\upsilon_F = 6.73$ eVÅ was defined experimentally, N_0 and N_h are the numbers of the electrons in the conduction bands and the holes doped into graphene, respectively. The concentration of the free charge carriers were found as $n_F = (k_F)^2\pi$, where k_F is the Fermi wave vector (Reprinted with permission from I. Gierz *et al.*, Nano Letters, 8, 4603, 2008 [504]. Copyright © (2008) by the American Chemical Society.).

Figure 114(a). The linear dispersion of the conduction and valence bands close to the Dirac point has been indicated. The doping shifts the Dirac point toward the Fermi level, which corresponds to *p*-type doping, while the linear dispersion of the bands remains unchanged. The shift of the Dirac point and the change of the free carrier density (n_F) as a function of the number of adatoms on the graphene surface is presented in Figure 115. It was observed that the Dirac point approaches the Fermi level and the free charge carrier density is reduced with increasing adatom coverage. For an element with higher electron affinity such as a gold, *p*-type doping was also obtained and for two gold atoms per graphene the shift of the Dirac point in comparison to pristine graphene was found to be 520 meV. The bands of graphene doped by gold are narrower than when doped by Bi or Sb.

In an experiment [565] where graphene was in contact with In, a shift of −400 meV of the Fermi level relative to the Dirac point, i.e. *n*-type doping, has been observed. The doping was also assigned to the charge transfer between the In contact and graphene. The shift of the Dirac point due to the increased coverage by adsorbed atoms such as Ti, Fe and Pt, was also seen in [566]. There, the adsorption of Ti atoms in the low coverage regime has shown a significant shift of the minimum in the gate-dependent conductivity towards negative gate voltage indicating the *n*-type doping of graphene. The shift induced by Ti adatoms was larger than that induced by Fe and Pt adatoms. The ineffective *n*-type doping of graphene by Pt atoms instead of the expected *p*-type doping predicted from the large difference of the work functions of Pt and graphene led to the conclusion that in addition to the work function difference, the interfacial dipole plays a crucial role in doping. Doping of the graphene layer and the asymmetric behavior of its spins induced by the metal adsorption have also been found in theoretical works [567–569]. Spin asymmetry has been attributed to the Coulomb potential [570], which can break the particle–hole symmetry under specific conditions.

The adsorption of Au and Pt atoms and their behavior on the graphene surface have been investigated in another experiment [562]. It was observed that metal atoms

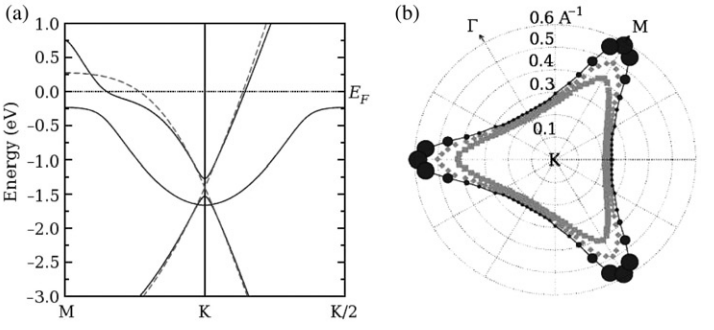

Figure 116. (a) The band diagram of the CaC_6 monolayer (solid line) plotted in the Brillouin zone of graphene (dashed line). (b) The influence of doping on the Fermi surface of the CaC_6 monolayer. Circles are the theoretical data from [576], where circle size is proportional to the electron–phonon coupling magnitude. Square and diamonds are the experimental results obtained in [577]. (Reprinted figure with permission from M. Calandra and F. Mauri, Physical Review B, 76, 161406, 2007 [576]. Copyright © (2007) by the American Chemical Society.)

tend to replace carbon atoms and can reside on single or multiple vacancies. Due to the attractive interaction between the metal atoms, they migrate to form clusters characterized by an unstable structure. It was also concluded based on magnitude of the activation energy for the in-plane migration (around 2.5 eV) that Au and Pt atoms can make covalent bonds with the carbon atoms. In another experiment [563], the effective dispersion of the gold nanoparticles on the graphene surface in the solution of gold and graphene has been obtained. Theoretically, it was shown that the gold–gold interaction is much stronger than the gold–carbon interactions [571,572], which explains why the formation of gold clusters occurs. The enhancement of the stability of the Pt and Au clusters on the graphene surface by induction of a carbon vacancy has been reported in a theoretical work [573]. Moreover, the unique influence of adsorption of the Au_nPt_n clusters on the size of the band gap has been obtained theoretically in [574]. The cluster composition has been found to define whether graphene shows semiconductor or metallic behavior. In fact, Au, AuPt and Au_3Pt_3 on the graphene surface provide charge transfer from graphene to the clusters generating a metallic band structure. For Au on graphene, the spin-up and spin-down bands overlap exactly, producing a gapless band structure, while for AuPt and Au_3Pt_3 clusters the spin degeneracy is lifted and half-metallicity occurs. The Pt and Au_2Pt_2 clusters act as charge donors and induce a semiconductor band gap. In another theoretical work [575], adsorption of the Au_{38} nanoparticles has also been seen to make charge exchange with the graphene surface. Moreover, adsorption modified the electronic structure of originally gapless graphene causing mini-gaps and the formation of new Dirac points. For a moderate coverage of the graphene surface by the nanoparticles ($\approx 0.2\,nm^{-2}$), the periodic deformation of the graphene lattice and consequence opening of the gap of the few tens of meV was also observed.

8.2.5. *Adsorption of metal atoms on graphene: theoretical approaches*

Alteration of the electronic structure of graphene due to adsorption of metals has been extensively studied theoretically as well. The deposition of a Ca atom on the

surface of pristine graphene with formation of the CaC_6 stoichiometry was considered in [576]. There, the interaction between the Ca atom and graphene modified the electronic properties of graphene by inducing an impurity band and opening a gap (Figure 116). The induced Ca band was significantly hybridized with the π^* states of the carbon atoms which resulted in nonlinearity of this π^* band. An increase in the charge transfer from the Ca atom to graphene has been shown to influence the band structure (Figure 116b).

When metal atoms are adsorbed on the graphene surface, the dependence of the charge transfer between the adsorbate and graphene on the work function shift [568] is similar to that for graphene on a metallic substrate [512,513]. It was found that metal atoms of groups I–III are strongly bounded to the graphene surface when they are localized above the center of a graphene hexagon [568]. The distortion of the graphene surface and the subsequent alteration of the electronic structure of graphene induced by the adsorption of metal atoms of this group is minimal, whereas both the charge transfer and the work-function shift are found to be significant. Titanium and iron atoms make covalent bonds with the graphene surface, and their formation is found to depend on the position of the atoms relative to the graphene cells, which is consistent with other investigations [578]. The strongest binding is still obtained when these atoms are positioned in the middle of the graphene hexagon [568]. Due to the covalent bonding, strong hybridization of the electronic structures of Ti and Fe metals on the graphene surface is observed. Pd, Au and Sn atoms on graphene have been found to induce significant distortion into the graphene lattice and predicted to change the sp^2 hybridization to more covalently reactive sp^3 type. Moreover, the diffusion of these atoms along the hexagonal bond network is possible, and for Au and Sn atoms the diffusion barrier was very small. In [579], it was found that for graphene-metal contacts, metals such as Sc, Ca, Co, Ni and Ti, which have the 3d orbitals located around the Fermi level, can make a strong chemical bond to graphene. The chemical contact of Li and K atoms with graphene may occur via ionic bonding, while Au and Cu are expected to interact weakly with graphene. Therefore, the strength of the chemical interactions defines the width and height of the potential barrier at the metal–graphene interface thereby controlling the transport properties of contacts and the conductivity is predicted to be highest for the Ti–graphene contact for which the chemical interactions are strongest.

For a Cu atom on the graphene surface, the most stable configuration was found to be when the Cu atom was placed directly above a carbon atom, while for a Cu dimer it was when the dimer was above a carbon bond and perpendicular to the graphene surface [580]. Moreover, the electronic structure of graphene was different depending on whether a single Cu atom or a dimer had been adsorbed onto the graphene surface. A single Cu atom has been found to induce a magnetic moment into the adsorbate–graphene system due to the unsaturated s-electrons of Cu atom. For adsorption of transition metal atoms such as Fe and Ti, the most stable configuration is above the center of a graphene hexagon [581]. The Fe atoms are found to preferentially form a cluster, while Ti atoms cover the graphene surface uniformly. Moreover, increase of the concentration of the transition metals on the graphene surface was found to change the binding energy of the adsorbate. However in experimental work [566], the tendency to form a cluster have been seen for several transition metals, such as Ti, Fe and Pt. The possibility to initiate the transition of a

semiconducting armchair ribbon into a metal characterized by ferromagnetic properties and a large magnetic moment has been obtained with adsorption of Mg and B atoms [582].

Clustered coverage is favorable over homogeneous distribution for Zr atoms on the graphene surface [583], because the Zr–Zr bond is stronger than that of Zn–C. The Zr atoms formed bonds to graphene and their binding energy was found to depend on the Zr/C coverage ratio. Moreover, the study indicated that Zr and Zr_3 clusters on graphene undergo diffusion at room temperature, and that the diffusion barrier for the Zr_3 cluster is lower than for a single Zr atom. It was proposed that this diffusion is responsible for clustering of the Zr atoms. It was shown that the charge transfer from Zr atoms to graphene decreases as the Zr/C coverage ration increases and saturates at Zr/C ration ~0.375. Moreover, the Zr/graphene system was spin-polarized and it was concluded that for all configurations of the Zr atoms on the graphene surface the spin-polarization is provided by 4d orbitals of zirconium. The magnitude of the local spin polarization was around $2\mu_B$.

According to theoretical investigations performed in [584], the binding of alkali and alkaline-earth metal atoms above the center of the graphene hexagon was also found to be energetically favorable than that directly above the carbon atoms. The adsorption energy was found to be affected by the ionization energy, the radius of the metal ions, and the amount of charge transfer between the adsorbates and the graphene surface. Thus, adsorption was found to be possible if the difference between the change of the electrostatic energy after the charge transfer between the adsorbates

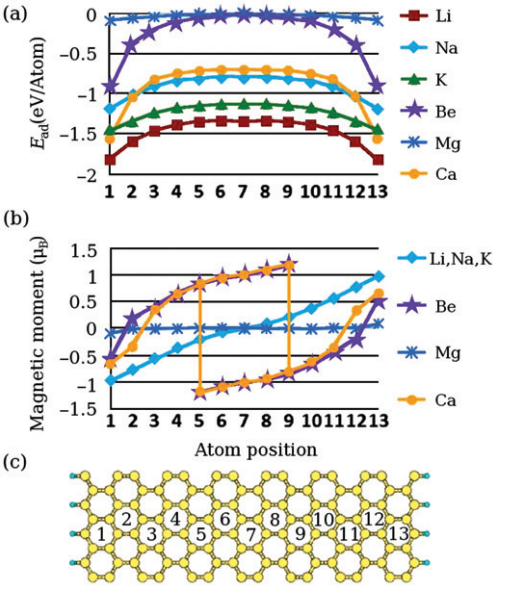

Figure 117. (a) The adsorption energy E_{ad} of the metal atoms as a function of their position on the surface of the zigzag nanoribbons in (c). (b) The magnetic moment induced by the adsorption of metal at various graphene sites numerated in (c) (Reprinted figure with permission from S.-M. Choi and S.-H. Jhi, Physical Review Letters, 101, 266105, 2008 [584]. Copyright © (2008) by the American Physical Society.).

and graphene was larger than the difference between the metal ionization energy and the work function of graphene. For metals which did not meet this condition, such as Be and Mg, the adsorption onto the graphene surface is not possible because the binding energy is zero. The adsorption energy is also found to vary depending on the lattice site, i.e. the position of the adsorbates in respect to the zigzag edges of graphene, as presented in Figure 117(a). The strongest binding is obtained for the edges of the zigzag nanoribbons because the electrostatic interactions between positively charged metal atoms and the zigzag edges are strongest in this case. Even for a Be atom, which cannot be adsorbed in the center of the graphene sheet, the binding energy is nonzero at a zigzag edge. Transfer of an electron from the metal atom to graphene creates a non-zero magnetic moment and its magnitude also depends on the lattice site (Figure 117b). If Li, Na or K atoms are adsorbed at the edges, the charge transfer from the metal to graphene results in a net magnetic moment of $-\mu_B$ because the donated electron occupies a single spin state localized on this edge. Therefore, in the case of Li, Na, K adsorbed at the center of the graphene structure, the transferred electron occupies both spin states equally thereby inducing no change in the magnetic moment of graphene. Other metal atoms placed close to the edges, such as Ca and Be atoms, can donate about $1.33\bar{e}$ which will occupy one spin state fully and the other partially, thereby generating the net magnetic moment of about $-0.66\mu_B$. At the center of the graphene structure, these metals can donate about $1.0\bar{e}$, equally distributed between both spin states, thereby leaving one electron on the metal atom, which is responsible for a net magnetic moment μ_B of the graphene–metal system. Moving the metal atom from one edge to the other, flips the spin orientation of the electrons in the metal atom due to their interaction with a certain spin state at the zigzag edge, creating hysteresis. The variation of the adsorption energy and the magnetic moment for different metals has been shown to be useful for developing spin-valve devices, where the position of the adsorbed metal on the graphene surface and magnetic moment induced by adsorption can be controlled by an external electric field. The dependence of the adsorption energy, net magnetic moment, and the electronic structure of the graphene–metal systems on the location of the adsorbed molecule have been also investigated in [585] for a Ni atom adsorbed on the graphene surface. It was also found that at the zigzag edges the Ni atom forms more stable configuration than that in the middle of the ribbon.

A systematic first-principles study of metal atoms adsorbed on pristine graphene and graphene with a defect, such as a single vacancy (SV) or a double vacancy (DV), was reported in [586]. For metal atoms adsorbed on pristine graphene, the binding energy is 0.2–1.5 eV and the barrier for migration of the metals along the surface is in the range of 0.2–0.8 eV. Therefore at room temperature, the adsorbed atom would rather migrate along the graphene surface and the magnetic moment induced by the adsorption would be unstable, making it difficult to use adsorption for manufacturing a graphene-based Kondo system. The introduction of a vacancy in the graphene lattice significantly improves the metal adsorption, changing the binding energy up to ~ -7 eV, which would prevent the adsorbed atom from moving away from the vacancy. The calculated results of the magnetic moment and the binding energy of a metal atom adsorbed on graphene containing single and double vacancies are presented in Figure 118. For most metals, the bonding with the graphene surface is strong thereby creating a hybridized state. This induces a small dispersion into the

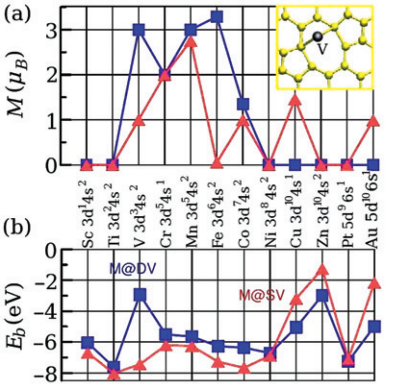

Figure 118. (a) The magnetic moment of the graphene sheet with the adsorbed metal atoms and (b) the binding energies of the metals. For both cases, squares corresponds to the case of graphene containing a single vacancy (SV), white triangle – to a double vacancy (DV). The M@SV and M@DV denote the metal-graphene system with SV and DV, respectively (Reprinted figure with permission from A.V. Krasheninnikov *et al.*, Physical Review Letters, 102, 126807, 2009 [586]. Copyright © (2009) by the American Physical Society.).

bands, which appears close to the Fermi energy and below. The M@DV complexes (metal–graphene system with the double vacancy) are found to be magnetic for all transition metals from V to Co. The larger 'hole' created by a double vacancy was suggested to cause the weaker interaction of the impurity atom with the ligand bonds leading to the higher spin state. In [587] it was also shown that adsorption of metals and small metallic structures can initiate the formation of mono- and bivacancies in the graphene lattice, thereby changing its electronic structure. The formation energy for these vacancies are found to be reduced due to the presence of the transition metal impurities, while a gold impurity almost did not affect the characteristics of the vacancies.

The effect of interaction of the adsorbed metal ions with the zigzag edges terminated by fluorine has been used in [588] to control the migration of the Li ions along the graphene surface. It was shown that at room temperature (~300 K) Li ions would migrate along the graphene surface without approaching the edges because of the repulsive interaction with the positive charge of the C–F carbon bond, whereas at higher temperature the Li ion can move freely near the edge region. The possibility to control the magnetic moment of the graphene with adsorbed metal atoms by the electric field has been discussed in [589]. There it was shown that an applied electric field can induce a shift of the chemical potential, thereby moving the magnetic field created by the adsorbates in the vertical direction.

8.3. *Lattice defects*

The interest in defects in the graphene lattice as a source of magnetization was triggered by an experimental work [590] where proton irradiation with energy 2.25 MeV was found to induce magnetism in highly oriented pyrolytic graphite

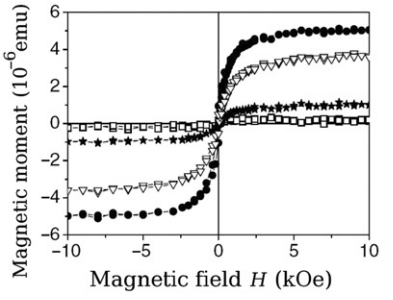

Figure 119. The magnetic moment of the pyrolytic graphite after first irradiation step (□), second (∗), third (●) and fourth (▽) (Reprinted figure with permission from P. Esquinazi *et al.*, Physical Review Letters, 91, 227201, 2003 [590]. Copyright © (2003) by the American Physical Society.).

samples. The magnetic moment of the pyrolytic graphite on a Si substrate has been measured, and the results obtained after subtraction of the substrate contribution are displayed in Figure 119. Because irradiation has been performed in several steps, a clear increase of the magnetic moment within the ferromagnetic loop with each step of the irradiation was observed (Figure 119). The authors came to the conclusion that the appearance of the magnetism after proton irradiation is related to magnetic ordering which is stable at room temperature, and not to the contribution from magnetic impurities. In another experiment [591], the electron-beam irradiation resulted in the appearance of a strong disorder band in the Raman spectrum of the single graphene layer. This was attributed to the damage to the graphene lattice caused by the radiation. Room-temperature ferromagnetism of graphene sheets has also been obtained [592]. There, the magnetization is believed to be induced by defects generated in the annealing process, because for samples of graphene oxide with induced magnetic impurities no ferromagnetism has been observed. An increase of the annealing temperature for some samples caused the enhancement of magnetization. The influence of the sample preparation on the presence of the charged impurities even if no doping has been applied has been noticed in [593], where the impurity concentration has been defined from the shift of the *G*-peak in the Raman spectra. It was shown that irradiation can also influence the charge transfer characteristics [565], which is proposed to be the result of a decrease in the Fermi velocity and modification of the hopping integral after irradiation.

The experimentally achieved ferro- or ferrimagnetism in graphite (explained by generation of defects in the graphite lattice) has stimulated an extensive investigation of the influence of defects on the magnetic properties of graphene. In [594,595], several mechanisms explaining the appearance of magnetism in carbon systems were proposed: under-coordinated atoms, itinerant ferromagnetism and negatively curved sp^2 bonded nano regions in the carbon lattice. However, defects are considered to be the most likely cause of magnetism. There are several types of defects responsible for the magnetic phenomena, vacancies and atoms on the graphene edges possessing dangling bonds (either passivated or free). The localized electronic states induced by these defects contribute to the density of states at the Fermi level and can induce magnetism.

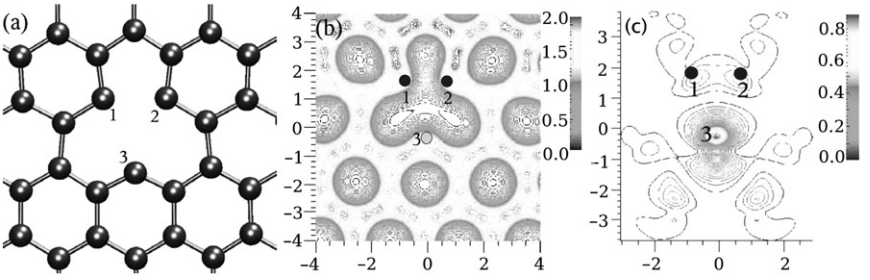

Figure 120. (a) Atomic structure of a single vacancy in graphene, which undergoes a Jahn–Teller distortion. The weak covalent C–C bond of length 2.02 Å is formed between atoms 1 and 2. (b) the charge density distribution ($e\,Å^{-3}$). (c) the spin density distribution ($e\,Å^{-3}$) (Reprinted with permission from Y. Ma *et al.*, New Journal of Physics, 6, p. 68, 2004 [595]. Copyright © (2004) IOP Publishing Ltd.).

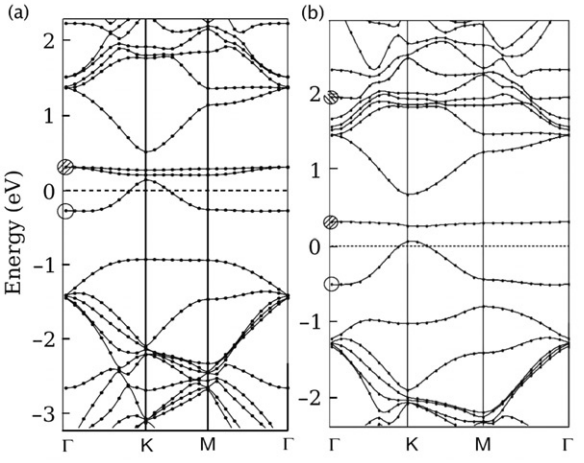

Figure 121. The band structure of graphene containing single vacancy of different symmetries: (a) the vacancy having the D_{3h} symmetry of the honeycomb network, (b) the vacancy of C_s symmetry. The band structures are obtained with DFT-LDA calculations. The Fermi level is set to zero. The shaded circles denote the σ band, while open circles correspond to the π band (Reprinted figure with permission from H. Amara *et al.*, Physical Review B, 76, 115423, 2007 [597]. Copyright © (2007) by the American Physical Society).

8.3.1. *Vacancy defects*

Spin-polarized calculations of the electronic structure were applied to investigate the effect of a single vacancy on the electronic properties of graphene [594,595]. The atomic structure of a single vacancy, its charge and spin density are presented in Figure 120. The carbon atoms surrounding the vacancy have sp^2 dangling bonds, but the formation of a pentagon leads to the saturation of two of these bonds, while the remaining unsaturated dangling bond will induce a magnetic moment of $1.04\,\mu_B$. However, the energy difference between a spin-polarized state and a non-polarized state was found to be only about 0.1 eV, suggesting an instability of magnetism of a single carbon vacancy which can be destroyed by interlayer interactions or finite

temperature. However, it was also shown that the single vacancy defect can have two conformations: the vacancy having the D_{3h} symmetry of the honeycomb network and the vacancy of C_s symmetry which undergoes a Jahn–Teller distortion [596,597]. In the case of the vacancy of C_s symmetry, the positions of the carbon atoms are distorted, namely two atoms near the vacancy move closer to each other and the third atom is displaced out of plane [597], and the presence of such vacancies significantly affects the electronic properties. The band structures of a graphene sheet containing the D_{3h} or C_s vacancies are presented in Figure 121. First of all, the presence of a vacancy and the magnetic ordering of the states localized on the vacancy break the symmetry of the graphene π-orbital system, which leads to opening of a gap. The gap between the π bands is larger for the vacancy with C_s symmetry than that with higher D_{3h} symmetry. Second, the vacancies induce extra bands near the Fermi level, which are flat σ bands associated with the defect states localized on the carbon atoms around the vacancy. For the vacancy of D_{3h} symmetry, there are two symmetric σ bands which are slightly separated and one antisymmetric π band (Figure 121a). For the vacancy of C_s symmetry, the π bands are shifted upward with respect to the position of the Fermi level and, because of broken planar symmetry, one σ band is moved deeper into the valence band. The study of a single vacancy with molecular dynamics methods [598] has shown that an electron trapped at the vacancy is stable at low temperature, while increasing the temperature up to 300 K leads to the structural changes of the graphene lattice that can allow the trapped electron to escape.

Therefore, even a single vacancy can induce magnetization into the graphene system through the formation of the spin-polarized localized state [328,594,595,597–604]. However, the presence of several vacancies in the graphene lattice can completely change the magnetization phenomena due to the correlation of the positions of the vacancies [601,605–610]. The presence of a single vacancy breaks both the lattice and sublattice symmetries and opens a gap. Two identical vacancies on different sublattices can restore the sublattice symmetry, thus suppressing the gap [605]. However, two identical vacancies located on the same sublattice results in a larger band gap. Therefore, the sublattice imbalance induced by the distribution of the vacancies over an initially balanced graphene lattice defines the magnetic properties of graphene lattice with defects [474,606].

Considering the spin properties of the defects, it was established that the defects according to Lieb's theorem [471] can interact ferromagnetically or antiferromagnetically depending on the sublattice imbalance. As a result, the total spin of the system will be defined by these local magnetic interactions. It was also found that at a certain defect density, the local magnetization can disappear [606,607]. These results suggesting disappearance of magnetization are in good agreement with the experimental data, where the suppression of magnetization has been observed after four steps of irradiation [590] (Figure 119). In [608], the total magnetization was reduced not only by increasing the vacancy density but also by decreasing the distance between vacancies. The dependence of the magnetization on the distance between the vacancies is a result of the bonding and antibonding interaction of the defect states. Thus, for the vacancies located on different sublattices, the energy splitting decreases with increasing distance between the vacancies [609]. More extensive investigation of the density of vacancies and the sublattice imbalance has

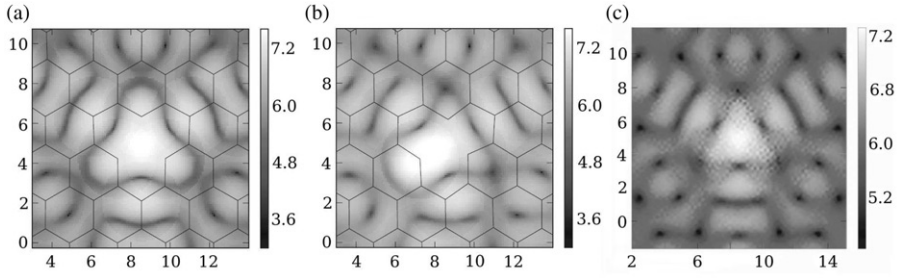

Figure 122. The scanning tunneling microscopy images of the single vacancy in graphene computed with positive tip potential of 0.2 V. (a) The non-reconstructed D_{3h} vacancy, (b) the reconstructed C_s vacancy, (c) average of the three equivalent C_s structure rotated by $\pm 2\pi/3$ (Reprinted figure with permission from H. Amara *et al.*, Physical Review B, 76, 115423, 2007 [597]. Copyright © (2007) by the American Physical Society.).

been performed in [609] with the help of a combination of the Hubbard model and first-principles methods. For vacancies which are equally distributed over the two sublattices, the magnetic moments on these sublattices are characterized by the opposite spin orientation and therefore they have magnetization of the opposite sign. This leads to a compensation effect in the total magnetization. It was concluded that a finite total magnetic moment can only be achieved in the case of the domination of the vacancies arranged on the same sublattice. In another study [601] the dependence of the gap on the concentration of uncompensated vacancies was reported. In the case when the electron–hole symmetry is preserved, the high dilution of the vacancies has been found to result in flattening of the DOS around the band center, while breaking of the electron–hole symmetry leads to broadening of the DOS peak at the Fermi level.

Lattice defects induce a significant alteration of the local electronic properties due to the scattering and interference of the electron waves at these defects. There are many experimental works devoted to the investigation of scanning tunnelling microscopy (STM) images of the defects as each type of defect is supposed to have its own signature [611–616]. For different types of defects the STM images have also been generated with first-principles methods [596,597,599,617]. The STM images of a single vacancy with different symmetries (D_{3h} and C_s) are presented in Figure 122. For a D_{3h} vacancy, the trigonal symmetry of the image at the center of the vacancy is observed, which is the result of the localization of the electron density at the three dangling bonds. The C_s vacancy is not characterized by the three-fold symmetry. The rotation of the pentagon by $\pm 2\pi/3$ for a C_s vacancy was found to restore the trigonal symmetry of the graphene lattice.

8.3.2. *Vacancy defects saturated by hydrogen*

The single vacancy is also interesting for understanding how it interacts with the adsorbed molecules. The interaction of helium atoms with a single vacancy induces a magnetic moment of about μ_B per vacancy, while interaction with an ideal graphite lattice was found to be weak, demonstrating no magnetic signal [594]. A similar situation is obtained for the interaction of adsorbed hydrogen with a single vacancy.

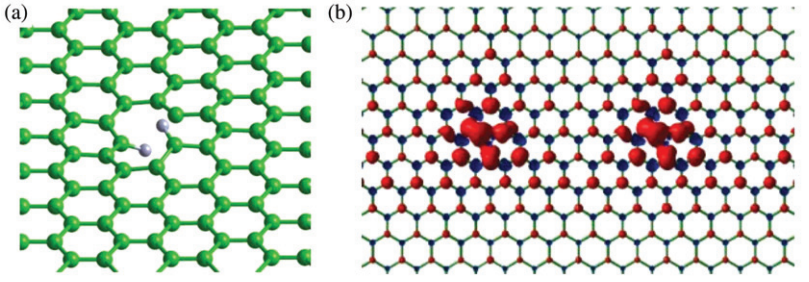

Figure 123. (a) The graphene sheet with the vacancy defect saturated by hydrogen atoms above and below the graphene plane. (b) The spin density distribution for the graphene sheet containing two identical vacancy defects saturated by hydrogens which are placed at a distance of 20 Å (Reprinted figure with permission from L. Pisani *et al*., New Journal of Physics, 10, p. 033002, 2008 [618]. Copyright © (2008) IOP Publishing Ltd).

However, if one dangling bond of the vacancy is saturated by hydrogen, that leads to a metastable state, and a magnetic moment of $2.3\,\mu_B$ is obtained. There is another stable magnetic configuration for a single vacancy saturated by hydrogens: if a single hydrogen atom interacts with a vacancy which is already saturated by another hydrogen, the stable configuration with two hydrogen atoms placed above and below of the graphene sheet is formed (Figure 123a). The magnetic moment of this configuration was found to be $1.2\,\mu_B$ in [594] and about $2.0\,\mu_B$ in [618]. There are two unpaired electrons on this defect [618], one of them occurs due to the breaking of the σ bond, whereas the other electron is the result of breaking of the three π bonds between the vacancy and the neighboring carbon atoms, which leads to the appearance of 1/3 of an unpaired electron on each atom. Because the three carbon atoms neighboring a vacancy belong to one sublattice, these unpaired electrons have the same spin orientation, therefore producing a spin-polarized electron localization, as shown in Figure 123(b). In the case of two vacancies embedded into a graphene sheet, the magnetic moment of the system will increase if the defects appear on the same sublattice as a result of the ferromagnetic coupling between their localized spin moments. Therefore, coupling between the defects possesses magnetic ordering at high temperature. The presence of these defects in the graphene lattice has also been found to break the sublattice symmetry thereby opening a gap of 0.51 eV for the majority spin band and of 0.55 eV for the minority. The calculated energy bands for the majority and minority spin states are presented in Figure 124 for two defects separated by distance L of 20 Å. It was also found that the opening of the gap is not related to the spin–orbit coupling and the gap size was shown to change with increasing distance between defects according to the scale L^{-2}.

8.3.3. *Divacancy defects*

The divacancy defect [597], which is formed when two neighboring vacancies coalesce, significantly changes the electronic and magnetic properties of the graphene flake. There are π bands which are located around the Fermi level, while σ bands induced by the vacancies are not located near the Fermi level but move deeper into the conduction and valence bands. The transition from the spin degenerate case of

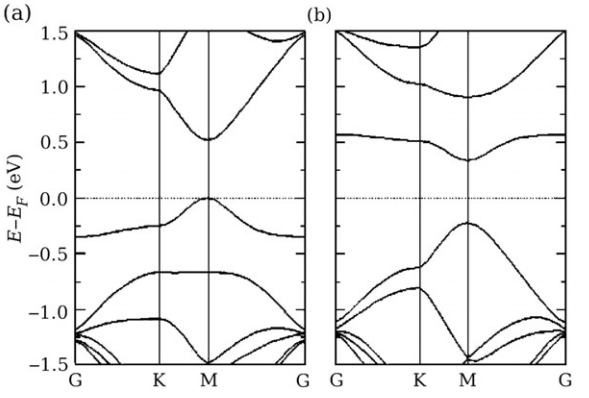

Figure 124. The band diagram for (a) majority and (b) minority spin states of the ferromagnetic state in graphene containing two vacancy defects saturated by hydrogens and separated by 20 Å (Reprinted figure with permission from L. Pisani *et al.*, New Journal of Physics, 10, p. 033002, 2008 [618]. Copyright © (2008) IOP Publishing Ltd).

pure graphene to highly spin-polarized state has been found in [619] due to the presence of a divacancy defect. In [620] the transition of graphene with armchair edges from a semiconductor to a metal was predicted to occur due to the presence of divacancies distributed over the graphene lattice with a constant period. Moreover, the presence of a divacancy defect was found to lead to strong interaction between graphene and the adsorbed molecules [621]. Thus, the adsorption of CO and N_2 molecules on graphene containing a divacancy defect led to a metallic behavior. Moreover, the adsorbed molecules were found to dissociate in the vicinity of a divacancy defect and take the place of the missing carbon atoms. For example, N_2 molecules play the role of a substitutional impurity for the missing carbon atom in graphene. The adsorption of a gold atom on the graphene sheet containing vacancy defects leads to the in-plane bonding of the gold atom [622]. The diffusion barrier for a gold atom on the graphene surface was found to decrease with increasing size of the vacancy. In addition to the divacancy, other type of vacancies with several carbon atoms missing have been investigated elsewhere [602,606,620,623] and spin-polarized states have also been generated from them. Jeong *et al.* [624] have seen the stabilization of some defects in the presence of pentagon and three pentagon vacancies.

8.3.4. *Crystallographic and chemisorption defects*

Attention has also been paid to crystallographic defects [605,625]. For a semiconducting graphene nanoribbon, the Stone–Wales defects have been found to induce a defect band at 0.6 eV above the Fermi level [625]. It was shown that adsorption of a COOH group is capable of significantly shifting this defect band closer to the Fermi level [625]. An increase in the number of Stone–Wales defects with adsorbed COOH groups can lead to the transition of the graphene sample from a semiconductor to a *p*-type metal. For metallic graphene, the presence of a single Stone–Wales defect shifts the Dirac point maintaining the two-fold degeneracy, but removing the

degeneracy at the K point, which results in a gap of 27.8 meV, while for three defects a gap is 80.3 meV [605]. Therefore for low density of the Stone–Wales defects, the size of the gap increases almost linearly with increasing defect concentration. The dynamic stability of the Stone–Wales defects has been found to be rather low in a planar graphene sheet [626], while similar crystallographic defects, such as pentagon–heptagon pairs, were dynamically stable. Random arrangement of the crystallographic defects, which are shown to form linearly stable configurations, has been seen to provide the formation of meta-crystal structure of graphene [627].

Chemisorption defects on the graphene surface, such as a carbon adatom or a hydrogen adatom, have been studied in [594,597,599,628]. The presence of vacancy defects has already been mentioned to initiate the formation of the chemisorption defects due to the attraction of the adatoms by vacancy defects [627]. It was found in [599] that hydrogen chemisorption defects induce a magnetic moment of μ_B per defect, and defect bands. The band maximum for the majority spin is located below the Fermi level, while in the minority spin case, it is above the Fermi level. The magnetic moment of the hydrogen chemisorption defects is independent of the distance between the two defects and the system remains spin-polarized in a wide range of defect concentration. However, the magnetic moment of the system depends on the distribution of the defects over the graphene sublattices where ferromagnetic coupling between defects give rise to an increase in the magnetic moment. Thus, the ferromagnetic ordering of the defects occurs when two defects are localized on the same sublattice as a result of non-oscillating behavior of the magnetization of the p_z orbital of the carbon atom and indirect coupling between defects.

In [603], the magnetic moment induced by the presence of an adatom, such as C, B, N, is found to be independent of the defect concentration, while the alteration of the band gap has been indicated. Moreover in the same work, the defects such as substitutional atoms and vacancy defects have been found to break symmetry of the graphene lattice and induce the magnetic quasi-localized states for which the magnetic moment is defined by the density of defects. For a carbon adatom incorporated into the graphene sheet [597], the flat bands of the localized states occur in the vicinity of the defect, which is similar to that obtained for the single vacancy defect (Figure 121a). The saturation of the carbon adatom by hydrogen [594] induces a magnetic moment of $0.9\,\mu_B$ resulting from the C–H group. The conductance of graphene has been found to be modified by the presence of the carbon adatom [628], for example, the conductance dip was dependent on the location of the defect relative to the edges and the severity of the defect. In general, the conductance of graphene is found to decrease in the presence of defects [628,629]. Moreover, the presence of a defect is found to affect the transport length scale in graphene [630], which is shown to fluctuate significantly as the topology of the edge irregularities are changed.

8.3.5. *Substitutional doping of graphene*

Another interesting topic is doping of graphene by impurities. It was observed experimentally that graphene is converted from *p*-type (pristine graphene) to *n*-type by substitutional doping of N atoms [631]. The investigation of doped graphene with first-principles methods [632] has also shown a transition of the armchair

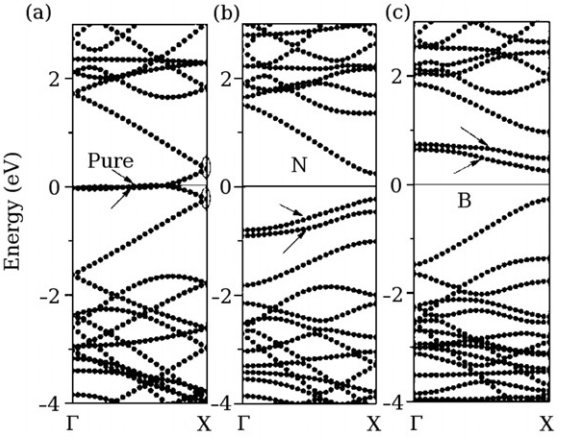

Figure 125. (a) The band diagram of pure graphene. (b) The band diagram of graphene doped by N. (c) The band diagram of graphene doped by B (Reprinted with permission from B. Huang *et al*., Applied Physics Letters, 91, 253122, 2007 [632]. Copyright © (2007) American Institute of Physics.).

nanoribbon from metallic to semiconducting behavior due to doping. The degradation of the electronic properties with doping is shown in Figure 125. Pristine graphene was observed to be metallic, whereas the substitutional doping by either N atoms or B atoms opens a gap. The substitution of a carbon atom by N (N-doping), induces a impurity level below the Fermi level (*p*-type semiconductor), while B-doping induces a impurity level above the Fermi energy, thereby leading to *n*-type semiconductor behavior of graphene in addition to the opening of a gap. The band gap is also modulated by the doping concentration. For low doping concentration, the band gap increases as the concentration of dopants grows, then achieves a maximum at concentration of $0.1365\,\text{Å}^{-1}$ and starts to decrease with further increase of the doping. Substitutional doping is found to be energetically more favorable at the interfaces of the zigzag edges.

A transition of graphene from metallic to semiconducting type has been found elsewhere [633] as result of substitutional N-doping. There, by controlling a chemical composition of C_xN_y graphene, the band gap was modulated in the range of 3–5 eV. The C_xN_y graphene layers were created under the conditions that chemical valences of four for C atoms and of three for N atoms were satisfied. This was achieved by generating a single vacancy of a C atom in a periodic manner. The optimization process has shown that some of the conformations were stable and had no confining compressional stress, but some conformations were found to spontaneously adopt buckled geometries. In the case when the carbon atom is substituted by a B atom, the transformation of graphene to the metallic type has also been reported [634]. Moreover, substitution of carbon atoms by B or N atoms was found to change the magnetism of the graphene nanoribbon [635]. There, the magnetic phase of graphene, i.e. the spin alignment between two opposite zigzag edges, has been controlled by the charge injection. The switching of the antiparallel spin orientation of the localized states between zigzag edges to the parallel one thereby modifying the size of gap was obtained. The presence of an impurity band induced by the

substitutional doping has also been observed in [601]. There, the impurity band had a split structure and was completely detached from the main band. For small impurity concentration, the change of the electronic structure consists of a rigid shift of the Dirac point. In the case when the impurities are located close to each other, the interference and hybridization effects leading to re-splitting of the low-energy resonance were observed.

The occurrence of an impurity-induced resonance near the Dirac point was observed in the local density of states as a result of the substitutional doping of two carbon atoms in graphene [636]. The existence of two nonequivalent Dirac points in the Brillouin zone has been proposed to cause this resonance effect. The embedding of the magnetic impurity into graphene has been shown to result in exchange splitting of the resonance in the two spin channels. The contribution of the exchange scattering is found to enhance the polarization of the impurity state. Moreover, the role of the substitutional impurity on the transport properties of graphene has been considered in [637]. The presence of impurities such as B or N was found to result in resonant backscattering, the efficiency of which was strongly dependent on the symmetry of the graphene sample, the edges and the location of the impurities within the graphene lattice. The possibility to convert the armchair nanoribbon in the semiconducting state to a metal by embedding a boron cluster was discussed in [638,639]. Another interesting result was reported in [640], where a method of substitutional doping of the graphene sheet by a B atom without an activation barrier was proposed. The barrierless doping was obtained due to selective exposing of each side of graphene sheet to different elements, such as nitrogen and boron.

8.4. *Functionalization of the edges*

The edges play a crucial role in the establishment of the electronic properties of nanoscale graphene. For example, structural changes of the edges [404,641,642], such as bond reconstruction, edge passivation and even edge aromaticity often lead to a change of the π network composition at the edges (percentage of sp, sp^2 and sp^3 bonds [428]), thereby modifying the electronic properties of graphene. In [641] the change of the electronic structure of a graphene nanoribbon activated by the edge modification as a function of the hydrogen content of the environment was investigated with first-principles methods. The simulations were performed for zigzag and armchair edges of stable and unstable configurations, the structures and electronic properties of which are presented in Figure 126(a) and (b), respectively. The results show that alteration of the edges changes the band structure by shifting the band crossing along the k-axis and along the energy axis or by modifying the size of the band gap. Therefore, the main conclusion here is that edge reorganization is a prospective way of manipulating the electronic properties of graphene (including size of the band gap) due to the significant contribution of the edges into the electronic properties of graphene. The edge structure can also be changed by saturation of the dangling bonds at the edges through its bonding with chemical groups (edge functionalization [643]) which may be another way to obtain the desired properties, such as spin polarization, spin gap asymmetry and controllable size of the band gap. There are two ways to functionalize graphene which have been extensively

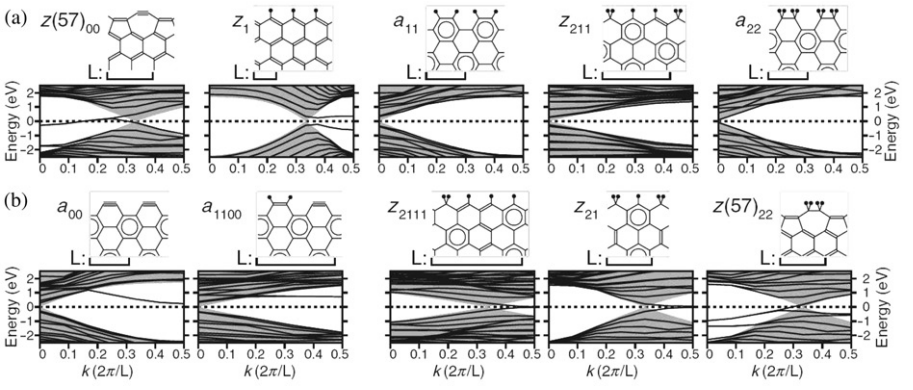

Figure 126. The configuration of zigzag (*z*) and armchair (*a*) edges of graphene and the corresponding band structure. The filled circles are hydrogen atoms. The structures are periodic along the edge with periodicity *L*. The gray area shows the bands allowed in 'bulk' graphene. (a) Most stable edge configuration, (b) other stable edge modifications. Here *z* denotes the zigzag edges, while *a* denotes the armchair edge (Reprinted figure with permission from T. Wassmann *et al*., Physical Review Letters, 101, 096402, 2008 [641]. Copyright © (2008) by the American Physical Society).

investigated – identical modification of two opposite edges or modification of a single edge. Because the zigzag edges are known to possess localized states, they have attracted considerable attention from the researchers. A wide range of chemical groups have been used for functionalizing the graphene edges: from simple chemical groups, such as NH_2, NO_2, O to massive molecules such as short branched alkanes [644]. Below, we consider the influence of the edge functionalization by different chemical groups on the electronic properties of graphene.

The lowest energy state of a graphene nanoribbon is known to have opposite spin ordering between the zigzag edges [362,412,414–416], i.e. when a spin-up state is localized on one sublattice, and a spin-down state is localized on the other, thereby opening a gap. The energetic bands of this state are most often spin degenerate, but can be slightly non-degenerate providing similar band structures for both spin states where the spin gap symmetry is preserved. A similar picture is observed when the two opposite zigzag edges are identically functionalized by the same groups [645–648]. Thus, for edges terminated with hydrogen or hydroxyl groups, the system is spin polarized in equilibrium and doubly degenerate [645], while using OH or NH functional groups gives a spin-unpolarized system. Almost degenerate spin states are found for graphene with zigzag edges terminated by NH_2 groups at each second carbon atom [646]. Moreover, by changing the type of the functional groups the size of a gap, spin ordering along the zigzag edges and distribution of the molecular orbitals over the graphene structure can be manipulated [648]. The simulation of the size of the band gap when both zigzag edges are functionalized by the same chemical groups are presented in Figure 127. According to the presented data, the oxidation of the graphene edges can decrease the band gap to almost half that of mono-hydrogenated zigzag edges. However, functionalization of both zigzag edges does not lift the degeneracy.

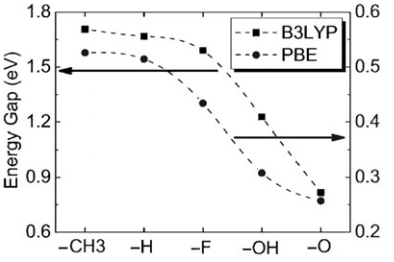

Figure 127. The band gap of the nanoscale graphene with the zigzag edges functionalized by the same chemical groups. The simulations are performed with PBE and B3LYP functionals (Reprinted figure with permission from H. Zheng and W. Duley, Physical Review B, 78, 045421, 2008 [648]. Copyright © (2008) by the American Physical Society.).

Modification of opposite zigzag edges by different chemical groups, which stabilizes a state with ferromagnetic ordering between the opposite edges, can induce an asymmetry in the potentials between these edges. This leads to an energy shift of the orbitals localized on the edges, thereby lifting the spin degeneracy of the electronic states localized on the opposite zigzag edges. Therefore, functionalization of a single zigzag edge is the way to generate a fully spin-polarized state in graphene, which can also be characterized by the spin gap asymmetry. For example, bearded ribbons where one zigzag edge is pure and has dangling bonds whereas the other edge has an additional carbon bond saturating each dangling bond have been found to have a gap [643]. But the most common case is when functionalization of the zigzag edge is performed by termination of the dangling bonds by some atoms which are not carbon. It was shown in [649] with first-principles methods that for graphene with one mono-hydrogenated zigzag edge and one di-hydrogenated edge, spontaneous magnetization occurs. The electronic structure of such a graphene system is fully spin-polarized and has a flat band near the Fermi level composed of the localized edge states. The flat band of the spin-up states is located below the Fermi level, while for the spin-down states it is just above the Fermi level. The achieved splitting between spin-up and spin-down states was 0.5–0.6 eV, while the gap was ~0.2 eV. The magnetic moment of such a structure was not zero and the total spin equaled one half of the number of unit cells. The functionalization of a single edge by fluorine atoms or oxygen atoms when a second edge is monohydrogenated has been considered in [650]. The band structures of fluorinated and oxidized graphene are similar to each other and distinguished by the presence of flat bands, which appear near the Fermi level and are spin-polarized only around the K point. However, the spin-up and spin-down states are slightly separated from each other in energy, thereby possessing a weak spin gap asymmetry.

The methylene-substituted graphene structure, where every carbon atom or every second carbon atom at a single zigzag edge is bound to a methylene group, did not show a strong magnetic behavior. Cervantes-Sodi *et al*. [646,647] considered different functional groups terminating the dangling bonds at a single zigzag edge to induce the spin-polarization in graphene. The simulation results of the spin density of the states performed with first-principles method are shown in Figure 128. There the edge functionalization significantly modifies the electronic structure of the graphene

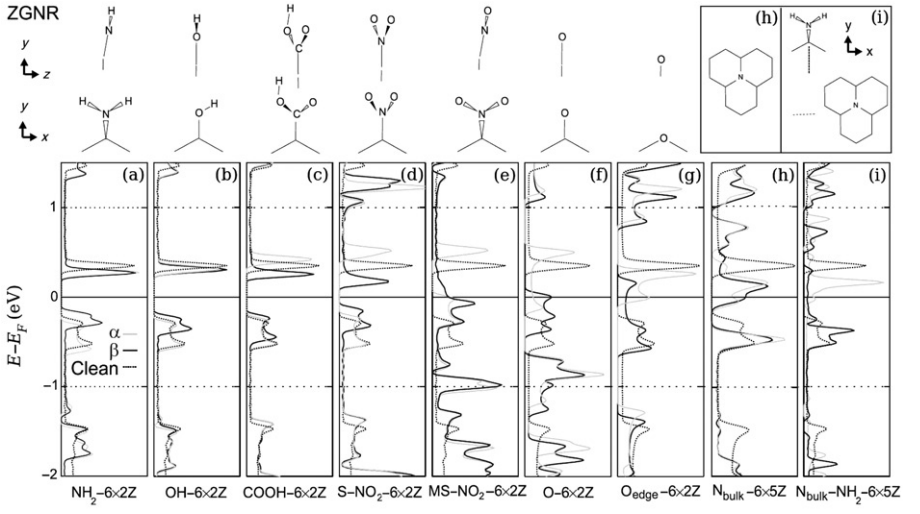

Figure 128. The spin density of the states for graphene with a single zigzag edge functionalized by the chemical groups. The spin density distribution for α- and β-spin states is presented in comparison to those for pure (clean) graphene (Reprinted figure with permission from F. Cervantes-Sodi *et al.*, Physical Review B, 77, 165427, 2008 [646]. Copyright © (2008) by the American Physical Society.).

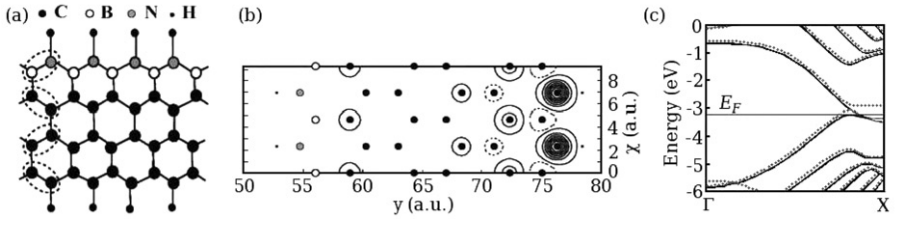

Figure 129. The structure and electronic properties of graphene where the border carbon atoms at one zigzag edge are substituted by the B or N atoms. (a) The structure of the graphene ribbon, (b) The spin-density distribution for the state where spin separation between sublattices does not occur. (c) The energy band structure for a ferrimagnetic state. Solid and dashed lines represent the spin-up and spin-down states (Reprinted figure with permission from J. Nakamura *et al.*, Physical Review B, 72, 205429, 2005 [415]. Copyright © (2005) by the American Physical Society.).

ribbon, particularly lifting the spin degeneracy. In some cases, a significant spin gap asymmetry is achieved producing half-metallic behavior at zero electric field (see the S–NO_2–$6 \times 2Z$ structure). However, functionalization of the armchair edges has been shown to slightly lift the spin degeneracy [646] and induce impurity bands. Similar results, showing that if two opposite zigzag edges are functionalized by two different types of chemical groups, a gap asymmetry of the α- and β-spin channels can be obtained, was also presented [418,651,652]. Thus, if one zigzag edge is terminated by OH groups and the opposite one by Cl atoms, zero band gap for one spin state and semiconductor gap for the other spin state are observed, thereby giving half-metallicity [651].

Another way to generate asymmetry of the potentials between two opposite zigzag edges is by substitution of the carbon atoms at the edges. Substitution of carbon atoms at a single zigzag edge by the B and N atoms [415], as presented in Figure 129(a), leads to occupation of the A and B sublattices by both spins, thereby providing the ferromagnetic spin ordering of the localized states between the zigzag edges and $n_\uparrow - n_\downarrow = 0.29$ per unit cell. The spin density distribution and band diagram for this state are presented in Figure 129(b) and (c), respectively. The spin ordering occurs due to the imbalance of the majority and minority spins at the zigzag edge, where substitution of the carbon atoms is performed. The obtained band structure corresponds to a metallic system. The lattice dissimilarity between the opposite zigzag edges generates asymmetry of the potentials between the opposite zigzag edges. The nanoribbons must be wider than a certain minimum value before spontaneous spin polarization may occur.

In [653], Berashevich and Chakraborty reported that for nanoscale graphene the highest symmetry is D_{2h} for which the sublattice symmetry is preserved and a gap can occur only due to the confinement effect. For the D_{2h} symmetry the HOMO and LUMO orbitals are localized at the zigzag edges but their electron density is equally distributed over both edges. Termination of a single zigzag edge by hydrogen or substitutional doping of the carbon atoms along a single zigzag edge by a dopant, such as nitrogen, breaks the sublattice symmetry thereby lowering the D_{2h} symmetry to the C_{2v} symmetry with a mirror plane of symmetry perpendicular to the zigzag edges. For the C_{2v} symmetry, the HOMO and LUMO orbitals are characterized by the α- and β-spin states localized on the opposite zigzag edges. For pure graphene in a state with the C_{2v} symmetry, where symmetry breaking is induced by the spin distribution between the zigzag edges, the band gaps for two different spins Δ_α and Δ_β are almost identical. Thus, for graphene with four carbon rings along the zigzag edge and five along the armchair edge, these band gaps are found to be of the order of $\sim$1.5 eV. The hydrogenation of a single zigzag edge leads to saturation of the dangling σ bonds at the terminated edge but does not significantly change the energy of the $HOMO_\alpha$ and $LUMO_\beta$ states localized at the terminated edge. The resulting non-degeneracy of the α- and β-spin states is not large, and the gap of the α-spin state ($\Delta_\alpha = 1.8$ eV) is almost identical to that of the β-spin state ($\Delta_\beta = 2.1$ eV). However, hydrogen termination along a single zigzag edge increases the gap from $\sim$1.5 eV for pure graphene in state of C_{2v} symmetry to $\sim$1.9 eV due to major breaking of the sublattice symmetry. The substitutional doping by nitrogen along a single zigzag edge shifts down the orbital energies of the $HOMO_\alpha$ and $LUMO_\beta$ states localized at the doped edge and results in a strong electron non-degeneracy for these orbitals. Slight enhancement of the gap occurs for the α-spin state up to $\Delta_\alpha = 2.2$ eV, but there is a significant decrease of the gap for the β-spin state down to $\Delta_\beta = 0.8$ eV. The achieved size of the band gap for α- and β-spin states corresponds to the half-semiconducting behavior. However, increasing the size of the graphene sample results in a decrease of both the Δ_α and Δ_β gaps due to diminishing confinement effect. When the number of carbon rings along the zigzag edges is six and seven along the armchair edges, the gap for the α-spin state is already suppressed to 1.13 eV while for the β-spin state it is 0.19 eV, which corresponds to the half-metallic behavior.

The state with ferromagnetic spin ordering between the zigzag edges when one edge is doped by boron was obtained in [448]. Metallic behavior for the majority spin channel and insulating behavior for the minority spin channel was observed in this case. An applied electric field was found to have no influence on this behavior, i.e. the magnitude of the gap remains the same for a wide range of the field strengths as a result of identical influence of the transverse electric field on both spin channels. In [654] it was shown that for substitution of one or several carbon atoms at the zigzag edges, the system becomes fully spin-polarized with a opening of band gap near the Fermi level, thereby switching from metallic to semiconducting behavior. The opposite was found in another case [646], where initially semiconducting graphene was converted to the metallic state by substitution of carbon atoms at both zigzag and armchair edges. Moreover, the substitution of the carbon atoms at a single zigzag edge by O (Figure 128g) and in the center of the ribbon by N (Figure 128h) has induced impurity states in the band gap of the zigzag nanoribbons, consequently providing the semiconductor-metal transition. Additionally, it was found [655] that the substitutional doping of a single carbon atom at the zigzag edge by an O, B or N atom can inject a hole or electron into graphene depending on the impurity type. Therefore, such substitution induces a localized impurity state close to the Fermi level. Because the induced impurity level affects the π/π^* levels of graphene, alteration of the transport properties of graphene occurs. For the armchair nanoribbon [646], the substitution of carbon atoms on the armchair edges by B and N was found to induce localized states which appear deep inside the valence and conduction bands. This actually could discourage manipulation of the electronic properties of the armchair nanoribbons.

In the system with a line of atomic substitutions in the middle of the graphene sheet, both metal–semiconductor and semiconductor–metal transitions have been observed [656]. The impurity line breaks the translation symmetry normal to the edges, and provides a modification of the electronic properties. For a zigzag nanoribbon, the impurity line induced along the armchair edges splits the graphene sheet into two stacked nanoribbons and therefore its electronic properties are significantly modified. If the graphene structure cannot be divided equally then the achieved electronic structure is a superposition of two bands of the nanoribbons of different sizes. For armchair nanoribbons a similar impurity line has been placed along the zigzag edge [656]. Depending on the nanoribbon geometry, there were three types of energy band structures: two semiconductor and one metallic. The single impurity line has been found to convert the semiconducting armchair nanoribbon to a metallic one and the metallic to semiconducting ribbon. Replacing the middle carbon chain by a boron-nitride, nanoribbon was also investigated [657]. It was found that depending on the number of replaced chains the properties of the graphene ribbon can be modified. The system with two chains replaced by a B–N system, shows a spin gap asymmetry, where one spin channel is semiconducting with a gap of 0.5 eV (whose size is similar to that of pure graphene), while the gap in the second spin channel is significantly reduced in comparison to the case of pure graphene. The replacement of four chains leads to the appearance of one conducting channel and an increase of the band gap for the second spin channel, whereas replacement of six chains shows a decrease in the gap for both spin channels. However, such a replacement breaks the particle symmetry, thus mixing spin states

along the edges and therefore the whole lattice is characterized by no dominance of spin states at any sites.

As we have shown above, the main advantage of functionalization of the edges of a graphene ribbon is the possibility to achieve a half-metallic behavior of graphene without applying an external electric field. This has enormous potential for application in developing spin-selective devices based on graphene systems [48,450,453–464].

Acknowledgements

This work was supported by the Canada Research Chairs program and the NSERC Discovery Grant, both awarded to T. Chakraborty. The work of K. Ziegler was supported by the Deutsche Forschungsgemeinschaft. T. Chakraborty would like to thank Dr. Xuefeng Wang for valuable discussions and help in preparing the section on plasmons in graphene. We thank Professor Peter Fulde for his support. We also thank Jean-Noel Fuchs, Mark Goerbig, Peter Maksym, Sergei Sharapov for reading the early version of the manuscript and offering valuable comments to improve the article. Finally, we wish to thank numereous colleagues who offered valuable suggestions based on the preprint version (abridged): arXiv:1003.0391, posted online.

Notes

1. Structures with up to 10 carbon layers are known as few-layer graphenes, while structures with 10–100 layers are known as thin graphite films [1].
2. The experimental study of very thin graphite is older than Geim and Novoselov's 'initial' discovery in 2004. For example, [19,20], both discuss the possible fabrication of graphene.
3. *Nanoculture – Implications of the New Technoscience*, edited by N. Katherine Hayles (Intellect Books, 2004)
4. This assumption does not adequately produce the band structure near the center of the Brillouin zone where the σ bands have the lowest energy. See, for example, [140] for the experimental evidence of the σ bands, and [13] for a description of the tight-binding σ bands in monolayer graphene. However, the low-energy and transport properties of bilayer graphene are determined by the π bands, so we limit ourselves only to their discussion.
5. Both mono- and bilayer graphene spontaneously form corrugations, or ripples, which are a significant mechanism for the stable formation of the two-dimensional crystal, and which may add to the disorder in the system (Section 5).
6. There is a certain confusion in the literature over the labelling of Landau levels in bilayer graphene since two common notations exist. In the two-band model, it is convenient to label using $\mathfrak{n} \in \{\ldots, -3, -2, 0, 1, +2, +3, \ldots\}$, while in the four-band model, the notation $n \in \{\ldots, -2, -1, -0, +0, +1, +2, \ldots\}$ is usually used. In this section we shall use the notations as defined in this endnote, so that $\mathfrak{n}$ refers to the 'two-band' labels, while n denotes 'four-band' labels.
7. The parameter β phenomenologically describes the small splitting between the $\mathfrak{n} = 0$ and $\mathfrak{n} = 1$ levels caused by effects like those parametrized by Δ and t'. The notation $\mathfrak{n}$ is defined in endnote 6.
8. As a result of the multiplication of the model Slater determinant wave function φ by the correlation factor F, the multiparticle state $F\varphi$ will most likely have projections on states outside of the bands, in particular on states with energies lower than the bottom of the valence band. This is clearly unphysical and has to be rectified by requiring that projections of $F\varphi$ on the states with momenta larger than a cut-off momentum, must

vanish. This cut-off momentum is determined, for example by requiring it to yield the correct number of allowed valence band states. Another constraint which is perhaps necessary is to impose explicitly the normalization of $g(r)$, i.e.

$$\int \mathrm{d}r[\,g(r) - 1] = -1$$

(P. Pietiläinen, private communication).

9. The spin–orbit coupling strength in graphene can be small [249]. However, the results presented in this section are valid for similar gap size in the energy band.
10. For $|\mu| \gg |\omega|$ the expression in Equation (71) is linear in μ. However, the conductivity vanishes when we take the DC limit at fixed scattering rate.
11. The SCBA has been criticized by several authors as being not applicable to Dirac fermions [311,312,319,320]. This is based on the fact that certain terms of the perturbative series are neglected in the SCBA. The above analysis sheds a different light on this issue, namely that the SCBA is only the result of a special scalar form of the solution of the more general matrix saddle-point equation. This implies that the average one-particle Green's function, including the density of states, requires the full solution of the matrix equation (81). On the other hand, for the scattering rate η the scalar equation (80) (i.e. the SCBA) is justified as a reasonable approximation even for Dirac fermions.

References

[1] A.K. Geim and K.S. Novoselov, Nat. Mater. 6 (2007), p. 183.
[2] M.J. Allen, V.C. Tung, and R.B. Kaner, Chem. Rev. 110 (2010), p. 132.
[3] T. Ando, Physica E 40 (2007), p. 213.
[4] V.P. Gusynin, S.G. Sharapov, and J.P. Carbotte, Int. J. Mod. Phys. B 21 (2007), p. 4611.
[5] N.M.R. Peres, J. Physica Condens. Matter 21 (2009), p. 323201.
[6] Eur. Phys. J. Spec. Top. 148 (2007), pp. 1–181; Solid State Commun. 143 (2007), pp. 1–125; Solid State Commun. 149 (2009), pp. 1039–1160.
[7] A.K. Geim and A.H. MacDonald, Phys. Today 60 (2007), p. 35; A.K. Geim and P. Kim, Sci. Am. 298 (2008), p. 90.
[8] T. Chakraborty, *Quantum Dots*, Elsevier, Amsterdam, 1999.
[9] T. Chakraborty, Comments Condens. Matter Phys. 16 (1992), p. 35.
[10] P.R. Wallace, Phys. Rev. 71 (1947), p. 622; J.C. Slonczewski and P.R. Weiss, Phys. Rev. 109 (1958), p. 272.
[11] J.W. McClure, Phys. Rev. 104 (1956), p. 666.
[12] R.R. Haering and P.R. Wallace, J. Phys. Chem. Solids 3 (1957), p. 253; H. Sato, J. Phys. Soc. Japan 14 (1959), p. 609.
[13] R. Saito, G. Dresselhaus, and M.S. Dresselhaus, *Physical Properties of Carbon Nanotubes*, Imperial College Press, London, 1998.
[14] S. Reich, C. Thomsen, and J. Maultzsch, *Carbon Nanotubes*, Wiley-VCH, Weinheim, 2004.
[15] T. Ando, in *Nano-Physics and Bio-Electronics: A New Odyssey*, Chap. 1, T. Chakraborty, F. Peeters, and U. Sivan, eds., Elsevier, Amsterdam, 2002.
[16] T. Ando, T. Nakanishi, and R. Saito, J. Phys. Soc. Japan 67 (1998), p. 2857.
[17] K.S. Novoselov, A.K. Geim, S.V. Morozov, D. Jiang, M.I. Katsnelson, I.V. Grigorieva, S.V. Dubonos, and A.A. Firsov, Nature 438 (2005), pp. 197–200.
[18] A. Grüneis, C. Attaccalite, A. Rubio, D.V. Vyalikh, S.L. Molodtsov, J. Fink, R. Follath, W. Eberhardt, B. Büchner, and T. Pichler, Phys. Rev. B 80 (2009), p. 075431.
[19] X. Lu, M. Yu, H. Huang, and R.S. Ruoff, Nanotechnology 10 (1999), p. 269.

[20] R.B. Little, J. Cluster Sci. 14 (2003), p. 135.
[21] K.S. Novoselov, A.K. Geim, S.V. Morozov, D. Jiang, Y. Zhang, S.V. Dubonos, I.V. Grigorieva, and A.A. Firosov, Science 306 (2004), p. 666.
[22] K.S. Novoselov, D. Jiang, F. Schedin, T.J. Booth, V.V. Khotkevich, S.V. Morozov, and A.K. Geim, PNAS 102 (2005), p. 10451.
[23] A.C. Ferrari, J.C. Meyer, V. Scardaci, C. Casiraghi, M. Lazzeri, F. Mauri, S. Piscanec, D. Jiang, K.S. Novoselov, S. Roth, and A.K. Geim, Phys. Rev. Lett. 97 (2006), p. 187401.
[24] J.C. Meyer, A.K. Geim, M.I. Katsnelson, K.S. Novoselov, T.J. Booth, and S. Roth, Nature 446 (2007), p. 60.
[25] K.I. Bolotin, K.J. Sikes, Z. Jiang, M. Klima, G. Fudenberg, J. Hone, P. Kim, and H.L. Stormer, Sol. State Commun. 146 (2008), p. 351.
[26] X. Du, I. Skachko, A. Barker, and E.Y. Andrei, Nat. Nanotechnol. 3 (2008), p. 491.
[27] S.V. Morozov, K.S. Novoselov, M.I. Katsnelson, F. Schedin, D.C. Elias, J.A. Jaszczak, and A.K. Geim, Phys. Rev. Lett. 100 (2008), p. 016602.
[28] C. Berger, Z. Song, T. Li, X. Li, A.Y. Ogbazghi, R. Feng, Z. Dai, A.N. Marchenkov, E.H. Conrad, P.N. First, and W.A. de Heer, J. Phys. Chem. B 108 (2004), p. 19912.
[29] C. Berger, Z. Song, X. Li, X. Wu, N. Brown, C. Naud, D. Mayou, T. Li, J. Hass, A.N. Marchenkov, E.H. Conrad, P.N. First, and W.A. de Heer, Science 312 (2006), p. 397.
[30] J. Hass, W.A. de Heer, and E.H. Conrad, J. Phys.: Condens. Matter 20 (2008), p. 323202.
[31] W.A. de Heer, C. Berger, X. Wu, P.N. First, E.H. Conrad, X. Li, T. Li, M. Sprinkle, J. Hass, M.L. Sadowski, M. Potemski, and G. Martinez, Solid State Commun. 143 (2007), p. 92.
[32] F. Varchon, R. Feng, J. Hass, X. Li, B. Ngoc Nguyen, C. Naud, P. Mallet, J.-Y. Veuillen, C. Berger, E.H. Conrad, and L. Magaud, Phys. Rev. Lett. 99 (2007), p. 126805.
[33] Th. Seyller, A. Bostwick, K.V. Emtsev, K. Horn, L. Ley, J.L. McChesney, T. Ohta, J.D. Riley, E. Rotenberg, and F. Speck, Phys. Status Solidi b 245 (2008), p. 1436.
[34] M.L. Sadowski, G. Martinez, M. Potemski, C. Berger, and W.A. de Heer, Phys. Rev. Lett. 97 (2006), p. 266405.
[35] S.Y. Zhou, G.-H. Gweon, A.V. Fedorov, P.N. First, W.A. de Heer, D.-H. Lee, F. Guinea, A.H. Castro Neto, and A. Lanzara, Nat. Materi. 6 (2007), p. 770.
[36] A. Bostwick, T. Ohta, Th. Seyller, K. Horn, and E. Rotenberg, Nat. Phys. 3 (2007), p. 36.
[37] A.N. Obraztsov, E.A. Obraztsova, A.V. Tyurnina, and A.A. Zolotukhin, Carbon 45 (2007), p. 2017.
[38] A. Reina, X. Jia, J. Ho, D. Nezich, H. Son, V. Bulovic, M.S. Dresselhaus, and J. Kong, Nano Lett. 9 (2009), p. 30.
[39] K.S. Kim, Y. Zhao, H. Jang, S.Y. Lee, J.M. Kim, K.S. Kim, J.-H. Ahn, P. Kim, J.-Y. Choi, and B.H. Hong, Nature 457 (2009), p. 706.
[40] Q. Yu, J. Lian, S. Siriponglert, H. Li, Y.P. Chen, and S.-S. Pei, Appl. Phys. Lett. 93 (2008), p. 113103.
[41] J. Coraux, A.T. N'Diaye, C. Busse, and T. Michely, Nano Lett. 8 (2008), p. 565.
[42] X. Li, W. Cai, J. An, S. Kim, J. Nah, D. Yang, R. Piner, A. Velamakanni, I. Jung, E. Tutuc, S.K. Banerjee, L. Colombo, and R.S. Ruoff, Science 324 (2009), p. 1312.
[43] M.C. Lemme, Solid State Phenom. 156–158 (2010), pp. 499–509.
[44] Y.-M. Lin, K.A. Jenkins, A. Valdes-Farcia, J.P. Small, D.B. Farmer, and P. Avouris, Nano Lett. 9 (2009), p. 422.
[45] I. Meric, N. Baklitskaya, P. Kim, and K.L. Shepard, *Electron Devices Meeting*, 2008. (IEDM 2008), IEEE International, San Francisco, 2008.

[46] J.S. Moon, D. Curtis, M. Hu, D. Wong, C. McGuire, P.M. Campbell, G. Jernigan, J.L. Tedesco, B. VanMil, R. Myers-Ward, C. Eddy, and D.K. Gaskill, IEEE Electron Dev. Lett. 30 (2009), p. 650.
[47] C. Stampfer, E. Schurtenberger, F. Molitor, J. Güttinger, T. Ihn, and K. Ensslin, Nano Lett. 8 (2008), pp. 2378–2383.
[48] N. Tombros, C. Jozsa, M. Popinciuc, H.T. Jonkman, and B.J. van Wees, Nature 448 (2007), p. 571.
[49] F. Schedin, A.K. Geim, S.V. Morozov, E.W. Hill, P. Blake, M.I. Katsnelson, and K.S. Novoselov, Nat. Mater. 6 (2007), p. 652.
[50] J.S. Bunch, S.S. Verbridge, J.S. Alden, A.M. van der Zande, J.M. Parpia, H.G. Craighead, and P.L. McEuen, Nano Lett. 8 (2008), p. 2458.
[51] E. Stolyarova, D. Dtolyarov, K. Bolotin, S. Ryu, L. Liu, K.T. Rim, M. Kilma, M. Hybertsen, I. Pogorelsky, I. Pavlishin, K. Kusche, J. Hone, P. Kim, H. Stormer, V. Yakimenko, and G. Flynn, Nano Lett. 9 (2009), p. 332.
[52] B. Standley, W. Bao, H. Zhang, J. Bruck, and C.N. Lau, Marc Bockrath Nano Lett. 8 (2008), p. 3345.
[53] X. Wang, L. Zhi, and K. Müllen, Nano Lett. 8 (2008), p. 323.
[54] P. Blake, P.D. Brimicombe, R.R. Nair, T.J. Booth, D. Jiang, F. Schedin, L.A. Ponomarenko, S.V. Morozov, H.F. Gleeson, E.W. Hill, A.K. Geim, and K.S. Novoselov, Nano Lett. 8 (2008), p. 1704.
[55] M. Gibertini, A. Singha, V. Pellegrini, M. Polini, G. Vignale, A. Pinczuk, L.N. Pfeiffer, and K.W. West, Phys. Rev. B 79 (2009), p. 241406.
[56] B.A. Bernevig, T.L. Hughes, S.-C. Zhang, H.-D. Chen, and C. Wu, Int. J. Mod. Phys. B 20 (2006), p. 3257.
[57] J.H. Ho, Y.H. Lai, Y.H. Chiu, and M.F. Lin, Physica E 40 (2008), pp. 1722–1725.
[58] Y. Zheng and T. Ando, Phys. Rev. B 65 (2002), p. 245420.
[59] J. Alicea and M.P.A. Fisher, Phys. Rev. B 74 (2006), p. 075422.
[60] D.A. Abanin, P.A. Lee, and L.S. Levitov, Phys. Rev. Lett. 98 (2007), p. 156801.
[61] V. Lukose, R. Shankar, and G. Baskaran, Phys. Rev. Lett. 98 (2007), p. 116802.
[62] R.S. Deacon, K.-C. Chuang, R.J. Nicholas, K.S. Novoselov, and A.K. Geim, Phys. Rev. B 76 (2007), p. 081406(R).
[63] Z. Jiang, E.A. Henriksen, L.C. Tung, Y.-J. Wang, M.E. Schwartz, M.Y. Han, P. Kim, and H.L. Stormer, Phys. Rev. Lett. 98 (2007), p. 197403.
[64] D.L. Miller, K.D. Kubista, G.M. Rutter, M. Ruan, W.A. de Heer, P.N. First, and J.A. Stroscio, Science 324 (2009), pp. 924–927.
[65] G. Li, A. Luican, and E.Y. Andrei, Phys. Rev. Lett. 102 (2009), p. 176804.
[66] G. Li and E.Y. Andrei, Nat. Phys. 3 (2007), pp. 623–627.
[67] W. Kohn, Phys. Rev. 123 (1961), p. 1242.
[68] P. Plochocka, C. Faugeras, M. Orlita, M.L. Sadowski, G. Martinez, M. Potemski, M.O. Goerbig, J.-N. Fuchs, C. Berger, and W.A. de Heer, Phys. Rev. Lett. 100 (2008), p. 087401.
[69] C.P. Chang, C.L. Lu, F.L. Shyu, R.B. Chen, Y.K. Fang, and M.F. Lin, Carbon 42 (2004), p. 2975.
[70] T. Nakajima and H. Aoki, Physica E 40 (2008), p. 1354.
[71] I.A. Luk'yanchuk and A.M. Bratkovsky, Phys. Rev. Lett. 100 (2008), p. 176404.
[72] T. Chakraborty and P. Pietiläinen, *The Quantum Hall Effects*, 2nd ed., Springer, Heidelberg, New York, 1995.
[73] T. Chakraborty, Adv. Phys. 49 (2000), p. 959.
[74] V.P. Gusynin and S.G. Sharapov, Phys. Rev. Lett. 95 (2005), p. 146801.
[75] P.M. Ostrovsky, I.V. Gornyi, and A.D. Mirlin, Phys. Rev. B 77 (2008), p. 195430.
[76] H. Aoki and T. Ando, Solid State Commun. 38 (1981), p. 1079.

[77] R.E. Pringe, Phys. Rev. B 23 (1981), p. 4802.
[78] D.J. Thouless, J. Phys. C 14 (1981), p. 3475.
[79] D.J. Thouless and M. Kohmoto, Phys. Rev. Lett. 49 (1982), p. 41.
[80] V.P. Gusynin and S.G. Sharapov, Phys. Rev. B 73 (2006), p. 245411.
[81] N.M.R. Peres, F. Guinea, and A.H. Castro Neto, Phys. Rev. B 73 (2006), p. 125411.
[82] B. Dóra and P. Thalmeier, Phys. Rev. B 76 (2007), p. 035402.
[83] S. Masubuchi, K. Suga, M. Ono, K. Kindo, S. Takeyama, and T. Machida, J. Phys. Soc. Japan 77 (2008), p. 113707.
[84] K.S. Novoselov, Z. Jiang, Y. Zhang, S.V. Morozov, H.L. Stormer, U. Zeitler, J.C. Maan, G.S. Boebinger, P. Kim, and A.K. Geim, Science 315 (2007), p. 1379.
[85] Y. Zhang, Y.-W. Tan, H.L. Stormer, and P. Kim, Nature 438 (2005), pp. 201–204.
[86] X. Wu, Y. Hu, M. Ruan, N.K. Madiomanana, J. Hankinson, M. Sprinkle, C. Berger, and W.A. de Heer, Appl. Phys. Lett. 95 (2009), p. 223108.
[87] T. Shen, J.J. Gu, M. Xu, Y.Q. Wu, M.L. Bolen, M.A. Capano, L.W. Engel, and P.D. Ye, Appl. Phys. Lett. 95 (2009), p. 172105.
[88] Z. Jiang, Y. Zhang, Y.-W. Tan, H.L. Stormer, and P. Kim, Solid State Commun. 143 (2007), pp. 14–19.
[89] A.J.M. Giesbers, U. Zeitler, M.I. Katsnelson, L.A. Ponomarenko, T.M. Mohiuddin, and J.C. Maan, Phys. Rev. Lett. 99 (2007), p. 206803.
[90] A.J.M. Giesbers, U. Zeitler, M.I. Katsnelson, L.A. Ponomarenko, T.M.G. Mohiuddin, and J.C. Maan, Physica E 40 (2008), pp. 1089–1091.
[91] Z. Jiang, Y. Zhang, H.L. Stormer, and P. Kim, Phys. Rev. Lett. 99 (2007), p. 106802.
[92] Y. Zhang, Z. Jiang, J.P. Small, M.S. Purewal, Y.-W. Tan, M. Fazlollahi, J.D. Chudow, J.A. Jaszczak, H.L. Stormer, and P. Kim, Phys. Rev. Lett. 96 (2006), p. 136806.
[93] J.G. Checkelsky, L. Li, and N.P. Ong, Phys. Rev. Lett. 100 (2008), p. 206801.
[94] J.G. Checkelsky, L. Li, and N.P. Ong, Phys. Rev. B 79 (2009), p. 115434.
[95] X. Du, I. Skachko, F. Duerr, A. Luican, and E.Y. Andrei, Nature 462 (2009), p. 192.
[96] K.I. Bolotin, F. Ghahari, M.D. Shulman, H.L. Stormer, and P. Kim, Nature 462 (2009), p. 196.
[97] A.J.M. Giesbers, L.A. Ponomarenko, K.S. Novoselov, A.K. Geim, M.I. Katsnelson, J.C. Maan, and U. Zeitler, Phys. Rev. B 80 (2009), p. 201403.
[98] K. Nomura and A.H. MacDonald, Phys. Rev. Lett. 96 (2006), p. 256602.
[99] D.N. Sheng, L. Sheng, and Z.Y. Weng, Phys. Rev. B 73 (2006), p. 233406.
[100] V.P. Gusynin, V.A. Miransky, S.G. Sharapov, and I.A. Shovkovy, Phys. Rev. B 74 (2006), p. 195429.
[101] M.O. Goerbig, R. Moessner, and B. Douçot, Phys. Rev. B 74 (2006), p. 161407(R).
[102] K. Yang, S. Das Sarma, and A.H. MacDonald, Phys. Rev. B 74 (2006), p. 075423.
[103] J. Alicea and M.P.A. Fisher, Solid. State. Commun. 143 (2007), pp. 504–509.
[104] D.A. Abanin, P.A. Lee, and L.S. Levitov, Sol. State. Commun. 143 (2007), pp. 77–85.
[105] M. Koshino and T. Ando, Phys. Rev. B 75 (2007), p. 033412.
[106] L. Sheng, D.N. Sheng, F.D.M. Haldane, and L. Balents, Phys. Rev. Lett. 99 (2007), p. 196802.
[107] K. Yang, Solid State Commun. 143 (2007), pp. 27–32.
[108] E.V. Gorbar, V.P. Gusynin, and V.A. Miransky, Low Temp. Phys. 34 (2008), p. 790.
[109] V.P. Gusynin, V.A. Miransky, S.G. Sharapov, and I.A. Shovkovy, Phys. Rev. B 77 (2008), p. 205409.
[110] A.L.C. Pereira and P.A. Schulz, Phys. Rev. B 77 (2008), p. 075416.
[111] V.P. Gusynin, V.A. Miransky, S.G. Sharapov, and I.A. Shovkovy, Low Temp. Phys. 34 (2008), p. 778.
[112] T. Kawarabayashi, Y. Hatsugai, and H. Aoki, Phys. Rev. Lett. 103 (2009), p. 156804.
[113] T. Chakraborty and P. Pietiläinen, Eur. Phys. Lett. 80 (2007), p. 37007.

[114] I.F. Herbut, Phys. Rev. B 75 (2007), p. 165411.
[115] J.-N. Fuchs and P. Lederer, Phys. Rev. Lett. 98 (2007), p. 016803.
[116] N.A. Viet, H. Ajiki, and T. Ando, J. Phys. Soc. Japan 63 (1994), p. 3036.
[117] H. Ajiki and T. Ando, J. Phys. Soc. Japan 64 (1995), p. 260.
[118] H. Ajiki and T. Ando, J. Phys. Soc. Japan 65 (1996), p. 2976.
[119] H. Ajiki and T. Ando, Phys. B 227 (1996), p. 342.
[120] M. Arikawa, Y. Hatsugai, and H. Aoki, Phys. Rev. B 78 (2008), p. 205401.
[121] S. Park and H.-S. Sim, Phys. Rev. B 77 (2008), p. 075433.
[122] L. Brey and H.A. Fertig, Phys. Rev. B 73 (2006), p. 195408.
[123] D.A. Abanin, P.A. Lee, and L.S. Levitov, Phys. Rev. Lett. 96 (2006), p. 176803.
[124] A.H. Castro Neto, F. Guinea, and N.M.R. Peres, Phys. Rev. B 73 (2006), p. 205408.
[125] H.A. Fertig and L. Brey, Solid State Commun. 143 (2007), pp. 86–91.
[126] D.A. Abanin, K.S. Novoselov, U. Zeitler, P.A. Lee, A.K. Geim, and L.S. Levitov, Phys. Rev. Lett. 98 (2007), p. 196806.
[127] D.-K. Ki, S. Jo, and H.-J. Lee, Appl. Phys. Lett. 94 (2009), p. 162113.
[128] E. Shimshoni, H.A. Fertig, and G.V. Pai, Phys. Rev. Lett. 102 (2009), p. 206408.
[129] V.M. Apalkov and T. Chakraborty, Phys. Rev. Lett. 97 (2006), p. 126801.
[130] V. Apalkov, X.-F. Wang, and T. Chakraborty, Int. J. Mod. Phys. B 21 (2007), pp. 1165–1179.
[131] M.O. Goerbig and N. Regnault, Phys. Rev. B 75 (2007), p. 241405.
[132] C. Toke, P.E. Lammert, V.H. Crespi, and J.K. Jain, Phys. Rev. B 74 (2006), p. 235417.
[133] Z. Papic, M.O. Goerbig, and N. Regnault, Solid State Commun. 149 (2009), p. 1056.
[134] F.D.M. Haldane, Phys. Rev. Lett. 51 (1983), p. 605.
[135] N. Shibata and K. Nomura, J. Phys. Soc. Japan 78 (2009), p. 104708.
[136] C.-H. Zhang and Y.N. Joglekar, Phys. Rev. B 75 (2007), p. 245414.
[137] R.B. Laughlin, Phys. Rev. Lett. 50 (1983), p. 1395.
[138] D.A. Abanin, I. Skachko, X. Du, E.Y. Andrei, and L.S. Levitov, Phys. Rev. B 81 (2010), p. 115410.
[139] E. McCann and V.I. Falko, Phys. Rev. Lett. 96 (2006), p. 086805.
[140] T. Ohta, A. Bostwick, T. Seyller, K. Horn, and E. Rotenberg, Science 313 (2006), p. 951.
[141] K.S. Novoselov, E. McCann, S.V. Morozov, V.I. Falko, M.I. Katsnelson, U. Zeitler, D. Jiang, F. Schedin, and A.K. Geim, Nat. Phys. 2 (2006), p. 177.
[142] P. Blake, E.W. Hill, A.H. Castro Neto, K.S. Novoselov, D. Jiang, R. Yang, T.J. Booth, and A.K. Geim, Appl. Phys. Lett. 91 (2007), p. 063124.
[143] D.S.L. Abergel, A. Russell, and V.I. Falko, Appl. Phys. Lett. 91 (2007), p. 063125.
[144] S. Roddaro, P. Pingue, V. Piazza, V. Pellegrini, and F. Beltram, Nano Lett. 7 (2007), p. 2707.
[145] C. Casiraghi, A. Hartschuh, E. Lidorikis, H. Qian, H. Harutyunyan, T. Gokus, K.S. Novoselov, and A.C. Ferrari, Nano Lett. 7 (2007), p. 2711.
[146] R.R. Nair, P. Blake, A.N. Grigorenko, K.S. Novoselov, T.J. Booth, T. Stauber, N.M.R. Peres, and A.K. Geim, Science 320 (2008), p. 1308.
[147] A.B. Kuzmenko, E. van Heumen, D. van der Marel, P. Lerch, P. Blake, K.S. Novoselov, and A.K. Geim, Phys. Rev. B 79 (2009), p. 115441.
[148] F. Wang, Y. Zhang, C. Tian, C. Girit, A. Zettl, M. Crommie, and Y.R. Shen, Science 320 (2008), p. 206.
[149] E.J. Nicol and J.P. Carbotte, Phys. Rev. B 77 (2008), p. 155409.
[150] L. Benfatto, S.G. Sharapov, and J.P. Carbotte, Phys. Rev. B 77 (2008), p. 125422.
[151] D.S.L. Abergel and V.I. Falko, Phys. Rev. B 75 (2007), p. 155430.
[152] Z.H. Ni, H.M. Wang, J. Kasim, H.M. Fan, T. Yu, Y.H. Wu, Y.P. Feng, and Z.X. Shen, Nano Lett. 7 (2007), p. 2758.

[153] P.E. Gaskell, H.S. Skulason, C. Rodenchuk, and T. Szkopek, Appl. Phys. Lett. 94 (2009), p. 143101.
[154] E.D. Palik, *Handbook of Optical Constants of Solids*, Elsevier, New York, 1998.
[155] G.E. Jellison, J.D. Hunn, and H.N. Lee, Phys. Rev. B 76 (2007), p. 085125.
[156] E.A. Obraztsova, A.V. Osadchy, E.D. Obraztsova, S. Lefrant, and I.V. Yaminsky, Phys. Status Solidi b 245 (2008), p. 2055.
[157] J.H. Warner, M.H. Rümmeli, T. Gemming, B. Büchner, and G.A.D. Briggs, Nano Lett. 9 (2009), p. 102.
[158] E. Sutter, D.P. Acharya, J.T. Sadowski, and P. Sutter, Appl. Phys. Lett. 94 (2009), p. 133101.
[159] D. Graf, F. Molitor, K. Ensslin, C. Stampfer, A. Jungen, C. Hierold, and L. Wirtz, Nano Lett. 7 (2007), p. 238.
[160] P. Poncharal, A. Ayari, T. Michel, and J.-L. Sauvajol, Phys. Rev. B 78 (2008), p. 113407.
[161] Z. Ni, Y. Wang, T. Yu, Y. You, and Z. Shen, Phys. Rev. B 77 (2008), p. 235403.
[162] J.M. Lopes dos Santos, N.M.R. Peres, and A.H. Castro Neto, Phys. Rev. Lett. 99 (2007), p. 256802.
[163] T. Ohta, A. Bostwick, J.L. McChesney, T. Seyller, K. Horn, and E. Rotenberg, Phys. Rev. Lett. 98 (2007), p. 206802.
[164] A.B. Kuzmenko, I. Crassee, D. van der Marel, P. Blake, and K.S. Novoselov, Phys. Rev. B 80 (2009), p. 165406.
[165] L.M. Zhang, Z.Q. Li, D.N. Basov, M.M. Fogler, Z. Hao, and M.C. Martin, Phys. Rev. B 78 (2008), p. 235408.
[166] L.M. Malard, J. Nilsson, D.C. Elias, J.C. Brant, F. Plentz, E.S. Alves, A.H. Castro Neto, and M.A. Pimenta, Phys. Rev. B 76 (2007), p. 201401(R).
[167] L.M. Malard, J. Nilsson, D.L. Mafra, D.C. Elias, J.C. Brant, F. Plentz, E.S. Alves, A.H. Castro Neto, and M.A. Pimenta, Phys. Status Solidi b 245 (2008), p. 2060.
[168] H. Min, B. Sahu, S.K. Banerjee, and A.H. MacDonald, Phys. Rev. B 75 (2007), p. 155115.
[169] P. Gava, M. Lazzeri, A. Marco Saitta, and F. Mauri, Phys. Rev. B 79 (2009), p. 165431.
[170] M. Mucha-Kruczyński, O. Tsyplyatyev, A. Grishin, E. McCann, V.I. Falko, A. Bostwick, and E. Rotenberg, Phys. Rev. B 77 (2008), p. 195403.
[171] Z.F. Wang, Q. Li, H. Su, X. Wang, Q.W. Shi, J. Chen, J. Yang, and J.G. Hou, Phys. Rev. B 75 (2007), p. 085424.
[172] M.I. Katsnelson and M.F. Prokhorova, Phys. Rev. B 77 (2008), p. 205424.
[173] J.C. Meyer, A.K. Geim, M.I. Katsnelson, K.S. Novoselov, D. Obergfell, S. Roth, C. Girit, and A. Zettl, Solid State Commun. 143 (2007), p. 101.
[174] S.Y. Zhou, G.-H. Gweon, J. Graf, A.V. Fedorov, C.D. Spataru, R.D. Diehl, Y. Kopelevich, D.-H. Lee, Steven G. Louie, and A. Lanzara, Nat. Phys. 2 (2006), p. 595.
[175] M. Mucha-Kruczyński, D.S.L. Abergel, E. McCann, and V.I. Falko, J. Phys.: Condens. Matter 21 (2009), p. 344206.
[176] K. Kechedzhi, V.I. Falko, E. McCann, and B.L. Altshuler, Phys. Rev. Lett. 98 (2007), p. 176806.
[177] R.V. Gorbachev, F.V. Tikhonenko, A.S. Mayorov, D.W. Horsell, and A.K. Savchenko, Phys. Rev. Lett. 98 (2007), p. 176805.
[178] E. McCann, Phys. Rev. B 74 (2006), p. 161403.
[179] A. Bostwick, T. Ohta, J.L. McChesney, K.V. Emtsev, T. Seyller, K. Horn, and E. Rotenberg, New J. Phys. 9 (2007), p. 385.
[180] F. Guinea, A.H. Castro Neto, and N.M.R. Peres, Phys. Rev. B 73 (2006), p. 245426.
[181] E.V. Castro, K.S. Novoselov, S.V. Morozov, N.M.R. Peres, J.M.B. Lopes dos Santos, J. Nilsson, F. Guinea, A.K. Geim, and A.H. Castro Neto, Phys. Rev. Lett. 99 (2007), p. 216802.

[182] V.M. Pereira, R.M. Ribeiro, N.M.R. Peres, and A.H. Castro Neto, Phys. Rev. B 79 (2009), p. 045421.
[183] K.F. Mak, C.H. Lui, J. Shan, and T.F. Heinz, Phys. Rev. Lett. 102 (2009), p. 256405.
[184] Y. Zhang, T.-T. Tang, C. Girit, Z. Hao, M.C. Martin, A. Zettl, M.F. Crommie, Y.R. Shen, and F. Wang, Nature 459 (2009), p. 820.
[185] J.B. Oostinga, H.B. Heersche, X. Liu, A.F. Morpurgo, and L.M.K. Vandersypen, Nat. Mater. 7 (2008), p. 151.
[186] M. Aoki and H. Amawashi, Solid State Commun. 142 (2007), p. 123.
[187] G. Fiori and G. Iannaccone, IEEE Electron Dev. Lett. 30 (2009), p. 261.
[188] J.-R. Huang, J.-Y. Lin, B.-H. Chen, and M.-H. Tsai, Phys. Status Solidi b 245 (2007), p. 136.
[189] E.K. Yu, D.A. Stewart, and S. Tiwari, Phys. Rev. B 77 (2008), p. 195406.
[190] J. Milton Pereira Jr, F.M. Peeters, and P. Vasilopoulos, Phys. Rev. B 76 (2007), p. 115419.
[191] N. Nemec and G. Cuniberti, Phys. Rev. B 75 (2007), p. 201404.
[192] M. Nakamura, L. Hirasawa, and K.-I. Imura, Phys. Rev. B 78 (2008), p. 033403.
[193] Y.H. Lai, J.H. Ho, C.P. Chang, and M.F. Lin, Phys. Rev. B 77 (2008), p. 085426.
[194] E.A. Henriksen, Z. Jiang, L.-C. Tung, M.E. Schwartz, M. Takita, Y.-J. Wang, P. Kim, and H.L. Stormer, Phys. Rev. Lett. 100 (2008), p. 087403.
[195] D.S.L. Abergel and T. Chakraborty, Phys. Rev. Lett. 102 (2009), p. 056807.
[196] M. Mucha-Kruczyński, E. McCann, and V.I. Falko, Solid State Commun. 149 (2009), p. 1111.
[197] Y.C. Huang, C.P. Chang, and M.F. Lin, Phys. Rev. B 78 (2008), p. 115422.
[198] S. Viola Kusminskiy, D.K. Campbell, and A.H. Castro Neto, Eur. Phys. Lett. 85 (2009), p. 58005.
[199] M. Ezawa, J. Phys. Soc. Japan 76 (2007), p. 094701.
[200] M. Ezawa, Physica E 40 (2007), p. 269.
[201] T. Misumi and K. Shizuya, Phys. Rev. B 77 (2008), p. 195423.
[202] Y. Barlas, R. Côté, K. Nomura, and A.H. MacDonald, Phys. Rev. Lett. 101 (2008), p. 097601.
[203] K. Shizuya, Phys. Rev. B 79 (2009), p. 165402.
[204] T. Ando, J. Phys. Soc. Japan 76 (2007), p. 104711.
[205] B.E. Feldman, J. Martin, and A. Yacoby, Nat. Phys. 5 (2009), p. 889.
[206] Y. Zhao, P. Cadden-Zimansky, Z. Jiang, and P. Kim, Phys. Rev. Lett. 104 (2010), p. 066801.
[207] J. Nilsson, A.H. Castro Neto, N.M.R. Peres, and F. Guinea, Phys. Rev. B 73 (2006), p. 214418.
[208] E.H. Hwang and S. Das Sarma, Phys. Rev. Lett. 101 (2008), p. 156802.
[209] T. Stauber, N.M.R. Peres, F. Guinea, and A.H. Castro Neto, Phys. Rev. B 75 (2007), p. 115425.
[210] E.V. Castro, N.M.R. Peres, T. Stauber, and N.A.P. Silva, Phys. Rev. Lett. 100 (2008), p. 186803.
[211] S. Viola Kusminskiy, J. Nilsson, D.K. Campbell, and A.H. Castro Neto, Phys. Rev. Lett. 100 (2008), p. 106805.
[212] E.H. Hwang, B.Y.-K. Hu, and S. Das Sarma, Phys. Rev. Lett. 99 (2007), p. 226801.
[213] J. Martin, N. Akerman, G. Ulbricht, T. Lohmann, J.H. Smet, K. von Klitzing, and A. Yacoby, Nat. Phys. 4 (2008), p. 144.
[214] S.K. Saha, U.V. Waghmare, H.R. Krishnamurthy, and A.K. Sood, Phys. Rev. B 78 (2008), p. 165421.
[215] J.-A. Yan, W.Y. Ruan, and M.Y. Chou, Phys. Rev. B 77 (2008), p. 125401.

[216] S. Piscanec, M. Lazzari, F. Mauri, A.C. Ferrari, and J. Robertson, Phys. Rev. Lett. 93 (2004), p. 185503.
[217] J. Yan, E.A. Henriksen, P. Kim, and A. Pinczuk, Phys. Rev. Lett. 101 (2008), p. 136804.
[218] L.M. Malard, D.C. Elias, E.S. Alves, and M.A. Pimenta, Phys. Rev. Lett. 101 (2008), p. 257401.
[219] L.M. Malard, M.H.D. Guimarães, D.L. Mafra, M.S.C. Mazzoni, and A. Jorio, Phys. Rev. B 79 (2009), p. 125426.
[220] A.H. Castro Neto and F. Guinea, Phys. Rev. B 75 (2007), p. 045404.
[221] A. Das, B. Chakraborty, S. Piscanec, S. Pisana, A.K. Sood, and A.C. Ferrari, Phys. Rev. B 79 (2009), p. 155417.
[222] T. Ando and M. Koshino, J. Phys. Soc. Japan 78 (2009), p. 034709.
[223] I. Martin, Ya.M. Blanter, and A.F. Morpurgo, Phys. Rev. Lett. 100 (2008), p. 036804.
[224] D.S.L. Abergel and T. Chakraborty, Appl. Phys. Lett. 95 (2009), p. 062107.
[225] P. San-Jose, E. Prada, E. McCann, and H. Schomerus, Phys. Rev. Lett. 102 (2009), p. 247204.
[226] H. Min, G. Borghi, M. Polini, and A.H. MacDonald, Phys. Rev. B 77 (2008), p. 041407.
[227] D.S.L. Abergel, P. Pietiläinen, and T. Chakraborty, Phys. Rev. B 80 (2009), p. 081408(R).
[228] D. Pines and P. Nozieres, *The Theory of Quantum Liquids*, Vol. 1, Benjamin, New York, 1966.
[229] G.D. Mahan, *Many Particle Physics*, 3rd ed., Kluwer/Plenum, New York, 2000.
[230] J.P. Eisenstein, L.N. Pfeiffer, and K.W. West, Phys. Rev. Lett. 68 (1992), p. 674; Phys. Rev. B 50 (1994), p. 1760; I.S. Millard, N.K. Patel, C.L. Foden, E.H. Linfield, M.Y. Simmons, D.A. Ritchie, and M. Pepper, *ibid.* B 55 (1997), p. 6715; E.A. Galaktionov, G.D. Allison, M.M. Fogler, A.K. Savchenko, S.S. Safonov, M.Y. Simmons, and D.A. Ritchie, Physica E 34 (2006), p. 240; S.I. Dorozhkin, J.H. Smet, K. von Klitzing, V. Umansky, W. Wegscheider, R.J. Haug, and K. Ploog, *ibid.* 12 (2002), p. 97.
[231] Y. Barlas, T. Pereg-Barnea, M. Polini, R. Asgari, and A.H. MacDonald, Phys. Rev. Lett. 98 (2007), p. 236601.
[232] D.E. Sheehy and J. Schmalian, Phys. Rev. Lett. 99 (2007), p. 226803.
[233] There are many effects predicted in the literature that are directly attributed to the presence of Coulomb interactions in monolayer graphene. See, for example, J. Gonzalez, F. Guinea, and M.A.H. Vozmediano, Phys. Rev. B 63 (2001), p. 134421; E.G. Mishchenko, Phys. Rev. Lett. 98 (2007), p. 216801; I.F. Herbut, V. Juricic, and O. Vafek, Phys. Rev. Lett. 100 (2008), p. 046403; M. Polini, R. Asgari, G. Borghi, Y. Barlas, T. Pereg-Barnea, and A.H. MacDonald, Phys. Rev. B 77 (2008), p. 081411.
[234] M.W.C. Dharma-wardana, Phys. Rev. B 75 (2007), p. 075427.
[235] B. Tanatar and D.M. Ceperley, Phys. Rev. B 39 (1989), p. 5005.
[236] H.P. Dahal, Y.N. Joglekar, K.S. Bedell, and A.V. Balatsky, Phys. Rev. B 74 (2006), p. 233405.
[237] F.A. Stevens Jr and M.A. Pokrant, Phys. Rev. A 8 (1973), p. 990.
[238] X.F. Wang and T. Chakraborty, Phys. Rev. B 75 (2007), p. 033408.
[239] X.F. Wang and T. Chakraborty, Phys. Rev. B 75 (2007), p. 041404(R).
[240] B. Wunsch, T. Stauber, F. Sols, and F. Guinea, New J. Phys. 8 (2006), p. 318.
[241] E.H. Hwang and S. Das Sarma, Phys. Rev. B 75 (2007), p. 205418.
[242] A. Qaiumzadeh and R. Asgari, Phys. Rev. B 79 (2009), p. 075414.
[243] P.K. Pyatkovskiy, J. Phys.: Condens. Matter 21 (2009), p. 025506.
[244] M. Polini, R. Asgari, G. Borghi, Y. Barlas, T. Pereg-Barnea, and A.H. MacDonald, Phys. Rev. B 77 (2008), p. 081411(R).

[245] Y. Barlas and K. Yang, Phys. Rev. B 80 (2009), p. 161408(R).
[246] A. Hill, S.A. Mikhailov, and K. Ziegler, Eur. Phys. Lett. 87 (2009), p. 27005.
[247] C.L. Kane and E.J. Mele, Phys. Rev. Lett. 95 (2005), p. 226801.
[248] N.A. Sinitsyn, J.E. Hill, H. Min, J. Sinava, and A.H. Mac Donald, Phys. Rev. Lett. 97 (2006), p. 106804.
[249] H. Min, J.E. Hill, N.A. Sinitsyn, B.R. Sahu, L. Kleinman, and A.H. MacDonald, Phys. Rev. B 74 (2006), p. 165310.
[250] B. Vinter, Phys. Rev. B 15 (1977), p. 3947.
[251] X.F. Wang, Phys. Rev. B 72 (2005), p. 85317.
[252] N.M.R. Peres, F. Guinea, and A.H. Castro Neto, Phys. Rev. B 72 (2005), p. 174406.
[253] D.P. DiVincenzo and E.J. Mele, Phys. Rev. B 29 (1984), p. 1685.
[254] A. Bostwick, T. Ohta, J.L. McChesney, T. Seyller, K. Horn, and E. Rotenberg, Solid State Commun. 143 (2007), p. 63.
[255] A. Bostwick, T. Ohta, J.L. McChesney, T. Seyller, K. Horn, and E. Rotenberg, Eur. Phys. J. Spec. Top. 148 (2007), p. 5.
[256] A. Qaiumzadeha, N. Arabchi, and R. Asgari, Solid State Commun. 147 (2008), p. 172.
[257] D.V. Khveshchenko, Phys. Rev. B 74 (2006), p. 161402(R).
[258] O. Vafek, Phys. Rev. Lett. 97 (2006), p. 266406.
[259] Y.H. Chiu, J.H. Ho, C.P. Chang, D.S. Chuu, and M.F. Lin, Phys. Rev. B 78 (2008), p. 245411.
[260] F. Rana, IEEE Trans. Nanotechnol. 7 (2008), p. 91.
[261] A.R. Wright, G.X. Wang, W. Xu, Z. Zeng, and C. Zhang , Microelectron. J. 40 (2009), p. 857.
[262] M. Koshino and T. Ando, Phys. Rev. B 73 (2006), p. 245403.
[263] M Tahir and K Sabeeh, J. Phys.: Condens. Matter 20 (2008), p. 425202.
[264] M. Tahir and K. Sabeeh, Phys. Rev. B 76 (2007), p. 195416.
[265] O.L. Berman, G. Gumbs, and Y.E. Lozovik, Phys. Rev. B 78 (2008), p. 085401.
[266] S. Adam and S. Das Sarma, Phys. Rev. B 77 (2008), p. 115436.
[267] J. Nilsson, A.H. Castro Neto, F. Guinea, and N.M.R. Peres, Phys. Rev. B 78 (2008), p. 045405.
[268] X.-F. Wang and T. Chakraborty, Phys. Rev. B 81 (2010), p. 081402 (R).
[269] T. Oka and H. Aoki, Phys. Rev. B 79 (2009), p. 081406(R). See also the associated Erratum: T. Oka and H. Aoki, Phys. Rev. B 79 (2009), p. 169901(E).
[270] M.V. Fistul and K.B. Efetov, Phys. Rev. Lett. 98 (2007), p. 256803.
[271] S.E. Shafranjuk, J. Phys.: Condens. Matter 21 (2009), p. 015301.
[272] F.J. López-Rodríguez and G.G. Nuamis, Phys. Rev. B 78 (2008), p. 201406(R).
[273] A.R. Wright, J.C. Cao, and C. Zhang, Phys. Rev. Lett. 103 (2009), p. 207401.
[274] K. Nomura and A.H. MacDonald, Phys. Rev. Lett. 98 (2007), p. 076602.
[275] P.A. Lee, Phys. Rev. Lett. 71 (1993), p. 1887.
[276] N.M.R. Peres, F. Guinea, and A.H. Castro Neto, Phys. Rev. B 73 (2006), p. 125411.
[277] Y.-W. Tan, Y. Zhang, K. Bolotin, Y. Zhao, S. Adam, E.H. Hwang, S. Das Sarma, H.L. Stormer, and P. Kim, Phys. Rev. Lett. 99 (2007), p. 246803.
[278] J.H. Chen, C. Jang, S. Adam, M.S. Fuhrer, E.D. Williams, and M. Ishigami, Nat. Phys. 4 (2008), p. 377.
[279] R. Danneau, F. Wu, M.F. Craciun, S. Russo, M.Y. Tomi, J. Salmilehto, A.F. Morpurgo, and P.J. Hakonen, J. Low Temp. Phys. 153 (2008), p. 374.
[280] D.C. Elias, R.R. Nair, T.M.G. Mohiuddin, S.V. Morozov, P. Blake, M.P. Halsall, A.C. Ferrari, D.W. Boukhvalov, M.I. Katsnelson, A.K. Geim, and K.S. Novoselov, Science 323 (2009), p. 610.
[281] I.F. Herbut, V. Juricic, and O. Vafek, Phys. Rev. Lett. 100 (2008), p. 046403.
[282] E.G. Mishchenko, Europhys. Lett. 83 (2008), p. 17005.

[283] D.E. Sheehy and J. Schmalian, Phys. Rev. B 80 (2009), p. 193411.
[284] Z.Q. Li, E.A. Henriksen, Z. Jiang, Z. Hao, M.C. Martin, P. Kim, H.L. Stormer, and D.N. Basov, Nat. Phys. 4 (2008), p. 532.
[285] J. Yan, Y. Zhang, P. Kim, and A. Pinczuk, Phys. Rev. Lett. 98 (2007), p. 166802.
[286] T.M.G. Mohiuddin, A. Lombardo, R.R. Nair, A. Bonetti, G. Savini, R. Jalil, N. Bonini, D.M. Basko, C. Galiotis, N. Marzari, K.S. Novoselov, A.K. Geim, and A.C. Ferrari, Phys. Rev. B 79 (2009), p. 205433.
[287] Y. Zhang, V.W. Brar, F. Wang, C. Girit, Y. Yayon, M. Panlasigui, A. Zettl, and M.F. Crommie, Nat. Phys. 4 (2008), p. 627.
[288] A. Bostwick, J.L. McChesney, K.V. Emtsev, T. Seyller, K. Horn, S.D. Kevan, and E. Rotenberg, Phys. Rev. Lett. 103 (2009), p. 056404.
[289] A.H. Castro Neto, F. Guinea, N.M.R. Peres, K.S. Novoselov, and A.K. Geim, Rev. Mod. Phys. 81 (2009), p. 109.
[290] S.V. Morozov, K.S. Novoselov, M.I. Katsnelson, F. Schedin, L.A. Ponemereanteo, D. Jiany, and A.K. Gein, Phys. Rev. Lett. 97 (2006), p. 016801.
[291] E. McCann, K. Keehedzhi, V.I. Falko, H. Suzuura, T. Ando, and B.L. Altshuler, Phys. Rev. Lett. 97 (2006), p. 146805.
[292] H. Suzuura and T. Ando, *Anti-localization in a graphene sheet without spin-orbit interaction*, in *Physics of Semiconductors 2002*, A.R. Long and J.H. Davies, eds., Institute of Physics Publishing, Bristol, 2003, p. D226.
[293] B. Dóra and K. Ziegler, New J. Phys. 11 (2009), p. 095006.
[294] M.I. Katsnelson, Eur. Phys. J. B 51 (2006), p. 157.
[295] K. Ziegler, Phys. Rev. Lett. 97 (2006), p. 266802.
[296] K. Ziegler, Phys. Rev. B 78 (2008), p. 125401.
[297] J.Z. Bernád, U. Zülicke and K. Ziegler, Physica E42 (2010), p. 755.
[298] A.W.W. Ludwig, M.P.A. Fisher, R. Shankar, and G. Grinstein, Phys. Rev. B 50 (1994), p. 7526.
[299] E. Fradkin, Phys. Rev. B 33 (1986), p. 3263.
[300] K. Ziegler, Phys. Rev. Lett. 80 (1998), p. 3113.
[301] K. Ziegler, Phys. Rev. B 75 (2007), p. 233407.
[302] J.Z. Bernad, M. Jaaskelainen, U. Zuelicke, Phys. Rev. B 81 (2010), p. 073403.
[303] V.P. Gusynin, S.G. Sharapov, and J.P. Carbotte, Phys. Rev. Lett. 98 (2007), p. 157402.
[304] S.A. Mikhailov and K. Ziegler, Phys. Rev. Lett. 99 (2007), p. 016803.
[305] V.P. Gusynin, S.G. Sharapov, and J.P. Carbotte, New J. Phys. 11 (2009), p. 095013.
[306] J. Cserti, Phys. Rev. B. 75 (2007), p. 033405.
[307] H. Suzuura and T. Ando, Phys. Rev. Lett. 89 (2002), p. 266603.
[308] D.V. Khveshchenko, Phys. Rev. Lett. 97 (2006), p. 036802.
[309] N.H. Shon and T. Ando, J. Phys. Soc. Japan 67 (1998), p. 2421.
[310] V.S. Dotsenko and VI.S. Dotsenko, J. Phys. C 15 (1982), p. 495.
[311] I.L. Aleiner and K.B. Efetov, Phys. Rev. Lett. 97 (2006), p. 236801.
[312] M.S. Foster and I.L. Aleiner, Phys. Rev. B 77 (2008), p. 195413.
[313] A. Altland, Phys. Rev. Lett. 97 (2006), p. 236802.
[314] M. Boquet, D. Serban, and M.R. Zirnbauer, Nucl. Phys. B 578 (2000), p. 628.
[315] J.S. Langer and T. Neal, Phys. Rev. Lett. 16 (1966), p. 984.
[316] R. Oppermann and F. Wegner, Z. Phys. B 34 (1979), p. 327.
[317] P. Fulde, *Electron Correlations in Molecules and Solids*, Springer, Berlin, 1995.
[318] K. Ziegler, Phys. Rev. Lett. 102 (2009), p. 126802; Phys. Rev. B 79 (2009), p. 195424.
[319] A.A. Nersesyan, A.M. Tsvelik, and F. Wegner, Phys. Rev. Lett. 72 (1994), p. 2628.
[320] D.V. Khveshchenko, Europhys. Lett. 82 (2008), p. 57008.
[321] S.-J. Xiong and Y. Xiong, Phys. Rev. B 76 (2007), p. 214204.

[322] Y.-Y. Zhang, J. Hu, B.A. Bernevig, X.R. Wang, X.C. Xie, and W.M. Liu, Phys. Rev. Lett. 102 (2009), p. 106401.
[323] J.H. Bardarson, J. Tworzydlo, P.W. Brouwer, and C.W.J. Beenakker, Phys. Rev. Lett. 99 (2007), p. 106801.
[324] C.H. Lewenkopf, E.R. Mucciolo, and A.H. Castro Neto, Phys. Rev. B 77 (2008), p. 081410(R).
[325] J.H. Bardarson, M.V. Medvedyeva, J. Tworzydlo, A.R. Akhmerov, and C.W.J. Beenakker, Phys. Rev. B 81 (2010), p. 121414(R).
[326] H. Schomerus, Phys. Rev. B 76 (2007), p. 045433.
[327] E.J. Duplock, M. Scheffler, and P.J.D. Lindan, Phys. Rev. Lett. 92 (2004), p. 225502.
[328] V.M. Pereira, F. Guinea, J.M.B. Lopes dos Santos, N.M.R. Peres, and A.H. Castro Neto, Phys. Rev. Lett. 96 (2006), p. 036801.
[329] T. Stauber, N.M.R. Peres, and F. Guinea, Phys. Rev. B 76 (2007), p. 205423.
[330] F. Guinea, M.I. Katsnelson, and M.A.H. Vozmediano, Phys. Rev. B 77 (2008), p. 075422.
[331] V.V. Cheianov, V.I. Falko, B.L. Altshuler, and I.L. Aleiner, Phys. Rev. Lett. 99 (2007), p. 176801.
[332] K. Ziegler, A. Sinner, arXiv:1002.3734.
[333] S. Cho and M.P.A. Fisher, Phys. Rev. B 55 (1997), p. 1025.
[334] J.T. Chalker, N. Read, V. Kagalovsky, B. Herovitz, Y. Avishai, and A.W.W. Ludwig, Phys. Rev. B 65 (2001), p. 012506.
[335] M.V. Medvedyeva, J. Tworzydlo, and C.W.J. Beenakker, arxiv:1004.1111.
[336] D.V. Khveshchenko, Phys. Rev. Lett. 87 (2001), p. 206401.
[337] E.V. Gorbar, V.P. Gusynin, V.A. Miransky, and I.A. Shovkovy, Phys. Rev. B 66 (2002), p. 045108.
[338] J.E. Drut and T.A. Lähde, Phys. Rev. Lett. 102 (2009), p. 026802.
[339] M.R. Buitelaar, A. Bachtold, T. Nussbaumer, M. Iqbal, and C. Schönenberger, Phys. Rev. Lett. 88 (2002), p. 156801; D.H. Cobden and J. Nygřard, *ibid*. 89 (2002), p. 046803; S. Moriyama, T. Fuse, M. Suzuki, Y. Aoyagi, and K. Ishibashi, *ibid*. 94 (2005), p. 186806; S.-H. Ke, H.U. Baranger, and W. Yang, *ibid*. 91 (2003), p. 116803.
[340] K. Ishibashi, S. Moriyama, D. Tsuya, and T. Fuse, J. Vac. Sci. Technol. A 24 (2006), p. 1349.
[341] O. Klein, Z. Phys. 53 (1929), p. 157.
[342] M.I. Katsnelson, Mater. Today 10 (2007), p. 20.
[343] A. Calogeracos and N. Dombey, Contemp. Phys. 40 (1999), p. 313.
[344] N. Stander, B. Huard, and D. Goldhaber-Gordon, Phys. Rev. Lett. 102 (2009), p. 026807.
[345] A.F. Young and P. Kim, Nat. Phys. 5 (2009), pp. 222–226.
[346] R. Giachetti and E. Sorace, Phys. Rev. Lett. 101 (2008), p. 190401.
[347] L.A. Ponomarenko, F. Schedin, M.I. Katsnelson, R. Yang, E.W. Hill, K.S. Novoselov, and A.K. Geim, Science 320 (2008), p. 356.
[348] S. Schnez, F. Molitor, C. Stampfer, J. Güttinger, I. Shorubalko, T. Ihn, and K. Ensslin, Appl. Phys. Lett. 94 (2009), p. 012107.
[349] J. Güttinger, C. Stampfer, S. Hellmüller, F. Molitor, T. Ihn, and K. Ensslin, Appl. Phys. Lett. 93 (2008), p. 212102.
[350] H.-Y. Chen, V. Apalkov, and T. Chakraborty, Phys. Rev. Lett. 98 (2007), p. 186803.
[351] P.G. Silvestrov and K.B. Efetov, Phys. Rev. Lett. 98 (2007), p. 016802.
[352] A. De Martino, L. Dell'Anna, and R. Egger, Phys. Rev. Lett. 98 (2007), p. 066802.
[353] L. Dell'Anna and A. De Martino, Phys. Rev. B 79 (2009), p. 045420.
[354] W. Hausler and R. Egger, Phys. Rev. B 80 (2009), p. 161402.
[355] M.V. Berry and R.J. Mondragon, Proc. R. Soc. A 412 (1987), p. 53.

[356] J. Wurm, A. Rycerz, I. Adagideli, M. Wimmer, K. Richter, and H.U. Baranger, Phys. Rev. Lett. 102 (2009), p. 056806.
[357] F. Libisch, C. Stampfer, and J. Burgdörfer, Phys. Rev. B 79 (2009), p. 115423.
[358] T. Yamamoto, T. Noguchi, and K. Watanabe, Phys. Rev. B 74 (2006), p. 121409(R).
[359] M. Ezawa, Phys. Rev. B. 76 (2007), p. 245415.
[360] J. Fernandez-Rossier and J.J. Palacios, Phys. Rev. Lett. 99 (2007), p. 177204.
[361] Z.Z. Zhang, K. Chang, and F.M. Peeters, Phys. Rev. B 77 (2008), p. 235411.
[362] D. Jiang, B.G. Sumpter, and S. Dai, J. Chem. Phys. 127 (2007), p. 124703.
[363] C. Tang, W. Yan, Y. Zheng, G. Li, and L. Li, Nanotechnology 19 (2008), p. 435401.
[364] E. McCann and V.I. Falko, J. Phys.: Condens. Matter 16 (2004), p. 2371.
[365] A.R. Akhmerov and C.W.J. Beenakker, Phys. Rev. B 77 (2008), p. 085423.
[366] P. Potasz, A.D. Guclu, and P. Hawrylak, Phys. Rev. B 81 (2010), p. 033403.
[367] A.V. Rozhkov and F. Nori, Phys. Rev. B 81 (2010), p. 155401.
[368] B. Wunsch, T. Stauber, and F. Guinea, Phys. Rev. B 77 (2008), p. 035316.
[369] I. Romanovsky, C. Yannouleas, and U. Landman, Phys. Rev. B 79 (2009), p. 075311.
[370] Y. Aharonov and D. Bohm, Phys. Rev. 115 (1959), p. 485.
[371] S. Russo, J.B. Oostinga, D. Wehenkel, H.B. Heersche, S.S. Sobhani, L.M.K. Vandersypen, and A.F. Morpurgo, Phys. Rev. B 77 (2008), p. 085413.
[372] P. Recher, B. Trauzettel, A. Rycerz, Y.M. Blanter, C.W.J. Beenakker, and A.F. Morpurgo, Phys. Rev. B 76 (2007), p. 235404.
[373] D.S.L. Abergel, V.M. Apalkov, and T. Chakraborty, Phys. Rev. B 78 (2008), p. 193405.
[374] D.A. Bahamon, A.L.C. Pereira, and P.A. Schulz, Phys. Rev. B 79 (2009), p. 125414.
[375] E. Rossi, J.H. Bardarson, P.W. Brouwer, and S. Das Sarma, Phys. Rev. B 81 (2010), p. 121408(R).
[376] A. Matulis and F.M. Peeters, Phys. Rev. B 77 (2008), p. 115423.
[377] P. Hewageegana and V. Apalkov, Phys. Rev. B 79 (2009), p. 115418.
[378] P. Hewageegana and V. Apalkov, Phys. Rev. B 77 (2008), p. 245426.
[379] G. Gamow, Z. Phys. 51 (1928), p. 204.
[380] G. Giavaras, P.A. Maksym, and M. Roy, J. Phys.: Condens. Matter 21 (2009), p. 102201.
[381] J. Sucher, Phys. Rev. 107 (1957), p. 1448; 109 (1958), p. 1010; Phys. Rev. A 22 (1980), p. 348; Int. J. Quantum Chem. 25 (1984), p. 3.
[382] P. Recher, J. Nilsson, G. Burkard, and B. Trauzettel, Phys. Rev. B 79 (2009), p. 085407.
[383] G. Giovannetti, P.A. Khomyakov, G. Brocks, P.J. Kelly, and J. van der Brink, Phys. Rev. B 76 (2007), p. 073103.
[384] J.M. Pereira Jr, F.M. Peeters, and P. Vasilopoulos, Phys. Rev. B 75 (2007), p. 125433.
[385] S. Schnez, K. Ensslin, M. Sigrist, and T. Ihn, Phys. Rev. B 78 (2008), p. 195427.
[386] J. Milton Pereira Jr, P. Vasilopoulos, and F.M. Peeters, Nano Lett. 7 (2007), p. 946.
[387] S.E. Stein and R.L. Brown, J. Am. Chem. Soc. 109 (1987), p. 3721.
[388] K. Tanaka, S. Yamashita, H. Yamabe, and T. Yamabe, Synth. Met. 17 (1987), p. 143.
[389] M. Fujita, M. Yoshida, and K. Nakada, Fuller. Sci. Technol. 4 (1996), p. 565.
[390] M. Fujita, K. Wakabayashi, K. Nakada, and K. Kusakabe, J. Phys. Soc. Japan 65 (1996), p. 1920.
[391] K. Nakada, M. Fujita, G. Dresselhaus, and M.S. Dresselhaus, Phys. Rev. B 54 (1996), p. 17954.
[392] Z. Klusek, Z. Waqar, E.A. Denisov, T.N. Kompaniets, I.V. Makarenko, N. Titkov, and A.S. Bhatti, Appl. Surf. Sci. 161 (2000), p. 508.
[393] Y. Kobayashi, K. Fukui, T. Enoki, K. Kusakabe, and Y. Kaburagi, Phys. Rev. B 71 (2005), p. 193406.

[394] Y. Niimi, T. Matsui, H. Kambara, K. Tagami, M. Tsukada, and H. Fukuyama, Phys. Rev. B 73 (2006), p. 085421.
[395] Y. Kobayashi, K. Fukui, T. Enoki, and K. Kusakabe, Phys. Rev. B 73 (2006), p. 125415.
[396] K.N. Kudin, B. Ozbas, H.C. Schniepp, R.K. Prud'homme, I.A. Aksay, and R. Car, Nano Lett. 8 (2008), p. 36.
[397] T.O. Wehling, K.S. Novoselov, S.V. Morozov, E.E. Vdovin, M.I. Katsnelson, A.K. Geim, and A.I. Lichtenstein, Nano Lett. 8 (2008), p. 173.
[398] T. Lohmann, K. von Klitzing, and J.H. Smet, Nano Lett. 9 (2009), p. 1973.
[399] K. Sakaki, S. Murakami, and R. Saito, Appl. Phys. Lett. 88 (2006), p. 113110.
[400] K. Sakaki, S. Murakami, and R. Saito, J. Phys. Soc. Japan 75 (2006), p. 074713.
[401] M. Fujita, M. Igami, and K. Nakada, J. Phys. Soc. 66 (1997), p. 1864.
[402] S. Jun, Phys. Rev. B 78 (2008), p. 073405.
[403] S. Okada, Phys. Rev. B 77 (2008), p. 041408(R).
[404] P. Koskinen, S. Malola, and H. Hákkinen, Phys. Rev. Lett 101 (2008), p. 115502.
[405] P. Koskinen, S. Malola, and H. Hákkinen, Phys. Rev. B 80 (2009), p. 073401.
[406] N.M.R. Peres, M.A.N. Araújo, and D. Bozi, Phys. Rev. B 70 (2004), p. 195122.
[407] N.M.R. Peres, F. Guinea, and A.H. Castro Neto, Phys. Rev. B 72 (2005), p. 174406.
[408] K. Sasaki and R. Saito, J. Phys. Soc. Japan 77 (2008), p. 054703.
[409] H.-H. Lin, T. Hikihara, H.-T. Jeng, B.-L. Huang, C.-Y. Mou, and X. Hu, Phys. Rev. B 79 (2009), p. 035405.
[410] A. Yamashiro, Y. Shimoi, K. Harigaya, and K. Wakabayashi, Phys. Rev. B 68 (2003), p. 193410.
[411] S. Dutta, S.L. Lakshmi, and S.K. Pati, Phys. Rev. B 77 (2008), p. 073412.
[412] L. Pisani, J.A. Chan, B. Montanari, and N.M. Harrison, Phys. Rev. B 75 (2007), p. 064418.
[413] A. Yamashiro, Y. Shimoi, K. Harigaya, and K. Wakabayashi, Physica E 22 (2004), p. 668.
[414] H. Lee, Y.-W. Son, N. Park, S. Han, and J. Yu, Phys. Rev. B 72 (2005), p. 174431.
[415] J. Nakamura, T. Nitta, and A. Natori, Phys. Rev. B 72 (2005), p. 205429.
[416] J. Jung, T. Pereg-Barnea, and A.H. MacDonald, Phys. Rev. Lett. 102 (2009), p. 227205.
[417] F. Wu, E. Kan, H. Xiang, S.-H. Wei, M.-H. Whangbo, and J. Yang, Appl. Phys. Lett. 94 (2009), p. 223105.
[418] D.W. Boukhvalov and M.I. Katsnelson, Nano Lett. 8 (2008), p. 4373.
[419] Y.-W. Son, M.L. Cohen, and S.G. Louie, Phys. Rev. Lett 97 (2006), p. 216803.
[420] V. Barone, O. Hod, and G.E. Scuseria, Nano Lett. 6 (2006), p. 2748.
[421] M. Ezawa, Phys. Rev. B 73 (2006), p. 045432.
[422] L. Brey and H.A. Fertig, Phys. Rev. B 73 (2006), p. 235411.
[423] P. Shemella, Y. Zhang, M. Mailman, P.M. Ajayan, and S.K. Nayak, Appl. Phys. Lett. 91 (2007), p. 042101.
[424] L. Yang, C.-H. Park, Y.-W. Son, M.L. Cohen, and S.G. Louie, Phys. Rev. Lett 99 (2007), p. 186801.
[425] H. Zheng, Z.F. Wang, T. Luo, and Q.W. Shi, J. Chen, Phys. Rev. B 75 (2007), p. 165414.
[426] K. Kudin, ACS Nano 2 (2008), p. 516.
[427] H. Raza and E.C. Kan, Phys. Rev. B 77 (2008), p. 245434.
[428] Y.H. Lu, R.Q. Wu, L. Shen, M. Yang, Z.D. Sha, Y.Q. Cai, P.M. He, and Y.P. Feng, Appl. Phys. Lett. 94 (2009), p. 122111.
[429] X.W. Zhang and G.W. Yang, J. Phys. Chem. C. 113 (2009), p. 4662.
[430] A.K. Singh and B.I. Yakobson, Nano Lett. 9 (2009), p. 1540.
[431] F. Tseng, D. Unluer, K. Holcomb, M.R. Stan, and A.W. Ghosh, Appl. Phys. Lett. 94 (2009), p. 223112.
[432] Q. Yan, B. Huang, J. Yu, F. Zheng, J. Zang, J. Wu, B.-L. Gu, F. Liu, and W. Duan, Nano Lett. 7 (2007), p. 1469.

[433] H. Sevinçli, M. Topsakal, and S. Ciraci, Phys. Rev. B 78 (2008), p. 245402.
[434] M. Mohr, K. Papagelis, J. Maultzsch, and C. Thomsen, Phys. Rev. B 80 (2009), p. 205410.
[435] O. Hod, J.E. Peralta, and G.E. Scuseria, Phys. Rev. B 76 (2007), p. 233401.
[436] A.V. Rozhkov, S. Savel'ev, and F. Nori, Phys. Rev. B 79 (2009), p. 125420.
[437] M.Y. Han, B. Özyilmaz, Y. Zhang, and P. Kim, Phys. Rev. Lett. 98 (2007), p. 206805.
[438] M.Y. Han, B. Özyilmaz, Y. Zhang, R. Jarillo-Herero, and P. Kim, Phys. Status Solidi b 244 (2007), p. 4134.
[439] L. Tapasztó, G. Dobrik, P. Lambin, and L.P. Biró, Nat. Nanotechnol. 3 (2008), p. 397.
[440] F. Molitor, C. Stampfer, J. Güttinger, A. Jacobsen, T. Ihn, and K. Ensslin, Semicond. Sci. Technol. 25 (2010), p. 034002.
[441] K.A. Ritter and J.W. Lyding, Nat. Mater. 8 (2009), p. 235.
[442] Y.-W. Son, M.L. Cohen, and S.G. Louie, Nature 444 (2006), p. 347.
[443] O. Hod, V. Barone, J.E. Peralta, and G.E. Scuseria, Nano Lett. 7 (2007), p. 2295.
[444] R.P. Tiwari and D. Stroud, Phys. Rev. B 79 (2009), p. 205435.
[445] W. Yao, S.A. Yang, and Q. Niu, Phys. Rev. Lett. 102 (2009), p. 096801.
[446] E. Rudberg, P. Salek, and Y. Luo, Nano Lett. 7 (2007), p. 2211.
[447] E.-J. Kan, Z. Li, J. Yang, and J.G. Hou, Appl. Phys. Lett. 91 (2007), p. 243116.
[448] D. Dutta and S.K. Pati, J. Phys. Chem. B 112 (2008), p. 1333.
[449] J. Jung and A.H. MacDonald, Phys. Rev. B 79 (2009), p. 235433.
[450] S. Cho, Y.-F. Chen, and M.S. Fuhrer, Appl. Phys. Lett. 91 (2007), p. 123105.
[451] C. Ritter, S.S. Makler, and A. Latgé, Phys. Rev. B 77 (2008), p. 195443.
[452] D.S. Novikov, Phys. Rev. Lett. 99 (2007), p. 056802.
[453] V.M. Karpan, G. Giovannetti, P.A. Khomyakov, M. Talanana, A.A. Starikov, M. Zwierzycki, J. van der Brink, G. Brocks, and P.J. Kelly, Phys. Rev. Lett. 99 (2007), p. 176602.
[454] D. Gunlycke, D.A. Areshkin, J. Li, J.W. Mintmire, and C.T. White, Nano Lett. 7 (2007), p. 3608.
[455] W.Y. Kim and K.S. Kim, Nat. Nanotechnol. 3 (2008), p. 408.
[456] J. Guo, D. Gunlycke, and C.T. White, Appl. Phys. Lett. 92 (2008), p. 163109.
[457] T. Yokoyama, Phys. Rev. B 77 (2008), p. 073413.
[458] O.V. Yazyev and M.I. Katsnelson, Phys. Rev. Lett. 100 (2008), p. 047209.
[459] S. Hong, Y. Yoon, and J. Guo, Appl. Phys. Lett. 92 (2008), p. 083107.
[460] C. Józsa, M. Popinciuc, N. Tombros, H.T. Jonkman, and B.J. van Wees, Phys. Rev. Lett. 100 (2008), p. 236603.
[461] M. Ezawa, Eur. Phys. J. B 67 (2009), p. 543.
[462] J. Guo and Y. Ouyang, Appl. Phys. Lett. 94 (2009), p. 243104.
[463] F. Muñoz-Rojas, J. Fernández-Rossier, and J.J. Palacios, Phys. Rev. Lett. 102 (2009), p. 136810.
[464] W. Han, W.H. Wang, K. Pi, K.M. McCreary, W. Bao, Y. Li, F. Miao, C.N. Lau, and R.K. Kawakami, Phys. Rev. Lett. 102 (2009), p. 137205.
[465] Z. Xu, Q.-S. Zheng, and G. Chen, Appl. Phys. Lett. 90 (2007), p. 233115.
[466] O. Hod, V. Barone, and G.E. Scuseria, Phys. Rev. B 77 (2008), p. 035411.
[467] S. Banerjee and D. Bhattacharyya, Comput. Mater. Sci. 44 (2008), p. 41.
[468] M. Topsakal, H. Sevinçli, and S. Ciraci, Appl. Phys. Lett. 92 (2008), p. 173118.
[469] X. Wu and X.C. Zeng, Nano Res. 1 (2008), p. 40.
[470] S. Bhowmick and V.B. Shenoy, J. Chem. Phys. 128 (2008), p. 244717.
[471] E.H. Lieb, Phys. Rev. Lett. 62 (1989), p. 1201.
[472] O.V. Yazyev, W.L. Wang, S. Meng, and E. Kaxiras, Nano Lett. 8 (2008), p. 766.
[473] W.L. Wang, S. Meng, and E. Kaxiras, Nano Lett. 8 (2008), p. 241.

[474] M. Vanević, V.M. Stojanović, and M. Kindermann, Phys. Rev. B 80 (2009), p. 045410.
[475] B. Wang, J. Wang, and H. Guo, Phys. Rev. B 79 (2009), p. 165417.
[476] Z. Li, H. Qian, J. Wu, B.-L. Gu, and W. Duan, Phys. Rev. Lett. 100 (2008), p. 206802.
[477] F. Muñoz-Rojas, D. Jacob, J. Fernández-Rossier, and J.J. Palacios, Phys. Rev. B 74 (2006), p. 195417.
[478] M. Wimmer, İ. Adagideli, S. Berber, D. Tománek, and K. Richter, Rev. Lett. 100 (2008), p. 177207.
[479] L.A. Agapito and H.-P. Cheng, J. Phys. Chem. C 111 (2007), p. 14266.
[480] L. Rosales, M. Pacheco, Z. Barticevic, A. Latgé, and P.A. Orellana, Nanotechnology 20 (2009), p. 095705.
[481] H. Li, L. Wang, and Y. Zheng, J. Appl. Phys. 105 (2009), p. 013703.
[482] Y.P. Chen, Y.E. Xie, L.Z. Sun, and J. Zhong, Appl. Phys. Lett. 93 (2008), p. 092104.
[483] X. Li, X. Wang, L. Zhang, S. Lee, and H. Dai, Science 319 (2008), p. 1229.
[484] M.P. Lima, A. Fazzio, and Antônio J.R. da Silva, Phys. Rev. B 79 (2009), p. 153401.
[485] B. Sahu, H. Min, A.H. MacDonald, and S.K. Banerjee, Phys. Rev. B 78 (2008), p. 045404.
[486] E.V. Castro, N.M.R. Peres, J.M.B. Lopes dos Santos, A.H. Castro Neto, and F. Guinea, Phys. Rev. Lett. 100 (2008), p. 026802.
[487] J.-W. Rhim and K. Moon, J. Phys.: Condens. Matter 20 (2008), p. 365202.
[488] K.-T. Lam and G. Liang, Appl. Phys. Lett. 92 (2008), p. 223106.
[489] Y.C. Huang, C.P. Chang, and M.F. Lin, J. Appl. Phys. 104 (2008), p. 103714.
[490] E.V. Castro, N.M.R. Peres, and J.M.B. Lopes dos Santos, Eur. Phys. Lett. 84 (2008), p. 17001.
[491] X. Jian, M. Hofmann, V. Meunier, B.G. Sumpter, J. Campos-Delgado, J.M. Romo-Herrera, H. Son, Y.-P. Hsieh, A. Reina, J. Kong, M. Terrones, and M.S. Dresselhaus, Science 323 (2009), p. 1701.
[492] L. Jiao, L. Zhang, X. Wang, G. Diankov, and H. Dai, Nature 458 (2009), p. 877.
[493] D.V. Kosynkin, A.L. Higginbotham, A. Sinitskii, J.R. Lomeda, A. Dimiev, B.K. Price, and J.M. Tour, Nature 458 (2009), p. 872.
[494] G. Gui, J. Li, and J. Zhong, Phys. Rev. B 78 (2008), p. 075435.
[495] Z.H. Ni, T. Yu, Y.H. Lu, Y.Y. Wang, Y.P. Feng, and Z.X. Shen, ACS Nano 2 (2008), p. 2301.
[496] M. Huang, H. Yan, C. Chen, D. Song, T.F. Heinz, and J. Hone, PNAS 106 (2009), p. 7304.
[497] H.E. Romero, N. Shen, P. Joshi, H.R. Guitierrez, S.A. Tadigadapa, J.O. Sofo, and P.C. Eklund, ACS Nano 2 (2008), p. 2037.
[498] J. Hass, F. Varchon, J.E. Millán-Otoya, M. Sprinkle, N. Sharma, W.A. de Heer, C. Berger, P.N. First, L. Magaud, and E.H. Conrad, Phys. Rev. Lett. 100 (2008), p. 125504.
[499] D.S. Lee, C. Riedl, B. Krauss, K. von Klitzing, U. Starke, and J.H. Smet, Nano Lett. 8 (2008), p. 4320.
[500] Y. Shi, X. Dong, P. Chen, J. Wang, and L.-J. Li, Phys. Rev. B 79 (2009), p. 115402.
[501] F. Hiebel, P. Mallet, F. Varchon, L. Magaud, and J.-Y. Veuillen, Phys. Rev. B 78 (2008), p. 153412.
[502] F. Varchon, R. Feng, J. Hass, X. Li, B.N. Nguyen, C. Naud, P. Mallet, J.-Y. Veuillen, C. Berger, E.H. Conrad, and L. Magaud, Phys. Rev. Lett. 99 (2007), p. 126805.
[503] A. Mattausch and O. Pankratov, Phys. Rev. Lett. 99 (2007), p. 076802.
[504] I. Gierz, C. Riedl, U. Starke, C.R. Ast, and K. Kern, Nano Lett. 8 (2008), p. 4603.

[505] T.A.G. Eberlein, R. Jones, J.P. Goss, and P.R. Briddon, Phys. Rev. B 78 (2008), p. 045403.
[506] Y.-J. Kang, J. Kang, and K.J. Chang, Phys. Rev. B 78 (2008), p. 115404.
[507] Y.H. Lu, P.M. He, and Y.P. Feng, J. Phys. Chem. C 112 (2008), p. 12683.
[508] P. Shemella and S.K. Nayak, Appl. Phys. Lett. 94 (2009), p. 032101.
[509] M.M. Li, J. Zhang, F.J. Li, F.X. Zhu, M. Zhang, and X.F. Zhao, Phys. Status Solidi c. 6 (2009), p. S90.
[510] L. Magaud, F. Hiebel, F. Varchon, P. Mallet, and J.-Y. Veuillen, Phys. Rev. B 79 (2009), p. 161405(R).
[511] X. Peng and R. Ahuja, Nano Lett. 8 (2008), p. 4464.
[512] G. Giovannetti, P.A. Khomyakov, G. Brocks, V.M. Karpan, J. van den Brink, and P.J. Kelly, Phys. Rev. Lett. 101 (2008), p. 026803.
[513] P.A. Khomyakov, G. Giovannetti, P.C. Rusu, G. Brocks, J. van den Brink, and P.J. Kelly, Phys. Rev. B 79 (2009), p. 195425.
[514] F. Ortmann, W.G. Schmidt, and F. Bechstedt, Phys. Rev. Lett. 95 (2005), p. 186101.
[515] S.Y. Zhou, D.A. Siegel, A.V. Fedorov, and A. Lanzara, Phys. Rev. Lett. 101 (2008), p. 086402.
[516] X. Dong, Y. Shi, Y. Zhao, D. Chen, J. Ye, Y. Yao, F. Gao, Z. Ni, T. Yu, Z. Shen, Y. Huang, P. Chen, and L.-J. Li, Phys. Rev. Lett. 102 (2009), p. 135501.
[517] E. Bekyarova, M.E. Itkis, P. Ramesh, C. Berger, M. Sprinkle, W.A. de Heer, and R.C. Haddon, J. Am. Chem. Soc. 131 (2009), p. 1336.
[518] X. Dong, D. Fu, W. Fang, Y. Shi, P. Chen, and L.-J. Li, Small 5 (2009), p. 1422.
[519] R. Voggu, B. Das, C.S. Rout, and C.N.R. Rao, J. Phys.: Condens. Matter 20 (2008), p. 472204.
[520] P.O. Lehtinen, A.S. Foster, A. Ayuela, A. Krasheninnikov, K. Nordlund, and R.M. Nieminen, Phys. Rev. Lett. 91 (2003), p. 017202.
[521] I. Zanella, S. Guerini, S.B. Fagan, J. Mendes Filho, and A.G. Souza Filho, Phys. Rev. B 77 (2008), p. 073404.
[522] M. Wu, E.-Z. Liu, and J.Z. Jiang, Appl. Phys. Lett. 93 (2008), p. 082504.
[523] B. Huang, Z. Li, Z. Liu, G. Zhou, S. Hao, J. Wu, B.-L. Gu, and W. Duan, J. Phys. Chem. C 112 (2008), p. 13442.
[524] E.R. Margine, M.-L. Bocquet, and X. Blase, Nano Lett. 8 (2008), p. 3315.
[525] Y.G. Zhou, X.T. Zu, F. Gao, H.F. Lv, and H.Y. Xiao, Appl. Phys. Lett. 95 (2009), p. 123119.
[526] S.D. Dalosto and Z.H. Levine, J. Phys. Chem. C 112 (2008), p. 8196.
[527] O. Leenaerts, B. Partoens, and F.M. Peeters, Phys. Rev. B 77 (2008), p. 125416.
[528] O. Leenaerts, B. Partoens, and F.M. Peeters, Appl. Phys. Lett. 92 (2008), p. 243125.
[529] Y.-H. Zhang, Y.-B. Chen, K.-G. Zhou, C.-H. Liu, J. Zeng, H.-L. Zhang, and Y. Peng, Nanotechnology 20 (2009), p. 185504.
[530] S.J. Sque, R. Jones, and P.R. Briddon, Phys. Status Solidi a 204 (2007), p. 3078.
[531] Y.H. Lu, W. Chen, Y.P. Feng, and P.M. He, J. Phys. Chem. B 113 (2009), p. 2.
[532] O. Leenaerts, B. Partoens, and F.M. Peeters, Phys. Rev. B 79 (2009), p. 235440.
[533] J. Berashevich and T. Chakraborty, Phys. Rev. B 80 (2009), p. 033404.
[534] T.O. Wehling, A.I. Lichtenstein, and M.I. Katsnelson, Appl. Phys. Lett. 93 (2008), p. 202110.
[535] R.M. Ribeiro, N.M.R. Peres, J. Coutinho, and P.R. Briddon, Phys. Rev. B 78 (2008), p. 075442.
[536] X. Wang, X. Li, L. Zhang, Y. Yoon, P.K. Weber, H. Wang, J. Guo, and H. Dai, Science 324 (2009), p. 768.
[537] H.E. Romero, P. Joshi, A.K. Gupta, H.R. Gutierrez, M.W. Cole, S.A. Tadigadapa, and P.C. Eklund, Nanotechnology 20 (2009), p. 245501.

[538] A.K. Manna and S.K. Pati, Chem. Asian J. 4 (2009), p. 855.
[539] A.V. Shytov, D.A. Abanin, and L.S. Levitov, Phys. Rev. Lett. 103 (2009), p. 016806.
[540] R.H. Miwa, T.B. Martins, and A. Fazzio, Nanotechnology 19 (2008), p. 155708.
[541] D. Jiang, B.G. Sumpter, and S. Dai, J. Phys. Chem. B 110 (2006), p. 23628.
[542] A. Rochefort and J.D. Wuest, Langmuir 25 (2009), p. 210.
[543] P. Cabrera-Sanfelix, J. Phys. Chem. A 113 (2009), p. 493.
[544] L. Tsetseris and S.T. Pantelides, J. Phys. Chem. B 113 (2009), p. 941.
[545] M. Chi and Y.-P. Zhao, Comput. Mater. Sci. 46 (2009), p. 1085.
[546] Y.G. Zhou, X.T. Zu, F. Gao, J.L. Nie, and H.Y. Xiao, J. Appl. Phys. 105 (2009), p. 014309.
[547] P.A. Denis, J. Phys. Chem. C 113 (2009), p. 5612.
[548] J. Dai, J. Yuan, and P. Giannozzi, Appl. Phys. Lett. 95 (2009), p. 232105.
[549] J.O. Sofo, A.S. Chaudhari, and G.D. Barber, Phys. Rev. B 75 (2007), p. 153401.
[550] S. Lebégue, M. Klintenberg, O. Eriksson, and M.I. Katsnelson, Phys. Rev. B 79 (2009), p. 245117.
[551] U. Li, Z. Zhou, P. Shen, and Z. Chen, J. Phys. Chem. C 113 (2009), p. 15043.
[552] M.Z.S. Flores, P.A.S. Autreto, S.B. Legoas, and D.S. Galvao, Nanotechnology 20 (2009), p. 465704.
[553] S. Ryu, M.Y. Han, J. Maultzsch, T.F. Heinz, P. Kim, M.L. Steigerwald, and L.E. Brus, Nano Lett. 8 (2008), p. 4597.
[554] J. Zhou, Q. Wang, Q. Sun, X.S. Chen, Y. Kawazoe, and P. Jena, Nano Lett. 9 (2009), p. 3867.
[555] H. Şahin, C. Ataca, and S. Ciraci, Appl. Phys. Lett. 95 (2009), p. 222510.
[556] J. Berashevich and T. Chakraborty, arxiv: 1001.0919v1.
[557] L.A. Chernozatonski, P.B. Sorokin, and J.W. Brüning, Appl. Phys. Lett. 91 (2007), p. 183103.
[558] D.W. Boukhvalov, M.I. Katsnelson, and A.I. Lichtenstein, Phys. Rev. B 77 (2008), p. 035427.
[559] D.W. Boukhvalov and M.I. Katsnelson, Phys. Rev. B 78 (2008), p. 085413.
[560] C.-K. Yang, Appl. Phys. Lett. 94 (2009), p. 163115.
[561] M. Topsakal, S. Cahangirov, and S. Ciraci, Appl. Phys. Lett. 96 (2010), p. 091912.
[562] Y. Gan, L. Sun, and F. Banhart, Small 4 (2008), p. 587.
[563] R. Muszynski, B. Seger, and P.V. Kamat, J. Phys. Chem. C 112 (2008), p. 5263.
[564] C.G. Hwang, S.Y. Shin, S.-M. Choi, N.D. Kim, S.H. Uhm, H.S. Kim, C.C. Hwang, D.Y. Noh, S.-H. Jhi, and J.W. Chung, Phys. Rev. B 79 (2009), p. 115439.
[565] L. Tapasztó, G. Dobrik, P. Nemes-Incze, G. Vertesy, Ph. Lambin, and L.P. Biró, Phys. Rev. B 78 (2008), p. 233407.
[566] K. Pi, K.M. McCreary, W. Bao, W. Han, Y.F. Chiang, Y. Li, S.-W. Tsai, C.N. Lau, and R.K. Kawakami, Phys. Rev. B 80 (2009), p. 075406.
[567] Y. Mao, J. Yuan, and J. Zhong, J. Phys.: Condens. Matter 20 (2008), p. 115209.
[568] K.T. Chan, J.B. Neaton, and M.L. Cohen, Phys. Rev. B 77 (2008), p. 235430.
[569] B. Uchoa, C.-Y. Lin, and A.H. Castro Neto, Phys. Rev. B 77 (2008), p. 035420.
[570] A.H. Castro Neto, V.N. Kotov, J. Nilsson, V.M. Pereira, N.M.R. Peres, and B. Uchoa, Solid State Commun. 149 (2009), p. 1094.
[571] R. Varns and P. Strange, J. Phys.: Condens. Matter 20 (2008), p. 225005.
[572] G.M. Wang, J.J. BelBruno, S.D. Kenny, and R. Smith, Phys. Rev. B 69 (2004), p. 195412.
[573] Y. Okamoto, Chem. Phys. Lett. 420 (2006), p. 382.
[574] O.Ü. Aktürk and M. Tomak, Phys. Rev. B 80 (2009), p. 085417.
[575] S.S. Carara, R.J.C. Batista, and H. Chacham, Phys. Rev. B 80 (2009), p. 115435.
[576] M. Calandra and F. Mauri, Phys. Rev. B 76 (2007), p. 161406(R).

[577] J.L. McChesney, A. Bostwick, T. Ohta, K.V. Emtsev, T. Seyller, K. Horn and E. Rotenberg, arXiv:0705.3264.
[578] M.I. Rojas and E.P.M. Leiva, Phys. Rev. B 76 (2007), p. 155415.
[579] Q. Ran, M. Gao, X. Guan, Y. Wang, and Z. Yu, Appl. Phys. Lett. 94 (2009), p. 103511.
[580] M. Wu, E.-Z. Liu, M.Y. Ge, and J.Z. Jiang, Appl. Phys. Lett. 94 (2009), p. 102505.
[581] I. Zanella, S.B. Fagan, R. Mota, and A. Fazzio, J. Phys. Chem. C 112 (2008), p. 9163.
[582] N. Gorjizadeh, A.A. Farajian, K. Esfarjani, and Y. Kawazoe, Phys. Rev. B 78 (2008), p. 155427.
[583] Y. Sanchez-Paisal, D. Sanchez-Portal, and A. Ayuela, Phys. Rev. B 80 (2009), p. 045428.
[584] S.-M. Choi and S.-H. Jhi, Phys. Rev. Lett. 101 (2008), p. 266105.
[585] V.A. Rigo, T.B. Martins, A.J.R. da Silva, A. Fazzio, and R.H. Miwa, Phys. Rev. B 79 (2009), p. 075435.
[586] A.V. Krasheninnikov, P.O. Lehtinen, A.S. Foster, P. Pyykkö, and R.M. Nieminen, Phys. Rev. Lett. 102 (2009), p. 126807.
[587] D.W. Boukhvalov and M.I. Katsnelson, Appl. Phys. Lett. 95 (2009), p. 023109.
[588] H. Tachikawa, J. Phys. Chem. C 112 (2008), p. 10193.
[589] B. Uchoa, V.N. Kotov, N.M.R. Peres, and A.H. Castro Neto, Phys. Rev. Lett. 101 (2008), p. 026805.
[590] P. Esquinazi, D. Spemann, R. Höhne, A. Setzer, K.-H. Han, and T. Butz, Phys. Rev. Lett. 91 (2003), p. 227201.
[591] D. Teweldebrhan and A.A. Balandin, Appl. Phys. Lett. 94 (2009), p. 013101.
[592] Y. Wang, Y. Huang, Y. Song, X. Zhang, Y. Ma, J. Liang, and Y. Chen, Nano Lett. 9 (2009), p. 220.
[593] C. Casiraghi, S. Pisana, K.S. Novoselov, A.K. Geim, and A.C. Ferrari, Appl. Phys. Lett. 91 (2007), p. 233108.
[594] P.O. Lehtinen, A.S. Foster, Y. Ma, A.V. Krasheninnikov, and R.M. Neiminen, Phys. Rev. Lett 93 (2004), p. 187202.
[595] Y. Ma, P.O. Lehtinen, A.S. Foster, and R.M. Neiminen, New J. Phys. 6 (2004), p. 68.
[596] A.A. El-Barbary, R.H. Telling, C.P. Ewels, M.I. Heggie, and P.R. Briddon, Phys. Rev. B 68 (2003), p. 144107.
[597] H. Amara, S. Latil, V. Meunier, Ph. Lambin, and J.-C. Charlier, Phys. Rev. B 76 (2007), p. 115423.
[598] H. Tachikawa and H. Kawabata, J. Phys. Chem. C 113 (2009), p. 7603.
[599] O.V. Yazyev and L. Helm, Phys. Rev. B 75 (2007), p. 125408.
[600] G. Forte, A. Grassi, G.M. Lombardo, A.L. Magna, G.G.N. Angilella, R. Pucci, and R. Vilardi, Phys. Lett. A 372 (2008), p. 6168.
[601] V.M. Pereira, J.M.B. Lopes dos Santos, and A.H. Castro Neto, Phys. Rev. B 77 (2008), p. 115109.
[602] M.P. López-Sancho, F. de Juan, and M.A.H. Vozmediano, Phys. Rev. B 79 (2009), p. 075413.
[603] R. Singh and P. Kroll, J. Phys.: Condens. Matter 21 (2009), p. 196002.
[604] H. Kumazaki and D.S. Hirashima, J. Phys. Soc. Japan 76 (2007), p. 064713.
[605] J. Kang, J. Bang, B. Ryu, and K.J. Chang, Phys. Rev. B 77 (2008), p. 115453.
[606] J.J. Palacios, J. Fernández-Rossier, and L. Brey, Phys. Rev. B 77 (2008), p. 195428.
[607] B. Huang, F. Liu, J. Wu, B.-L. Gu, and W. Duan, Phys. Rev. B 77 (2008), p. 153411.
[608] Y. Zhang, S. Talapatra, S. Kar, R. Vajtai, S.K. Nayak, and P.M. Ajayan, Phys. Rev. Lett. 99 (2007), p. 107201.
[609] O.V. Yazyev, Phys. Rev. Lett. 101 (2008), p. 037203.
[610] B.-L. Huang and C.-Y. Mou, Eur. Phys. Lett. 88 (2009), p. 68005.
[611] J.R. Hahn and H. Kang, Phys. Rev. B 60 (1999), p. 6007.

[612] P. Ruffieux, O. Gröning, P. Schwaller, L. Schlapbach, and P. Gröning, Phys. Rev. Lett. 84 (2000), p. 4910.
[613] P. Ruffieux, M. Melle-Franco, O. Gröning, M. Bielmann, F. Zerbetto, and P. Gröning, Phys. Rev. B 71 (2005), p. 153403.
[614] G.M. Rutter, J.N. Crain, N.P. Guisinger, T. Li, P.N. First, and J.A. Stroscio, Science 317 (2007), p. 219.
[615] P. Mallet, F. Varchon, C. Naud, L. Magaud, C. Berger, and J.-Y. Veuillen, Phys. Rev. B 76 (2007), p. 041403(R).
[616] C. Bena, Phys. Rev. Lett. 100 (2008), p. 076601.
[617] Y. Ferro and A. Allouche, Phys. Rev. B 75 (2007), p. 155438.
[618] L. Pisani, B. Montanari, and N.M. Harrison, New J. Phys. 10 (2008), p. 033002.
[619] R.Y. Oeiras, F.M. Araújio-Moreira, and E.Z. da Silva, Phys. Rev. B 80 (2009), p. 073405.
[620] M. Topsakal, E. Aktürk, H. Sevinçli, and S. Ciraci, Phys. Rev. B 78 (2008), p. 235435.
[621] B. Sanyal, O. Eriksson, U. Jansson, and H. Grennberg, Phys. Rev. B 79 (2009), p. 113409.
[622] S. Malola, H. Häkkinen, and P. Koskinen, Appl. Phys. Lett. 94 (2009), p. 043106.
[623] M.A.H. Vozmediano, M.P. López-Sancho, T. Stauber, and F. Guinea, Phys. Rev. B 72 (2005), p. 155121.
[624] B.W. Jeong, J. Ihm, and G.-D. Lee, Phys. Rev. B 78 (2008), p. 165403.
[625] F. OuYang, B. Huang, Z. Li, J. Xiao, H. Wang, and H. Xu, J. Phys. Chem. C 112 (2008), p. 12003.
[626] A. Carpio, L.L. Bonilla, F. de Juan, and M.A.H. Vozmediano, New J. Phys. 10 (2008), p. 053021.
[627] M.T. Lusk and L.D. Carr, Phys. Rev. Lett. 100 (2008), p. 175503.
[628] J.Y. Yan, P. Zhang, B. Sun, H.-Z. Lu, Z. Wang, S. Duan, and X.-G. Zhao, Phys. Rev. B 79 (2009), p. 115403.
[629] N. Gorjizadeh, A.A. Farajian, and Y. Kawazoe, Nanotechnology 20 (2009), p. 015201.
[630] A. Cresti and S. Roche, Phys. Rev. B 79 (2009), p. 223404.
[631] D. Wei, Y. Liu, Y. Wang, H. Zhang, L. Huang, and G. Yu, Nano Lett. 9 (2009), p. 1752.
[632] B. Huang, Q. Yan, G. Zhou, J. Wu., B.-L. Gu, W. Duan, and F. Liu, Appl. Phys. Lett. 91 (2007), p. 253122.
[633] M. Deifallah, P.F. McMillan, and F. Corà, J. Phys. Chem. C 112 (2008), p. 5447.
[634] O.Ü. Aktürk and M. Tomak, Appl. Phys. Lett. 96 (2010), p. 081914.
[635] K. Sawada, F. Ishii, M. Saito, S. Okada, and T. Kawai, Nano Lett. 9 (2009), p. 269.
[636] T.O. Wehling, A.V. Balatsky, M.I. Katsnelson, A.I. Lichtenstein, K. Scharnberg, and R. Wiesendanger, Phys. Rev. B 75 (2007), p. 125425.
[637] B. Biel, X. Blase, F. Triozon, and S. Roche, Phys. Rev. Lett. 102 (2009), p. 096803.
[638] A. Quandt, C. Özdogan, J. Kunstmann, and H. Fehske, Nanotechnology 19 (2008), p. 335707.
[639] A. Quandt, C. Özdogan, J. Kunstmann, and H. Fehske, Phys. Status Solidi b 245 (2008), p. 2077.
[640] R.B. Pontes, A. Fazzio, and G.M. Dalpian, Phys. Rev. B 79 (2009), p. 033412.
[641] T. Wassmann, A.P. Seitsonen, A.M. Saitta, M. Lazzeri, and F. Mauri, Phys. Rev. Lett. 101 (2008), p. 096402.
[642] H. Xu, T. Heinzel, and I.V. Zozoulenko, Phys. Rev. B 80 (2009), p. 045308.
[643] K. Wakabayashi and M. Sigrist, Phys. Rev. Lett. 84 (2000), p. 3390.
[644] D. Konatham and A. Striolo, Nano Lett. 8 (2008), p. 4630.
[645] D. Gunlycke, J. Li, J.W. Mintmire, and C.T. White, Appl. Phys. Lett. 91 (2007), p. 112108.

[646] F. Cervantes-Sodi, G. Csányi, S. Piscanec, and A.C. Ferrari, Phys. Rev. B 77 (2008), p. 165427.
[647] F. Cervantes-Sodi, G. Csányi, S. Piscanec, and A.C. Ferrari, Phys. Status Solidi b 245 (2008), p. 2068.
[648] H. Zheng and W. Duley, Phys. Rev. B 78 (2008), p. 045421.
[649] K. Kusakabe and M. Maruyama, Phys. Rev. B 67 (2003), p. 092406.
[650] M. Maruyama and K. Kusakabe, J. Phys. Soc. Japan 73 (2004), p. 656.
[651] M. Wu, X. Wu, Y. Gao, and X.C. Zeng, Appl. Phys. Lett. 94 (2009), p. 223111.
[652] E.-J. Kan, Z. Li, J. Yang, and J.G. Hou, J. Am. Chem. Soc. 130 (2008), p. 4224.
[653] J. Berashevich and T. Chakraborty, Phys. Rev. B 80 (2009), p. 115430.
[654] T.B. Martins, R.H. Miwa, A.J.R. da Silva, and A. Fazzio, Phys. Rev. Lett. 98 (2007), p. 196803.
[655] T.B. Martins, A.J.R. da Silva, R.H. Miwa, and A. Fazzio, Nano Lett. 8 (2008), p. 2293.
[656] R.N. Costa Filho, G.A. Farias, and F.M. Peeters, Phys. Rev. B 76 (2007), p. 193409.
[657] S. Dutta, A.K. Manna, and S.K. Pati, Phys. Rev. Lett. 102 (2009), p. 096601.